

**SPINDLE CHECKPOINT SILENCING BY TRIP13**

APPROVED BY SUPERVISORY COMMITTEE

---

Xuelian “Sue” Luo, Ph.D. (Mentor)

---

Hongtao Yu, Ph.D. (Mentor)

---

Russell A. DeBose-Boyd, Ph.D. (Chair)

---

Sandeep Burma, Ph.D.

---

Michael G. Roth, Ph.D.

## **DEDICATION**

I would first like to thank my mentors, Dr. Xuelian “Sue” Luo and Dr. Hongtao Yu, for taking a chance on me when I needed to switch labs. Through their mentorship I was able to graduate “on time”. Hongtao’s enthusiasm for scientific discovery is infectious, and his combination of kindness and high expectations make him an invaluable mentor. Sue has been an excellent teacher when it comes to detailed analysis, and I greatly appreciate her patience with my mistakes and misunderstandings. I also would like to acknowledge my dissertation committee members Dr. Russell DeBose-Boyd, Dr. Sandeep Burma, and Dr. Michael Roth, and my previous mentor, Dr. Patrick Ryan Potts, for their thoughtful comments and advice through five different projects. Their help ensured my success.

I would also like to thank the past and current members of my labs for their thoughts, advice, and support over the years. For help with my project, I acknowledge Dr. Zhejian Ji, Bing Li, Dr. Faxiang Li, Dr. Byung-Cheon Jeong, Eric Yu, Dr. Chad Brautigam, and Dr. Eunhee Choi. I would be remiss not to acknowledge the invaluable friendships I have had with Dr. Saumya Ramanathan and Dr. Natalie Lundsteen, who have provided the support I needed to pursue my chosen career as an undergraduate teaching professor.

I would have accomplished none of this without the unwavering support of my husband, Perry Brulotte, and my parents, Frank and Vicky Long. My husband taught me to never give up on my dreams, my dad that, “God always knows the endpoint”, and my mom taught me how to love people in all circumstances. Above all, I thank my Lord and Savior, Jesus Christ, for telling me, “No!” when I wanted to quit, and for holding me through the difficult journey that is graduate school. He wrote this as much as I did. 1 Thess. 5:16-18.

SPINDLE CHECKPOINT SILENCING BY TRIP13

by

MELISSA LYNN BRULOTTE

DISSERTATION

Presented to the Faculty of the Graduate School of Biomedical Sciences

The University of Texas Southwestern Medical Center at Dallas

In Partial Fulfillment of the Requirements

For the Degree of

DOCTOR OF PHILOSOPHY

The University of Texas Southwestern Medical Center at Dallas

Dallas, Texas

December, 2017

Copyright

by

Melissa Lynn Brulotte, 2017

All Rights Reserved

## SPINDLE CHECKPOINT SILENCING BY TRIP13

Melissa Lynn Brulotte, Ph.D.

The University of Texas Southwestern Medical Center at Dallas, 2017

Supervising Professors: Xuelian Luo, Ph.D. and Hongtao Yu, Ph.D.

The spindle checkpoint is important for maintaining genomic stability and preventing aneuploidy, a hallmark of cancer. The checkpoint ensures that chromosome segregation does not occur until all sister chromatids are correctly attached to the mitotic spindle during metaphase. When this requirement is met, the checkpoint must be silenced for the cell to proceed to anaphase. Thyroid hormone receptor interacting protein 13 (TRIP13) is a hexameric AAA+ ATPase involved in spindle checkpoint silencing. TRIP13 functions by initiating a conformational change in mitotic arrest deficient 2 (Mad2), a key component of the mitotic checkpoint complex (MCC). This TRIP13-mediated conformational change of Mad2 causes MCC disassembly and relieves inhibition of the anaphase promoting complex/cyclosome

(APC/C). The interaction between TRIP13 and Mad2 is dependent on the p31<sup>comet</sup> adaptor protein.

In my first project, I show that TRIP13-p31<sup>comet</sup> disrupts the MCC by local unfolding of Mad2. I identify a binding surface on human TRIP13 for p31<sup>comet</sup>-Mad2 and key TRIP13 residues involved in its conformational dynamics. I propose that the flexibility of the hinge region of TRIP13 is important for coupling its ATPase activity to substrate unfolding. The hinge region is conserved in other eukaryotic AAA+ ATPases, and may also be important for energetic coupling in those systems. I have also reconstituted the process of spindle checkpoint silencing in vitro. Importantly, I show that TRIP13 can disrupt the free MCC complex, but not MCC bound to APC/C, providing an explanation for the coordination of the multiple mechanisms that work together to achieve spindle checkpoint silencing.

In my second project, to provide a tool for future mechanistic studies and to examine the oncogenic activity of TRIP13, I attempted to identify chemical inhibitors for TRIP13 through high-throughput screening. I identified a series of lead compounds that indirectly inhibited TRIP13 as pan-assay interference compounds. These compounds are redox cyclers that generate hydrogen peroxide, which covalently modifies protein residues such as cysteines and tryptophans. No other potent lead compounds were discovered. This study revealed that TRIP13 may be a difficult protein to target, and that large compound libraries should be prescreened for redox cyclers before they are used in high-throughput inhibitor screening.

## TABLE OF CONTENTS

<b>DEDICATION.....</b>	<b>II</b>
<b>TABLE OF CONTENTS .....</b>	<b>VII</b>
<b>PRIOR PUBLICATIONS .....</b>	<b>XI</b>
<b>LIST OF FIGURES .....</b>	<b>XII</b>
<b>LIST OF TABLES .....</b>	<b>XIV</b>
<b>LIST OF DEFINITIONS .....</b>	<b>XV</b>
<b>CHAPTER I: INTRODUCTION .....</b>	<b>1</b>
<b>SPINDLE CHECKPOINT ACTIVATION .....</b>	<b>2</b>
<i>The metaphase-to-anaphase transition is activated by APC/C<sup>Cdc20</sup> .....</i>	<i>2</i>
<i>APC/C<sup>Cdc20</sup> is inhibited by the mitotic checkpoint complex.....</i>	<i>3</i>
<i>Kinetochore recruitment and activation of spindle checkpoint proteins</i> .....	<i>3</i>
<i>Mad2 Conformational Change and MCC Formation .....</i>	<i>5</i>
<b>SPINDLE CHECKPOINT SILENCING.....</b>	<b>6</b>
<i>Microtubule attachment competes with Mps1 .....</i>	<i>7</i>
<i>Removal of Mad1-Mad2 from the kinetochore .....</i>	<i>8</i>
<i>APC/C<sup>Cdc20</sup> ubiquitination of MCC-bound Cdc20.....</i>	<i>9</i>
<i>p31<sup>comet</sup> as a spindle checkpoint protein .....</i>	<i>10</i>
<i>TRIP13 as a spindle checkpoint protein .....</i>	<i>11</i>
<b>CHAPTER II: MATERIALS AND METHODS .....</b>	<b>18</b>
<b>PROTEIN EXPRESSION AND PURIFICATION .....</b>	<b>18</b>

<i>TRIP13</i> .....	18
<i>p31<sup>comet</sup> and Mad2</i> .....	19
<i>ΔN35-p31<sup>comet</sup>-Mad2<sup>L13A</sup> and Mad2</i> .....	19
<i>ΔN35-p31<sup>comet</sup></i> .....	19
<i>Mad2<sup>R133A</sup></i> .....	20
<i>ΔN10-Mad2</i> .....	21
<i>Cdc20</i> .....	21
<i>p97/VCP</i> .....	22
NMR SPECTROSCOPY .....	23
X-RAY CRYSTALLOGRAPHY .....	24
<i>Crystallization, data collection and structure determination</i> .....	24
<i>Accession codes</i> .....	25
ATPASE ASSAYS .....	25
<i>ADP-Glo™ Kinase Assay</i> .....	25
<i>Kinase Glo® ATPase Assay</i> .....	26
MAD2 DISSOCIATION AND BINDING ASSAYS .....	26
ANALYTICAL ULTRACENTRIFUGATION.....	27
APC/C UBIQUITINATION ASSAY.....	28
HIGH-THROUGHPUT SCREENING.....	29
ASSAY FOR THE GENERATION OF HYDROGEN PEROXIDE.....	30

**CHAPTER III: MECHANISTIC INSIGHT INTO TRIP13-CATALYZED MAD2  
STRUCTURAL TRANSITION AND SPINDLE CHECKPOINT SILENCING..... 32**

INTRODUCTION ..... 32

RESULTS ..... 36

*TRIP13 and p31<sup>comet</sup> convert C-Mad2 to O-Mad2 without global unfolding of C-Mad2*  
..... 36

*Crystal structure of human TRIP13 in its monomeric ADP-bound state* ..... 38

*Identification of TRIP13 residues critical for its p31<sup>comet</sup>-Mad2-stimulated ATPase  
activity*..... 40

*TRIP13 mutants not stimulated by p31<sup>comet</sup>-Mad2 fail to release C-Mad2 from ligands*  
..... 42

*The hinge impacts TRIP13 conformational dynamics and oligomerization*..... 43

*Identification of p31<sup>comet</sup>-Mad2-binding residues on TRIP13*..... 45

*Reconstitution of TRIP13-dependent MCC inactivation in vitro*..... 47

*The N-terminus of Mad2 is necessary for TRIP13 inactivation of MCC*..... 48

DISCUSSION ..... 50

*Mechanism of TRIP13-catalyzed Mad2 structural transition* ..... 51

*Mechanistic insight into MCC inactivation by TRIP13*..... 52

**CHAPTER IV: EXPLORING CHEMICAL INHIBITION OF THE TRIP13  
ONCOPROTEIN ..... 74**

INTRODUCTION ..... 74

RESULTS ..... 76

<i>Development of an HTS assay for inhibitors of TRIP13.....</i>	<i>76</i>
<i>Development of a counter-screen to identify non-specific inhibitors of AAA+ ATPases .....</i>	<i>78</i>
<i>Secondary screening of lead compounds from the 8,000 compound screen .....</i>	<i>78</i>
<i>Secondary screening of lead compounds from the 200,000 compound screen .....</i>	<i>80</i>
<i>Toxoflavins and other lead compounds interfere with the ATPase assay by redox cycling.....</i>	<i>81</i>
<b>DISCUSSION.....</b>	<b>82</b>
<b>CHAPTER V: PERSPECTIVES.....</b>	<b>97</b>
<b>BIBLIOGRAPHY .....</b>	<b>99</b>

## **PRIOR PUBLICATIONS**

Brulotte, M.L., Jeong, B.C., Li, F., Li, B., Yu, E. B., Wu, Q., Brautigam, C.A., Yu, H., Luo, X. (2017) Mechanistic Insight into TRIP13-catalyzed Mad2 Structural Transition and Spindle Checkpoint Silencing. *Nature Communications*. *Accepted*.

## LIST OF FIGURES

Figure 1: Metaphase to anaphase transition is activated by APC/C Cdc20.....	14
Figure 2: APC/C Cdc20 is inhibited by the mitotic checkpoint complex (MCC).....	15
Figure 3: Kinetochore recruitment of spindle checkpoint proteins, mitotic checkpoint complex (MCC) assembly, and spindle checkpoint silencing.....	16
Figure 4: Comparison of the structures of APC/CMCC-closed and APC/CMCC-open. ....	17
Figure 5: TRIP13 catalyzes C-Mad2 to O-Mad2 conversion in the presence of p31 <sup>comet</sup> ....	55
Figure 6: TRIP13 catalyzes the conversion of C-Mad2 to O-Mad2 with the help of p31 <sup>comet</sup> .....	56
Figure 7: TRIP13-catalyzed structural transition of Mad2 does not involve Mad2 global unfolding.....	57
Figure 8: Crystal structure of human TRIP13 in its monomeric ADP-bound state.....	58
Figure 9: Development of a high-throughput assay to assess the ATPase activity of TRIP13 mutants.....	59
Figure 10: Identification of TRIP13 mutants with defective p31 <sup>comet</sup> -Mad2 stimulation.	61
Figure 11: The TRIP13 hinge is required for conformational dynamics and oligomerization .....	62
Figure 12: TRIP13 promotes dissociation of Mad2 from peptide ligands.....	64
Figure 13: TRIP13 G320A forms oligomers in the presence of ATP .....	65
Figure 14: The p31 <sup>comet</sup> -Mad2 complex prefers to bind to TRIP13 in the ATP-bound state .....	66
Figure 15: Identification of a p31 <sup>comet</sup> -Mad2-binding site on TRIP13.....	67

Figure 16: TRIP13 prevents APC/C <sup>Cdc20</sup> inhibition by MCC components .....	68
Figure 17: The N-terminus of Mad2 is required for binding TRIP13 and for inactivation of MCC by TRIP13 .....	70
Figure 18: TRIP13 W221C phenocopies TRIP13 W221A, and it cannot bind to p31 <sup>comet</sup> -Mad2 .....	71
Figure 19: Mechanisms of TRIP13-dependent Mad2 conformational change and checkpoint silencing .....	72
Figure 20: Development of a HTS assay for inhibitors of TRIP13 .....	85
Figure 21: No lead compounds for inhibition or activation of TRIP13 were identified in the 8000 compound screen .....	87
Figure 22: The 200,000 compound screen identified 54 compounds that inhibit the ATPase activity of TRIP13.....	90
Figure 23: Secondary screening identified 12 compounds that inhibit Mad2 conformational change by TRIP13.....	91
Figure 24: Structures of lead compounds that may inhibit TRIP13 .....	94
Figure 25: Toxoflavins and other lead compounds interfere with the ATPase assay by redox cycling .....	95
Figure 26: Compound SW056958 may be a candidate for TRIP13 inhibition. ....	96

## LIST OF TABLES

Table 1: Data Collection and Refinement Statistics for human TRIP13 .....	31
Table 2: Activity scores of the 18 lead compounds from the 8000 compound screen .....	89
Table 3: Activity scores of the 12 lead compounds from the 200,000 compound screen ....	93

## LIST OF DEFINITIONS

AAA – ATPases Associated with diverse cellular Activities  
ADP – adenosine diphosphate  
APC/C – anaphase-promoting complex/cyclosome  
Apc15 – anaphase promoting complex 15  
ATP – adenosine triphosphate  
ATPase – adenosine triphosphate hydrolase  
ATP $\gamma$ S – adenosine triphosphate gamma-sulfur  
AUC – analytical ultracentrifugation  
BME –  $\beta$ -mercaptoethanol  
BSA – bovine serum albumin  
Bub1 – budding uninhibited by benomyl 1  
Bub3 – budding uninhibited by benomyl 3  
BubR1 – Bub1-related 1  
CBB – Coomassie brilliant blue  
CCAN – constitutive centromere-associated network  
Cdc20 – cell division cycle 20  
Cdc20N – Cdc20 N-terminal 170-residue fragment  
Cdk1 – cyclin-dependent kinase 1  
CENP – centromere protein  
ClpP – caseinolytic mitochondrial matrix peptidase proteolytic subunit  
ClpX – caseinolytic mitochondrial matrix peptidase chaperone subunit  
C-Mad2 – closed Mad2  
CRC – colorectal cancer  
DMSO – dimethyl sulfoxide  
Dsn1 – dosage suppressor of Nnf1  
DTT – dithiothreitol  
H/D – Proton/deuterium  
H<sub>2</sub>O<sub>2</sub> – hydrogen peroxide  
HBSS – Hank's Buffered Salt Solution  
Hec1 – highly expressed in cancer 1  
HRP-PR – horseradish peroxidase-phenol red  
HSQC – Heteronuclear single quantum correlation  
HTS – high-throughput screening  
I-Mad2 – intermediate Mad2  
IP – immunoprecipitation  
IPTG – isopropyl  $\beta$ -D-1-thiogalactopyranoside  
K<sub>d</sub> – dissociation constant  
kD – kilodaltons  
KDM4A – lysine-specific demethylase 4A  
K<sub>M</sub> – Michaelis binding constant  
KMN – Knl1/Mis12C/Ndc80C  
Knl1 – kinetochore null 1

Mad1 – mitotic arrest deficiency 1  
Mad2 – mitotic arrest deficiency 2  
MBP1 – Mad2-binding peptide 1  
MCC – mitotic checkpoint complex  
MELT – methionine-glutamate-leucine-threonine  
MIM – Mad2-interacting motif  
Mis12 – minichromosome instability 12  
Mis12C – Mis12 complex  
MOPS – 3-(N-morpholino)propanesulfonic acid  
Mps1 – monopolar spindle 1  
Ndc80 – nuclear division cycle 80  
Ndc80C – Ndc80 complex  
NMR – nuclear magnetic resonance  
Nnf1 – necessary for nuclear function 1  
NSF – N-ethylmaleimide sensitive fusion protein  
Nsl1 – Nnf1 synthetic lethal 1  
Nuf2 – Nuclear filament-containing protein 2  
O-Mad2 – open Mad2  
PAINS – pan-assay interference compounds  
PCH2 – pachytene checkpoint 2  
PCR – polymerase chain reaction  
Plk1 – polo-like kinase 1  
PMSF – phenylmethylsulfonyl fluoride  
PP1 – protein phosphatase 1  
redox – reduction/oxidation  
Rod – rough deal homolog  
RZZ – Rod-Zwilch-ZW10 complex  
SCCHN – squamous cell carcinoma of the head and neck  
SD – standard deviation  
SDS – sodium dodecylsulfate  
SDS-PAGE – SDS polyacrylamide electrophoresis  
Spc24 – spindle component 24  
Spc25 – spindle component 25  
SV – sedimentation velocity  
TCEP – tris(2-carboxyethyl)phosphine  
TCF – T-cell factor  
TEV – tobacco etch virus protein  
TPR – tetratricopeptide repeat  
TRIP13 – Thyroid receptor-interacting protein 13  
Ub – ubiquitin  
Uba1 – Ubiquitin-activating enzyme E1  
UbcH10 – Ube2C, Ubiquitin-conjugating enzyme E2 C  
Ube2S – Ubiquitin-conjugating enzyme E2 S  
USP44 – ubiquitin-specific protease 44

VCP – vasolin-containing protein

WT – wild-type

ZW10 – zeste white 10

Zwint – ZW10 interacting kinetochore protein

## **CHAPTER ONE**

### **Introduction**

The physical and molecular properties of cell division have been studied for about 150 years. In 1882, Walther Flemming first described the stages of mitosis (Flemming, 1882; Paweletz, 2001), the process by which the eukaryotic cell segregates its chromosomes into two daughter cells. Mitosis is now taught at all levels of education, starting as early as elementary school. Shortly afterward, Theodor Boveri began his own studies of cell division, first focused on the role of centrosomes and their attachment to chromosomes. Using *Ascaris* and sea urchin eggs as model systems, he was one of the first to describe that chromosomes form bipolar attachments to two different centrosomes, and suggested that chromosomes had individual identities (Boveri, 1887; Maderspacher, 2008; Manchester, 1995; Scheer, 2014). Boveri is most well-known for his part in the chromosome theory of inheritance, which described chromosomes as the carriers of genetic material (Boveri, 1904; Maderspacher, 2008). This was independently described by Walter Sutton around the same time (1902-1904), and thus is sometimes known as the Boveri-Sutton Chromosome Theory.

Less well-known is that Boveri was the first to suggest that abnormal chromosome number, or aneuploidy, could be a cause of cancer (Boveri, 1902; Holland and Cleveland, 2009). In his 1902 paper, Boveri commented that sea urchin embryos developed abnormal growths or “tumors” from cells that had multipolar spindles (Manchester, 1995). He reiterated this and other theories in a 1914 paper, where he described cancer as developing from normal cells that undergo some change that leads to abnormal cell division and growth (Boveri, 1914; Holland and Cleveland, 2009; Manchester, 1995). One of the changes he observed was aneuploidy. He also described the presence of some kind of “arrangement for inhibition” that

prevents cell division from happening until a certain stimulus is produced (Boveri, 1914; Manchester, 1995), eluding to the spindle checkpoint 75 years before Leland Hartwell introduced the concept of cell cycle checkpoints (Weinert and Hartwell, 1989).

The work of Boveri and other pioneers set the stage for over 100 years of studies on the importance of mitosis, and more recently the spindle checkpoint, in maintaining genomic stability to prevent aneuploidy and cancer. The molecular processes of the spindle checkpoint have been studied since 1991 (Fisk, 2015; Hoyt et al., 1991; Li and Murray, 1991), and new discoveries are still being published today. A summary of what is currently known about the spindle checkpoint is described here, followed by new work on the role of TRIP13 in spindle checkpoint silencing.

## SPINDLE CHECKPOINT ACTIVATION

### **The metaphase-to-anaphase transition is activated by APC/C<sup>Cdc20</sup>**

The spindle checkpoint controls the transition between the metaphase and anaphase stages of mitosis (Jia et al., 2013; London and Biggins, 2014b; Musacchio, 2015). This transition is ultimately activated by the anaphase promoting complex or cyclosome (APC/C), a large ubiquitin ligase complex, bound to its mitotic activator, Cdc20 (Chang and Barford, 2014; Kim and Yu, 2011; Sivakumar and Gorbsky, 2015; Yu, 2007). When all the chromosomes in a cell achieve bipolar attachment to the mitotic spindle in metaphase, APC/C<sup>Cdc20</sup> is activated to ubiquitinate its substrates – cyclin B and securin – which are then degraded by the proteasome (Fig. 1a) (Chang and Barford, 2014). Degradation of cyclin B inactivates Cdk1, allowing mitosis to progress (Chang and Barford, 2014). Degradation of securin releases separase,

which cleaves cohesin at the centromeres of the chromosomes, allowing the sister chromatids to separate (Chang and Barford, 2014). This separation marks the start of anaphase.

### **APC/C<sup>Cdc20</sup> is inhibited by the mitotic checkpoint complex**

APC/C<sup>Cdc20</sup> must be inhibited during prophase and prometaphase to ensure that the chromosomes attach properly to the mitotic spindle before sister chromatid separation. If APC/C<sup>Cdc20</sup> is prematurely activated, chromosomes may missegregate, leading to aneuploidy (Fig. 1b). The mitotic checkpoint complex (MCC) is the spindle checkpoint effector that consists of four proteins: Mad2, Cdc20, BubR1, and Bub3 (Bharadwaj and Yu, 2004; Musacchio and Salmon, 2007; Yu, 2007). The MCC is assembled at kinetochores in a tightly controlled mechanism involving several phosphorylation and binding events. The MCC inhibits APC/C<sup>Cdc20</sup> by binding to the substrate recognition site of the ubiquitin ligase (Fig. 2a) (Alfieri et al., 2016; Izawa and Pines, 2015; Yamaguchi et al., 2016). Thus, the physiological form of APC/C<sup>MCC</sup> includes two Cdc20 subunits: the APC/C-associated Cdc20 (Cdc20<sup>APC/C</sup>) and MCC-associated Cdc20 (Cdc20<sup>MCC</sup>).

### **Kinetochores recruitment and activation of spindle checkpoint proteins**

The kinetochore of chromosomes is classically known as the attachment site for the microtubules of the mitotic spindle. When it is unattached to microtubules, the kinetochore also serves as a platform for the recruitment and activation of the spindle checkpoint proteins (Fig. 3). The kinetochore consists of both an “inner” and an “outer” layer. The inner kinetochore is formed on the centromere of chromosomes, specifically at nucleosomes

containing CENP-A, a histone H3 variant (Black and Cleveland, 2011; Black et al., 2007). The inner kinetochore is made from the constitutive centromere-associated network (CCAN), consisting of 16 CENP proteins that associate together in several subcomplexes to support the recruitment of outer kinetochore proteins (Pesenti et al., 2016; Weir et al., 2016).

The outer kinetochore is the site of microtubule attachment, and recruitment and activation of spindle checkpoint proteins. A major component of the outer kinetochore is the KMN network of proteins, consisting of three subcomplexes termed Knl1, Mis12C, and Ndc80C. Knl1 contains Knl1 and Zwint (in humans); Mis12C has Dsn1, Nsl1, Mis12, and Nnf1; and Ndc80C consists of Hec1, Nuf2, Spc25, and Spc24 (Cheeseman et al., 2006; Cheeseman and Desai, 2008; Kim and Yu, 2011). All three complexes help to anchor the KMN to the CCAN, and Ndc80C and Knl1 bind microtubules directly (Ji et al., 2017; Kim and Yu, 2011). When kinetochores are not attached to microtubules, the KMN network undergoes several phosphorylation events that ultimately lead to the recruitment of the spindle checkpoint components.

Mps1 is the master kinase that initiates the spindle checkpoint. Mps1 binds to the Nuf2 and Hec1 subunits of Ndc80C by two distinct mechanisms (Hiruma et al., 2015; Ji et al., 2015). The binding of Mps1 to Hec1 is dependent on phosphorylation by another kinase, Aurora B (Ji et al., 2015; Zaytsev et al., 2014). After binding to Ndc80C, Mps1 phosphorylates Knl1 at multiple methionine-glutamate-leucine-threonine (MELT) motifs to recruit Bub1-Bub3 and BubR1-Bub3 to the kinetochore, with Bub3 binding to the phosphosites directly (Krenn et al., 2014; London and Biggins, 2014a; Shepperd et al., 2012; Yamagishi et al., 2012). BubR1-Bub3 is a component of the MCC, while Bub1-Bub3 serves as the recruitment platform for the

other MCC proteins, Cdc20 and Mad2. Cdc20 binds to Bub1 and BubR1 directly to be primed for incorporation into the MCC (Diaz-Martinez et al., 2015; Han et al., 2014; Jia et al., 2016; Lischetti et al., 2014). Mad2, however, is a two-state protein that requires a conformational change from its inactive, open form (O-Mad2) to the active, closed form (C-Mad2) to allow formation of the MCC (Luo et al., 2000; Luo et al., 2002; Luo et al., 2004; Luo and Yu, 2005, 2008; Yang et al., 2008). This is dependent on the catalytic engine of MCC formation, the Mad1-Mad2 core complex.

#### *Mad2 Conformational Change and MCC Formation*

Mad1 forms a constitutive core complex with Mad2 throughout the cell cycle. The Mad1-Mad2 core complex is a heterotetramer consisting of the Mad1 homodimer with each Mad1 molecule binds to one copy of C-Mad2. The Mad1-bound C-Mad2 serves as a template for the conversion of Mad2 from the open form to the closed form. Mad1-Mad2 recruitment to kinetochores requires phosphorylation by Mps1. After Bub1-Bub3 is recruited by Mps1 phosphosites, Bub1 is phosphorylated by the checkpoint kinase Cdk1 at serine-459 (Ji et al., 2017). This primes Bub1 for phosphorylation by Mps1 at threonine-461, creating docking sites for Mad1-Mad2 (Ji et al., 2017). Mad1 binds directly to phosphothreonine-461, localizing the heterodimer to the kinetochore (Ji et al., 2017). Once Mad1-Mad2 is recruited, it is also phosphorylated by Mps1 (Ji et al., 2017). This creates an interaction site for the N-terminal region of Cdc20, which is already bound to Bub1, and thus brings Cdc20 in close proximity to the Mad1-Mad2 catalytic engine (Ji et al., 2017).

Once Mad1-Mad2 is recruited to the kinetochore, it serves as a template for conversion of O-Mad2 to C-Mad2. O-Mad2 in the cytosol binds to C-Mad2 in the Mad1-Mad2 core complex, and the O-Mad2 undergoes a conformational change to an intermediate form, I-Mad2 (Fig. 3) (Hara et al., 2015; Skinner et al., 2008). At this point, all four MCC components are bound to the kinetochore: the BubR1-Bub3 subcomplex is bound to Bub1-Bub3 and Mps1-phosphorylated Knl1, Cdc20 is bound to Bub1 and Mps1-phosphorylated Mad1, and I-Mad2 is bound to Mad1-Mad2 (Fig. 3). In the intermediate form, I-Mad2 is primed for MCC incorporation, and binds to BubR1-Bub3 and Cdc20 as C-Mad2 (Kulukian et al., 2009; Musacchio, 2015). Once the MCC forms, it can diffuse away from kinetochores and readily inhibit APC/C<sup>Cdc20</sup>, thus initiating the spindle checkpoint (Fig. 3). C-Mad2 is more energetically stable than O-Mad2 (Luo et al., 2004), and thus once Mad2 is incorporated into the MCC, energy input is required to convert Mad2 back to the open form.

### **SPINDLE CHECKPOINT SILENCING**

Inhibition of APC/C<sup>Cdc20</sup> by the spindle checkpoint effectively prevents anaphase from occurring until all the sister chromatids are bidirectionally attached to the mitotic spindle. However, once sister chromatids are bound by microtubules, the checkpoint must be turned off to allow anaphase to proceed. If this does not occur, the cell will undergo prolonged mitotic arrest, leading to either cell death in mitosis, or exit from mitosis without chromosome segregation which can lead to polyploidy or cell death in interphase (Fig. 2b). There are various mechanisms by which the spindle checkpoint is silenced such that APC/C<sup>Cdc20</sup> is no longer

inhibited, checkpoint signaling is ceased, the formation of the MCC is disrupted, and preformed MCC is disassembled.

### **Microtubule attachment competes with Mps1**

The binding of microtubules to the KMN network affects spindle checkpoint silencing directly. As previously discussed, Mps1 binds to the Nuf2 and Hec1 subunits of Ndc80C in a phosphorylation-dependent manner to further phosphorylate the KMN network for recruitment of checkpoint and MCC components (Hiruma et al., 2015; Ji et al., 2017; Ji et al., 2015). Microtubules also bind to Ndc80C at Nuf2 and Hec1, and binding is dependent on the phosphorylation state of the Hec1 tail: hyperphosphorylation of the tail by Aurora B lowers the affinity of Ndc80C for microtubules, while hypophosphorylation permits binding of microtubules (Alushin et al., 2012; Ciferri et al., 2008; DeLuca et al., 2006; Guimaraes et al., 2008; Miller et al., 2008). The opposite is true for the recruitment of Mps1: phosphorylation of the Hec1 tail by Aurora B is required for localization to Ndc80C (Ji et al., 2015). In 2015, our group and the Kops group independently reported that Mps1 competes directly with microtubules for binding to the KMN network (Hiruma et al., 2015; Ji et al., 2015). Thus, when microtubules bind to kinetochores, Mps1 is removed, reducing the phosphorylation of the KMN and the recruitment of spindle checkpoint proteins. Phosphorylation that has already occurred on the KMN is removed by protein phosphatase 1 (PP1), which is recruited to kinetochores by Knl1 and other kinetochore proteins, such as the Ska complex (Liu et al., 2010; London and Biggins, 2014a; Meadows et al., 2011; Rosenberg et al., 2011; Sivakumar et al.,

2016). Thus, removal of Mps1 from the KMN is one mechanism by which spindle checkpoint signaling and the formation of the MCC are reduced.

### **Removal of Mad1-Mad2 from the kinetochore**

Another way to silence the spindle checkpoint involves the removal of Mad1-Mad2 from kinetochores to prevent MCC formation, since O-Mad2 would no longer be converted to C-Mad2 for incorporation into the MCC. The physical removal of the Mad1-Mad2 core complex is directed by the dynein motor protein. Dynein is recruited to the kinetochore by binding to the Rod-Zwilch-Zw10 complex (RZZ) and Spindly (Barisic and Geley, 2011; Gassmann et al., 2008; Griffis et al., 2007; London and Biggins, 2014b). In addition to binding to Bub1, Mad1-Mad2 can also bind to Spindly (Kops et al., 2005; London and Biggins, 2014b; Matson and Stukenberg, 2014; Varma et al., 2013). This may be a second way to recruit Mad1-Mad2 to the kinetochore (Kops et al., 2005; Varma et al., 2013). It is thought that a kinetochore complex containing RZZ, Spindly, Mad1-Mad2, and dynein may exist both when the spindle checkpoint is activated, and when it is silenced (London and Biggins, 2014b). The difference is that when microtubules bind to the kinetochore during silencing, dynein can bind to the microtubule and walk toward the minus end at the spindle poles (Howell et al., 2001; Zhang et al., 2007). This physically disrupts the interaction between RZZ-Spindly and the kinetochore, allowing dynein to pull RZZ-Spindly and Mad1-Mad2 away from the kinetochore (London and Biggins, 2014b). This physical removal of spindle checkpoint components disrupts the formation of the MCC.

### **APC/C<sup>Cdc20</sup> ubiquitination of MCC-bound Cdc20**

Disruption of the formation of the MCC by reducing the recruitment of spindle checkpoint components at the kinetochore, and by removal of checkpoint proteins that have already been recruited, is insufficient to silence the checkpoint: the MCC that has already been formed needs to be disassembled. This can be accomplished by APC/C<sup>Cdc20</sup> ubiquitination of the Cdc20 subunit of the MCC (Cdc20<sup>MCC</sup>), allowing APC/C<sup>Cdc20</sup> to relieve inhibition of itself (Foster and Morgan, 2012; Jia et al., 2011; Reddy et al., 2007; Stegmeier et al., 2007; Uzunova et al., 2012). The ubiquitination of MCC-bound Cdc20 (Cdc20<sup>MCC</sup>) leads to recognition of Cdc20 by the proteasome and degradation, therefore removing Cdc20 from the MCC and causing MCC disassembly (Jia et al., 2011; Reddy et al., 2007; Stegmeier et al., 2007).

The process of Cdc20<sup>MCC</sup> ubiquitination is theorized to be constitutive: APC/C<sup>Cdc20</sup> continuously ubiquitinates Cdc20 to disassemble the MCC (Stegmeier et al., 2007; Uzunova et al., 2012). This means that to maintain the spindle checkpoint, a new MCC complex would need to bind to APC/C<sup>Cdc20</sup> every time one is removed. Thus, the steady-state levels of MCC in the cell depend on both the rate of MCC production and the rate of MCC disassembly. Cdc20<sup>MCC</sup> ubiquitination is controlled by the Apc15 subunit of APC/C<sup>Cdc20</sup>, which is dispensable for ubiquitination of cyclin B1 and securin (Foster and Morgan, 2012; Uzunova et al., 2012). The binding or release of Apc15 from the APC/C<sup>Cdc20</sup> ubiquitin ligase may aid in controlling spindle checkpoint activation or silencing.

In 2016, the cryo-electron microscopy (cryo-EM) structure of APC/C<sup>Cdc20</sup> bound to MCC (APC/C<sup>MCC</sup>) was solved, providing more mechanistic insight into the ubiquitination of Cdc20<sup>MCC</sup> (Alfieri et al., 2016). This study, along with another study by Schulman and

coworkers (Yamaguchi et al., 2016), revealed that APC/C<sup>MCC</sup> adopts two distinct conformations: a closed form that occludes access of the ubiquitination machinery to Cdc20<sup>MCC</sup>, and an open form that allows ubiquitination to occur. This is driven by the conformational change of Apc15. In the structure of APC/C<sup>MCC-closed</sup>, Apc15 is disordered and the TPR domain of the BubR1 subunit of MCC blocks the E2 ubiquitin ligase, UbcH10, from accessing Cdc20<sup>MCC</sup>. In contrast, in APC/C<sup>MCC-open</sup>, Apc15 is well-defined and MCC-Cdc20<sup>APC/C</sup> is rotated to allow Cdc20<sup>MCC</sup> to bind UbcH10 (Fig. 4). The cryo-EM structure of APC/C<sup>MCC-UbcH10</sup> was also determined in the same study, and it revealed that APC/C<sup>MCC-UbcH10</sup> resembles APC/C<sup>MCC-open</sup>, and that the C-terminus of Cdc20<sup>MCC</sup> was accessible by UbcH10. The authors concluded that modulation of the conformation of APC/C and MCC components allow for ubiquitination of Cdc20<sup>MCC</sup>, and that the conformational switch may be mediated by another checkpoint silencing protein, p31<sup>comet</sup>, which shall be discussed next.

### **p31<sup>comet</sup> as a spindle checkpoint silencing protein**

p31<sup>comet</sup> was identified as a Mad2-binding protein in 2002 (Habu et al., 2002). This protein binds specifically to C-Mad2 in the MCC and in the Mad1-Mad2 complex (Mapelli et al., 2006; Xia et al., 2004; Yang et al., 2007). In the Mad1-Mad2 complex, p31<sup>comet</sup> binding blocks the binding site of O-Mad2 on the C-Mad2 template, effectively blocking the conversion of O-Mad2 to C-Mad2 such that the MCC can no longer form (Mapelli et al., 2006; Yang et al., 2007).

p31<sup>comet</sup> also disrupts the MCC complex by directly competing with the BubR1 binding site on C-Mad2 (Chao et al., 2012; Yang et al., 2007). It can therefore block MCC formation

by binding to C-Mad2 bound to Cdc20 (Jia et al., 2011; Xia et al., 2004) or cause MCC disassembly by competing BubR1 off of MCC (Miniowitz-Shemtov et al., 2012; Teichner et al., 2011; Westhorpe et al., 2011). The latter activity garners the most interest because it suggests a way to promote MCC disassembly independently of Cdc20<sup>MCC</sup> ubiquitination by APC/C<sup>Cdc20</sup>. Indeed, ubiquitination of Cdc20<sup>MCC</sup> by APC/C<sup>Cdc20</sup> is not required for spindle checkpoint silencing (Jia et al., 2011). p31<sup>comet</sup> was found to act redundantly with Cdc20<sup>MCC</sup> ubiquitination, and it is capable of accessing both free MCC and MCC bound to APC/C (Jia et al., 2011; Westhorpe et al., 2011; Xia et al., 2004). Interestingly, binding of p31<sup>comet</sup> to C-Mad2 can also indirectly cause the release of Cdc20 from both Mad2 and BubR1 (Jia et al., 2011; Teichner et al., 2011). This activity is dependent on ATP hydrolysis, though p31<sup>comet</sup> has no enzymatic activity (Miniowitz-Shemtov et al., 2010; Teichner et al., 2011). This discrepancy remained a mystery until 2014, when thyroid interacting protein 13 (TRIP13) was discovered to have a role in mitosis (Eytan et al., 2014; Wang et al., 2014a).

### **TRIP13 as a checkpoint silencing protein**

TRIP13, also known as pachytene checkpoint 2 (PCH2), is an ATPases Associated with diverse cellular Activities (AAA+) protein that was originally discovered to have a role in homologous recombination during meiosis (San-Segundo and Roeder, 1999). The activity in meiosis is independent of its role in mitosis as it involves different substrates, and thus it will not be discussed further here. In 2014, two groups independently identified that TRIP13 has a direct role in spindle checkpoint silencing in mitosis and that this activity is in concert with p31<sup>comet</sup> (Eytan et al., 2014; Wang et al., 2014a).

Further work in the last several years has identified that p31<sup>comet</sup> binds to TRIP13 and acts as an adaptor protein between TRIP13 and Mad2 (Miniowitz-Shemtov et al., 2015; Ye et al., 2015). TRIP13 hydrolyzes ATP to direct the conformational change of C-Mad2 to O-Mad2, thus providing the energy needed to convert the more stable C-Mad2 to the less stable open form (Ye et al., 2015). Therefore, TRIP13 and p31<sup>comet</sup> are spindle checkpoint silencing proteins that promote MCC disassembly by changing the conformation of Mad2 such that it can no longer bind BubR1 or Cdc20 (Fig. 3). This completes checkpoint silencing: displacement of Mps1 from the KMN by microtubules reduces checkpoint signaling; removal of Mad1-Mad2 from kinetochores halts the conversion of O-Mad2 to C-Mad2, and therefore stops MCC formation; APC/C<sup>Cdc20</sup> ubiquitinates Cdc20<sup>MCC</sup> to promote MCC disassembly; and TRIP13 and p31<sup>comet</sup> also work to completely disassemble MCC by resetting C-Mad2 to O-Mad2.

Despite this large body of work, it is not clear how these mechanisms for spindle checkpoint silencing work together in time and space. Additional mechanisms of checkpoint silencing may exist. In 2016, Ma and Poon reported that neither TRIP13 nor p31<sup>comet</sup> is strictly required for cells to exit mitosis. Furthermore, they reported that C-Mad2 could be converted to O-Mad2 in the absence of p31<sup>comet</sup> (Ma and Poon, 2016). Recent *in vitro* studies suggest this may be due to the action of another ATPase (Kaisari et al., 2017), though further work in cells must be done to confirm this finding. Interestingly, TRIP13 may be required for spindle checkpoint initiation as well as silencing because knockout of TRIP13 prevented cells from initiating a checkpoint response (Ma and Poon, 2016). This may be because TRIP13 maintains the pool of O-Mad2 in the cell: in the absence of TRIP13, all of Mad2 was found to be in the

closed form, which cannot interact with Mad1-Mad2 core efficiently and cannot be incorporated into the MCC (Ma and Poon, 2016). These recent findings reveal a need for further mechanistic studies of TRIP13 to answer some of the outstanding questions in the field.

I endeavored to answer some of these questions by examining the mechanism by which TRIP13-p31<sup>comet</sup> binds and unfolds Mad2, and by reconstituting spindle checkpoint silencing by TRIP13-p31<sup>comet</sup> *in vitro* (Chapter III). Furthermore, I attempted to identify chemical inhibitors of TRIP13 to both provide a tool for future mechanistic studies, and to begin to explore the therapeutic potentials of such inhibitors in cancer therapy, as TRIP13 is an oncogene (Chapter IV). The previous work on TRIP13 in cancer is discussed at length in the introduction of Chapter IV. My studies provided important insights into the function of TRIP13. Most notably, we found that TRIP13 cannot access C-Mad2 that is bound to APC/C<sup>MCC</sup>, thus providing a potential connection between ubiquitination of Cdc20<sup>MCC</sup> by APC<sup>Cdc20</sup>, p31<sup>comet</sup> binding to APC/C<sup>MCC</sup>, and TRIP13-mediated disassembly of the MCC (Figure 18).

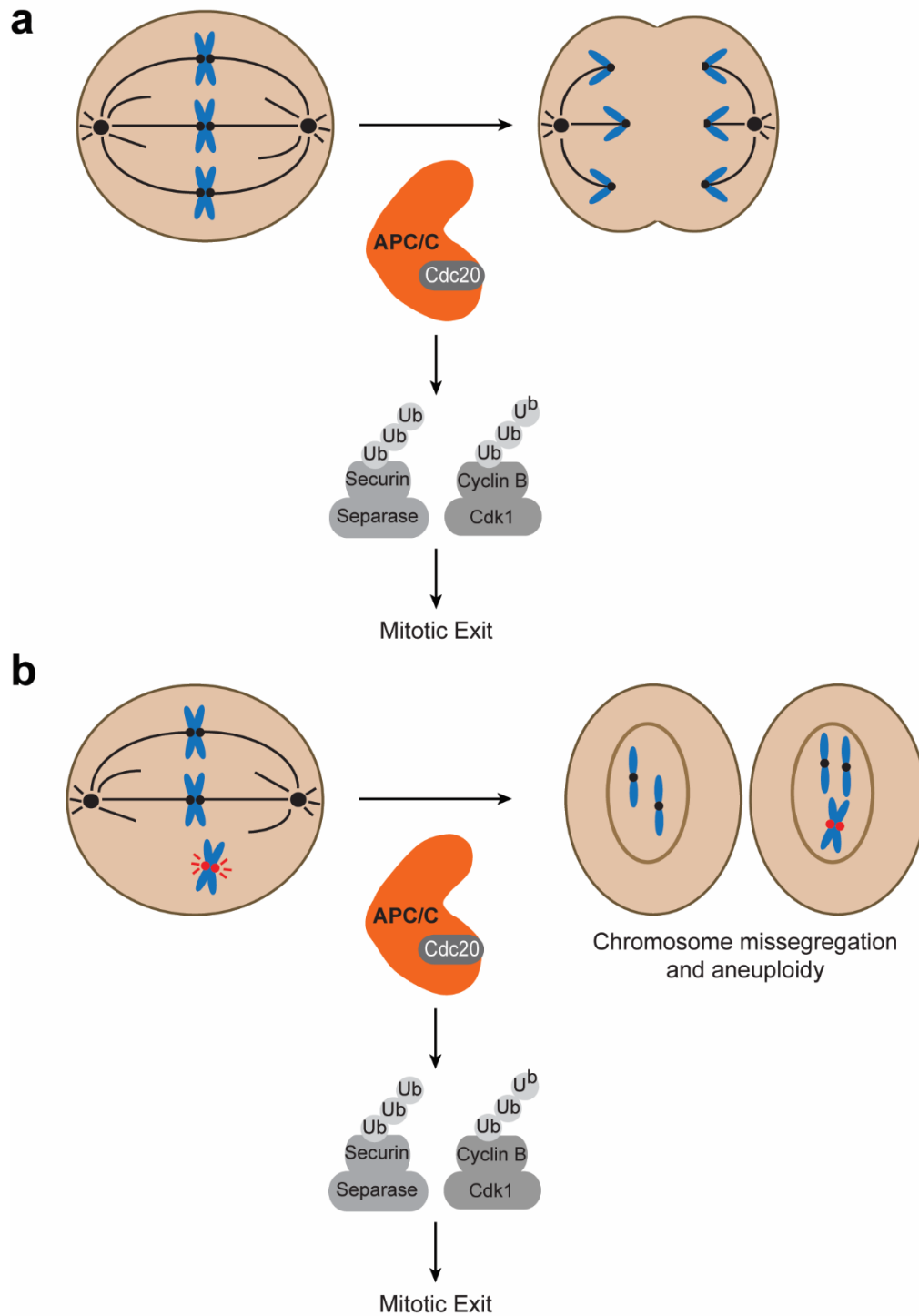


**Figure 1: Metaphase to anaphase transition is activated by APC/C<sup>Cdc20</sup>.** (a) When chromosomes achieve bipolar attachment to the mitotic spindle, APC/C<sup>Cdc20</sup> is activated to ubiquitinate cyclin b and securin. (b) Premature activation of APC/C<sup>Cdc20</sup> leads to chromosome missegregation and aneuploidy.

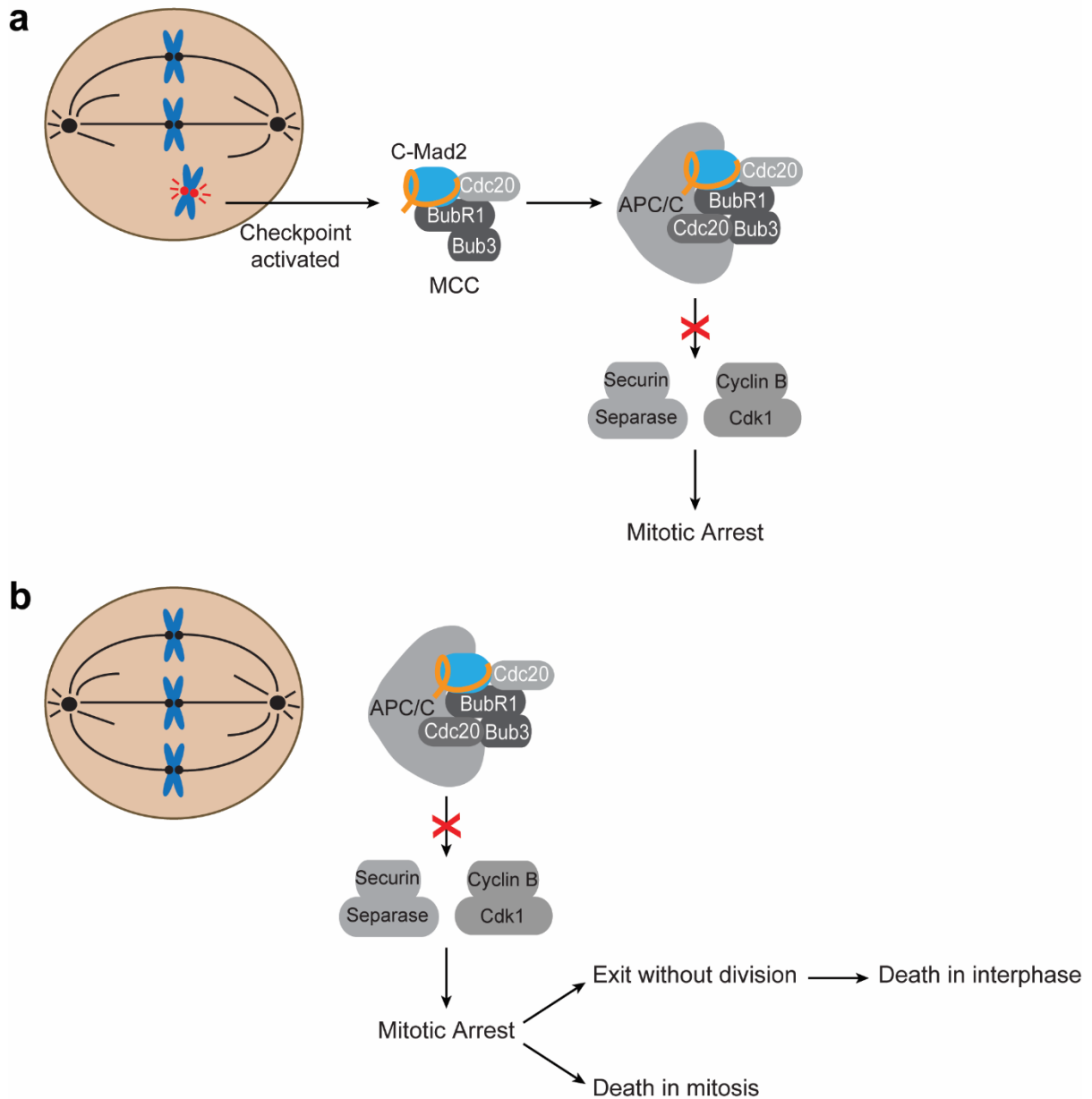


**Figure 2: APC/C<sup>Cdc20</sup> is inhibited by the mitotic checkpoint complex (MCC).** (a) The MCC binds to and inhibits APC/C<sup>Cdc20</sup>. (b) Prolonged inhibition of APC/C<sup>Cdc20</sup> and mitotic arrest leads to cell death.

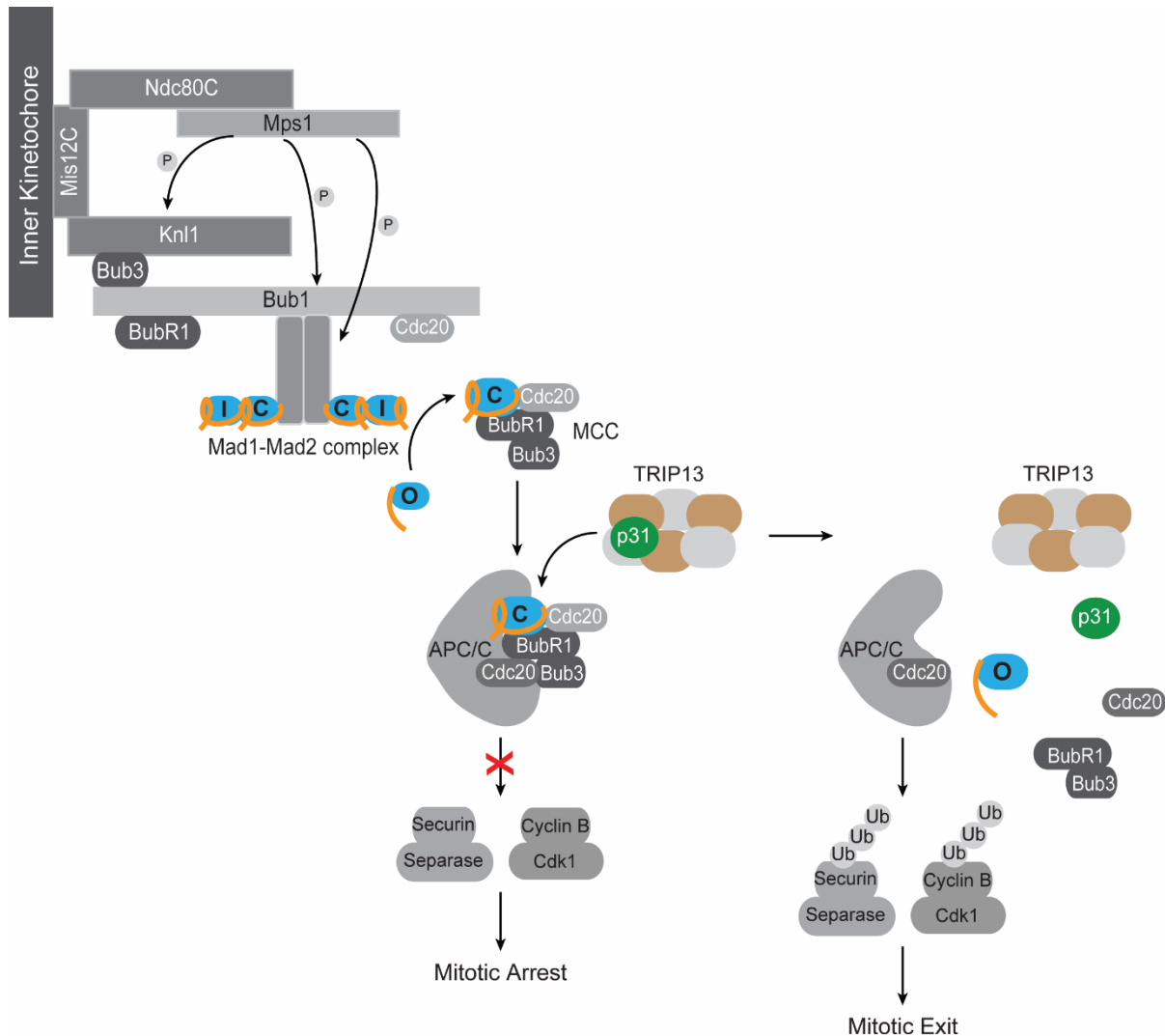


**Figure 3: Kinetochore recruitment of spindle checkpoint proteins, mitotic checkpoint complex (MCC) assembly, and spindle checkpoint silencing.** The Knl1/Mis12C/Ndc80C (KMN) complex serves as a platform for the recruitment of spindle checkpoint proteins. The master regulatory kinase of checkpoint protein recruitment is Mps1. Mps1 phosphorylates Knl1, providing docking sites for Bub3/Bub1. Mps1 then phosphorylates Bub1. Bub1 recruits BubR1, the Mad1-Mad2 complex, and Cdc20. Mad1-Mad2 is phosphorylated by Mps1, and this provides further interaction with Cdc20 (not shown). The Mad1-Mad2 catalyzes the conformational change of O-Mad2 to I-Mad2, priming Mad2 for integration into the MCC as C-Mad2. The recruitment of the MCC proteins and conversion of Mad2 lead to the formation of the MCC, which inhibits APC/C, causing mitotic arrest at metaphase. During checkpoint silencing, TRIP13 with its adaptor protein, p31<sup>comet</sup>, catalyzes the conversion of C-Mad2 to O-Mad2, leading to disassembly of the MCC and mitotic exit.

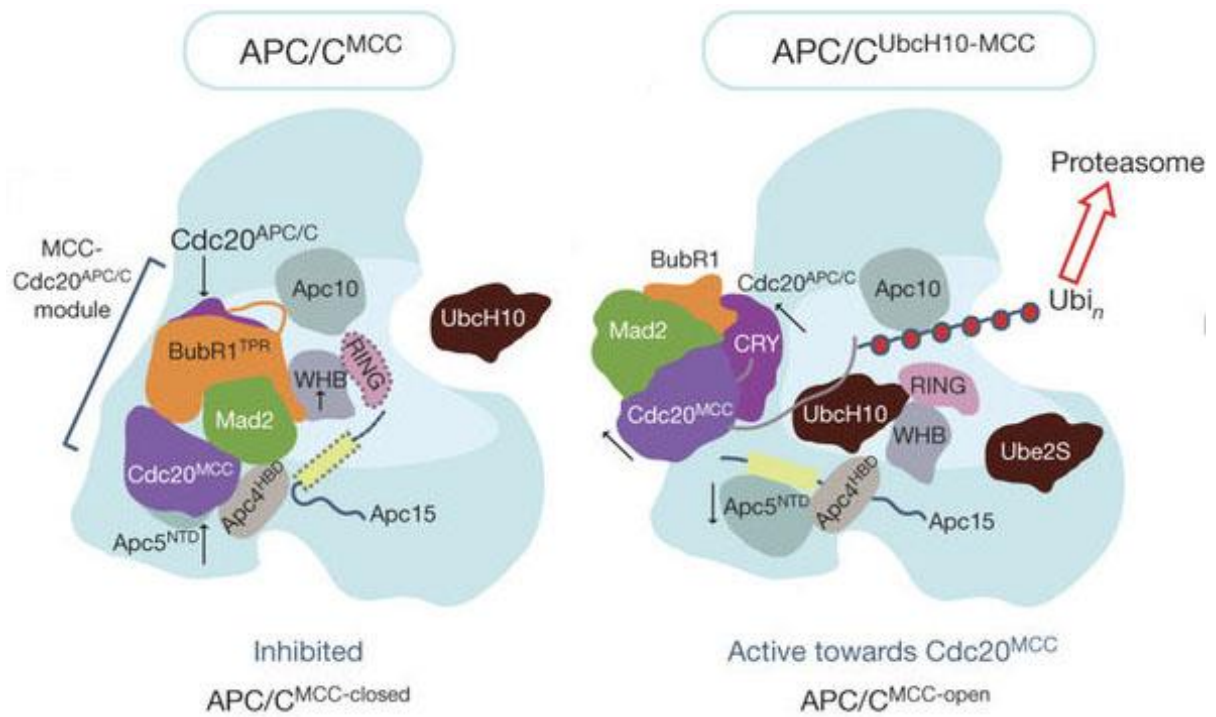


**Figure 4: Comparison of the structures of APC/C<sup>MCC-closed</sup> and APC/C<sup>MCC-open</sup>.** (Adapted from Alfieri et al., 2016.) In APC/C<sup>MCC-closed</sup>, the structure of Apc15 is disordered and the TPR domain of the BubR1 subunit of MCC blocks Ubch10 from accessing Cdc20<sup>MCC</sup> for ubiquitination. In APC/C<sup>MCC-open</sup>, Apc15 is well-defined and MCC-Cdc20<sup>APC/C</sup> is rotated to allow Cdc20<sup>MCC</sup> to bind Ubch10. Cdc20<sup>MCC</sup> is ubiquitinated, and undergoes proteasome degradation.

## CHAPTER TWO

### Materials and Methods

#### PROTEIN EXPRESSION AND PURIFICATION

##### TRIP13

BL21 (DE3)-T1 *E. coli* cells (Sigma) were transformed with plasmids encoding His<sub>6</sub>-tagged human TRIP13 WT or mutants, cultured in Terrific Broth until the OD<sub>600</sub> reached 1.0, and induced overnight at 18 °C with 0.2 mM isopropyl β-D-1-thiogalactopyranoside (IPTG). Harvested cells were resuspended in the TRIP13 Purification Buffer [50 mM NaH<sub>2</sub>PO<sub>4</sub>·2H<sub>2</sub>O pH 8.0, 300 mM NaCl, 5 mM MgCl<sub>2</sub>, 10% glycerol, 5 mM β-mercaptoethanol (BME), 200 μM ATP] supplemented with 20 mM imidazole and 1 mM phenylmethylsulfonyl fluoride (PMSF) and lysed. The cleared lysate was incubated with Ni<sup>2+</sup>-NTA Agarose beads (Qiagen). Beads were washed with the TRIP13 Purification Buffer supplemented with 50 mM imidazole, and eluted with the TRIP13 Purification Buffer supplemented with 250 mM imidazole. The proteins were incubated with TEV for overnight to remove the His<sub>6</sub> tag, and fractionated on a Resource Q™ column (GE) with the TRIP13 Purification Buffer containing 50 mM NaCl as the starting buffer, and the TRIP13 Purification Buffer containing 1 M NaCl as the elution buffer. TRIP13 proteins were further purified on the HiLoad 16/600 Superdex 200 gel filtration column (GE) in the buffer containing 20 mM HEPES pH 7.7, 100 mM KCl, 5 mM MgCl<sub>2</sub>, 5% glycerol, 1 mM DTT. The proteins were concentrated with Centriprep™ Concentrators (Millipore) and stored at -80 °C.

**p31<sup>comet</sup> and Mad2** *$\Delta$ N35-p31<sup>comet</sup>-Mad2<sup>L13A</sup> and Mad2*

His<sub>6</sub>- $\Delta$ N35-p31<sup>comet</sup>-Mad2<sup>L13A</sup> complex and His<sub>6</sub>-Mad2 (containing the C79S and C106S mutations to avoid disulfide formation *in vitro*) were expressed in BL21 (DE3)-T1 cells. Harvested cells were lysed in the Mad2 Purification Buffer (50 mM Tris, pH 8.0, 300 mM NaCl, 5 mM BME) supplemented with 1 mM PMSF. The cleared lysates were incubated with Ni<sup>2+</sup>-NTA Agarose beads (Qiagen). Beads were washed with the Mad2 Purification Buffer supplemented with 10 mM imidazole, and with the MOPS Buffer (50 mM MOPS pH 7.2, 300 mM NaCl, 5 mM BME) supplemented with 25 mM imidazole. Proteins were eluted with the MOPS Buffer supplemented with 200 mM imidazole, and exchanged into the MOPS Buffer with no imidazole with PD-10 Desalting Columns (GE). The His<sub>6</sub>-tag of the  $\Delta$ N35-p31<sup>comet</sup>-Mad2<sup>L13A</sup> complex was cleaved by TEV, whereas His<sub>6</sub>-Mad2 was not cleaved. The proteins were purified with the Resource Q column with the MOPS Buffer containing 75 mM NaCl as the binding buffer, and the MOPS Buffer containing 1 M NaCl as the elution buffer. The proteins were concentrated and further purified with the Superdex 200 Increase 10/300 GL column (GE) in a buffer containing 25 mM Tris pH 7.5, 200 mM NaCl, 10% glycerol, and 1 mM tris(2-carboxyethyl)phosphine (TCEP).

 *$\Delta$ N35-p31<sup>comet</sup>*

His<sub>6</sub>- $\Delta$ N35-p31<sup>comet</sup> was expressed in M15[pRep4] *E. coli* cells. Cells were lysed in the buffer containing 50 mM MOPS pH 7.2, 150 mM NaCl, 5 mM BME, 10 mM imidazole. After

purification with Ni<sup>2+</sup>-NTA Agarose beads and TEV cleavage, the protein was further purified with the Resource Q column with the binding buffer of 20 mM HEPES pH 7.5, 50 mM NaCl, 10% glycerol, and 1 mM DTT and the elution buffer of 20 mM HEPES pH 7.5, 1 M NaCl, 10% glycerol, and 1 mM DTT. The protein was further purified by gel filtration in the buffer containing 20 mM HEPES pH 7.5, 200 mM NaCl, 10% glycerol, and 1 mM DTT.

### *Mad2*<sup>R133A</sup>

His<sub>6</sub>-Mad2<sup>R133A</sup> was expressed in M15[pRep4] cells in M9 minimal media containing <sup>15</sup>N-NH<sub>4</sub>Cl as the sole nitrogen source. Cells were harvested in the R133A Buffer (50 mM sodium phosphate pH 8.0, 300 mM NaCl, 5 mM BME) supplemented with 10 mM imidazole, lysed by sonication, and cleared by centrifugation. The lysate was incubated with Ni<sup>2+</sup>-NTA Agarose beads (Qiagen). Beads were washed with the R133A Buffer supplemented with 10 mM imidazole, followed by the R133A Buffer supplemented with 20 mM imidazole. The protein was eluted with the R133A Buffer supplemented with 250 mM imidazole. The protein was dialyzed into the buffer containing 50 mM Tris pH 8.0, 100 mM NaCl, 1 mM DTT, and cleaved overnight with TEV to remove the His<sub>6</sub>-tag. The cleaved protein was purified with the Resource Q<sup>TM</sup> column (GE) with the binding buffer of 20 mM Tris pH 8.0, 50 mM NaCl, and 1 mM DTT, and the elution buffer of 20 mM Tris pH 8.0, 1 M NaCl, and 1 mM DTT. The protein was further purified with the Superdex 75 10/300 GL column (GE) in a buffer containing 50 mM sodium phosphate pH 6.8, 300 mM KCl, and 1 mM DTT.

### *ΔN10-Mad2*

His<sub>6</sub>-ΔN10-Mad2 was expressed in M15[pRep4] cells in Luria Broth. Harvested cells were lysed in the ΔN10 Purification Buffer (50 mM NaH<sub>2</sub>PO<sub>4</sub>·2H<sub>2</sub>O, pH 7.8, 300 mM NaCl) supplemented with 1 mM DTT, 1 mM PMSF, and 1X cComplete™, EDTA-free Protease Inhibitor (Sigma). The cleared lysates were incubated with Ni<sup>2+</sup>-NTA Agarose beads (Qiagen). Beads were washed with the ΔN10 Purification Buffer, with ΔN10 Wash Buffer (50 mM NaH<sub>2</sub>PO<sub>4</sub>·2H<sub>2</sub>O pH 6.0, 300 mM NaCl, 10% glycerol), and with ΔN10 Wash Buffer supplemented with 20 mM imidazole. Proteins were eluted with ΔN10 Wash Buffer supplemented with 500 mM imidazole, and exchanged with PD-10 Desalting Columns (GE) into buffer containing 25 mM Tris, pH 8.0, 100 mM NaCl, 1 mM DTT. The His<sub>6</sub>-tag was not cleaved. The protein was diluted 2.5x with water and purified with the Mono Q column with buffer containing 25 mM Tris, pH 7.5, 50 mM NaCl, 3 mM DTT as the binding buffer, and buffer containing 25 mM Tris, pH 7.5, 1 M NaCl, 3 mM DTT as the elution buffer. The protein was concentrated and incubated overnight at 30°C to induce dimer formation. The protein was further purified with the Superdex 200 Increase 10/300 GL column (GE) in a buffer containing 25 mM Tris pH 7.5, 200 mM NaCl, and 3 mM DTT.

### **Cdc20**

Expression of Cdc20N-His<sub>6</sub> (residues 1-170 of human Cdc20) in BL21 (DE3) cells was induced with 1 mM IPTG for 6 hrs at 37 °C. The harvested cells were lysed in 8 M urea, 100 mM NaH<sub>2</sub>PO<sub>4</sub>, and 10 mM Tris at pH 8.0 for overnight at room temperature. The lysate was sonicated, cleared by centrifugation, and incubated with Ni<sup>2+</sup>-NTA Agarose beads (Qiagen).

The beads were washed with 8 M urea, 100 mM NaH<sub>2</sub>PO<sub>4</sub>, and 10 mM Tris at pH 6.3, and eluted with 8 M urea, 100 mM NaH<sub>2</sub>PO<sub>4</sub>, and 10 mM Tris at pH 4.5. The protein was dialyzed into the buffer containing 25 mM Tris pH 8.0, 300 mM NaCl, 5% glycerol, and 1 mM BME.

### **p97/VCP**

For p97/VCP purification, BL21 (DE3) *E. coli* cells were transformed with plasmids encoding His<sub>6</sub>-tagged human p97/VCP, cultured in Luria Broth until the OD<sub>600</sub> reached 0.6, and induced overnight at 18 °C with 0.2 mM isopropyl β-D-1-thiogalactopyranoside (IPTG). Harvested cells were resuspended in p97/VCP Lysis Buffer [100 mM Tris pH 7.4, 500 mM KCl, 5 mM MgCl<sub>2</sub>, 20 mM imidazole, 5% glycerol, 2 mM β-mercaptoethanol (BME)]. The cleared lysate was incubated with Ni<sup>2+</sup>-NTA Agarose beads (Qiagen). Beads were washed with p97/VCP Purification Buffer [50 mM HEPES pH 7.4, 150 mM KCl, 5 mM MgCl<sub>2</sub>, 2 mM β-mercaptoethanol (BME)] supplemented with 50 mM imidazole, and then with p97/VCP Purification Buffer supplemented with 100 mM imidazole. The protein was eluted with the p97/VCP Purification Buffer supplemented with 300 mM imidazole, and diluted 3-fold with p97/VCP Purification buffer with no imidazole. The protein was incubated with TEV for overnight to remove the His<sub>6</sub> tag. p97/VCP protein was concentrated and further purified on the Superdex 200 Increase 10/300 GL gel filtration column (GE) in the buffer containing 20 mM HEPES pH 7.4, 250 mM KCl, 1 mM MgCl<sub>2</sub>, 5% glycerol, 1 mM DTT. The protein was concentrated and stored at -80 °C.

## NMR SPECTROSCOPY

All NMR experiments were recorded on Agilent DD2 600 MHz spectrometer at 30 °C. To obtain uniformly  $^{15}\text{N}$ -labeled Mad2<sup>R133A</sup>, we used M9 minimal media with  $^{15}\text{NH}_4\text{Cl}$  as the sole nitrogen source (1 g/L). Purified  $^{15}\text{N}$ -Mad2 R133A was incubated overnight at room temperature before the NMR experiments to ensure that the two forms of Mad2 have reached equilibrium (Luo et al., 2004). The final NMR samples contained 140  $\mu\text{M}$   $^{15}\text{N}$ -Mad2<sup>R133A</sup> (after overnight pre-incubation) with or without 4.3  $\mu\text{M}$   $\Delta\text{N35-p31}^{\text{comet}}$  and 0.43  $\mu\text{M}$  TRIP13 dissolved in a buffer containing 25 mM Tris, pH 7.5, 300 mM KCl, 1 mM  $\text{MgCl}_2$ , 1 mM DTT and 5%  $\text{D}_2\text{O}$ . ATP was added to the  $^{15}\text{N}$ -Mad2<sup>R133A</sup>- $\Delta\text{N35-p31}^{\text{comet}}$ -TRIP13 sample at a final concentration of 1 mM. For monitoring the conformational change of Mad2, a series of 2D  $^1\text{H}$ - $^{15}\text{N}$  HSQC spectra each lasting 2 hrs 34 min were acquired for a total acquisition time of 40 hrs.

For  $^1\text{H}/^2\text{H}$  (H/D) exchange experiments, the final NMR samples were lyophilized and dissolved in 100%  $\text{D}_2\text{O}$ , and contained 150  $\mu\text{M}$   $^{15}\text{N}$ -Mad2<sup>R133A</sup> in a buffer containing 25 mM Tris, pH 7.5, 200 mM NaCl, 5 mM  $\text{MgCl}_2$ , and 1 mM DTT. After the acquisition of a 2D  $^1\text{H}$ - $^{15}\text{N}$  HSQC spectrum lasting 2 hrs 34 min, ATP (0.1 M in  $\text{D}_2\text{O}$ ) and the TRIP13- $\Delta\text{N35-p31}^{\text{comet}}$  complex were added into the Mad2<sup>R133A</sup>  $\text{D}_2\text{O}$  sample to final concentrations of 5 mM and 1.5  $\mu\text{M}$ , respectively. A series of 2D  $^1\text{H}$ - $^{15}\text{N}$  HSQC spectra each lasting 2 hours 34 min were acquired for a total acquisition time of 24 hrs. All data were processed with NMRpipe (Delaglio et al., 1995) and analyzed with NMRView (Johnson and Blevins, 1994).

## X-RAY CRYSTALLOGRAPHY

### Crystallization, data collection and structure determination

His<sub>6</sub>-TRIP13<sup>E253A</sup> ΔC2 (with the C-terminal two residues deleted) was expressed in BL21(DE3) cells, and purified using Ni<sup>2+</sup>-NTA Agarose resin pre-equilibrated with the lysis buffer (50 mM phosphate, pH 7.5, 300 mM NaCl, 40 mM imidazole, and 5 mM BME). After cleavage by TEV to remove the His<sub>6</sub>-tag, the TRIP13<sup>E253A</sup> protein was further purified with a resource Q column followed by a Superdex 200 gel filtration column equilibrated with a buffer containing 20 mM phosphate, pH 8.0, 300 mM NaCl, and 0.5 mM TCEP. The purified protein was concentrated to 2 mg/mL. The ΔN35-p31<sup>comet</sup>-Mad2<sup>L13A</sup> complex was expressed and purified as previously described (Yang et al., 2007). TRIP13<sup>E253A</sup> and ΔN35-p31<sup>comet</sup>-Mad2<sup>L13A</sup> were mixed at 1:2 molar ratio in the presence of 200 μM ATP. The protein mixture was fractionated on a Superdex 200 column equilibrated with a buffer containing 20 mM Tris-HCl, pH 8.0, 100 mM NaCl, and 0.5 mM TCEP. The TRIP13<sup>E253A</sup>-ΔN35-p31<sup>comet</sup>-Mad2<sup>L13A</sup> complex was then concentrated to 5.5 mg/mL, and subjected to crystallization by the sitting-drop vapor diffusion method at 20 °C. The best crystals were obtained with a reservoir solution containing 0.1 M HEPES, pH 7.5, 0.2 M NaCl, and 4% (v/v) isopropanol. Crystals were cryo-protected by increasing the final concentration of glycerol to 30% (v/v) in a step-wise fashion and flash-cooled in liquid nitrogen.

The X-ray diffraction data were collected at beamline 19-ID (SBC-CAT) at the Advanced Photon Source (Argonne National Laboratory, Argonne, Illinois, USA). Data were processed in the program HKL3000 (Otwinowski and Minor, 1997). Initial phases were obtained by molecular replacement in the program Phase r(McCoy et al., 2007), using the

structure of *C. elegans* PCH-2 as a search model (PDB ID: 4XGU). Iterative model building and refinement were performed in the programs Coot (Emsley and Cowtan, 2004) and PHENIX (Adams et al., 2010), respectively. Although the TRIP13<sup>E253A</sup>– $\Delta$ N35-p31<sup>comet</sup>–Mad2<sup>L13A</sup> complex was used for crystallization in the presence of ATP, the final crystals only contained TRIP13<sup>E253A</sup> bound to ADP. Data collection and refinement statistics are summarized in Table 1.

### **Accession codes**

The coordinates of the human TRIP13–ADP structure have been deposited to the Protein Data Bank with the PDB ID: 5WC2.

## **ATPASE ASSAYS**

### **ADP-Glo™ Kinase Assay**

All reactions were performed in white OptiPlate-384 plates (Perkin Elmer) at room temperature. TRIP13 and  $\Delta$ N35-p31<sup>comet</sup>–Mad2<sup>L13A</sup> were diluted in the Reaction Buffer (25 mM Tris pH 7.5, 200 mM NaCl, 10 mM MgCl<sub>2</sub>, 1 mM DTT, 5% glycerol, and 0.05% Tween) to a final volume of 5  $\mu$ L, and incubated for 15 min. ATP was added to the reaction to a final volume of 10  $\mu$ L and a final concentration of 0.1 mM, and incubated for 1 hr. 10  $\mu$ L Glo Reagent from the ADP-Glo™ Kinase Assay kit (Promega) was added to the reaction, and incubated for 40 min. 20  $\mu$ L Detect reagent from the kit was added to the reaction, and incubated for 30 min. Luminescence was detected with the VICTOR 3V Multilabel Plate Reader (Perkin Elmer). A standard curve was prepared according to the ADP-Glo™ kit

instructions to calculate the concentration of ADP based on luminescence. All data were normalized to the reading of the sample containing the Reaction Buffer alone with no proteins. The best results were obtained when the ADP-Glo™ kit reagents were diluted two-fold with the Reaction Buffer. Different standard curves were used for undiluted versus diluted reagents.

### **Kinase Glo® ATPase Assay**

All reactions were performed in white OptiPlate-384 plates (Perkin Elmer) at room temperature. TRIP13 was diluted in the Reaction Buffer (25 mM Tris pH 7.5, 200 mM NaCl, 10 mM MgCl<sub>2</sub>, 1 mM DTT, 5% glycerol, and 0.05% Tween) to a final volume of 10 μL. ATP was added to the reaction to a final volume of 20 μL and a final concentration of 0.01 mM, and incubated for 2 hr. 6.7 μL Kinase-Glo® Reagent from the Kinase-Glo® Luminescent Kinase Assay kit (Promega) was added to the reaction, and incubated for 20 min. Luminescence was detected with the VICTOR 3V Multilabel Plate Reader (Perkin Elmer). A standard curve was prepared according to the Kinase-Glo® kit instructions to calculate the concentration of ATP based on luminescence. All data were normalized to the reading of the sample containing the Reaction Buffer alone with no proteins.

## **MAD2 DISSOCIATION AND BINDING ASSAYS**

The MBP1 peptide (with the sequence of SWYSYPPPQRAVC) was synthesized at the Protein Chemistry Technology Core at University of Texas Southwestern Medical Center (UTSW). MBP1 or Cdc20N was coupled to SulfoLink™ Coupling Resin (Thermo Fisher) according to the manufacturer's instructions. Beads were washed in the ATPase Reaction Buffer. His<sub>6</sub>-

Mad2 (0.5 mg/mL) was incubated with the beads for 30-60 min. After washing with the ATPase Reaction Buffer, TRIP13 and  $\Delta$ N35-p31<sup>comet</sup> at indicated concentrations and 1 mM ATP were added to the beads and incubated for another 30-60 min. Proteins bound to beads were dissolved in SDS sample buffer, analyzed by SDS-PAGE, and stained with Coomassie blue. The Mad2-binding assay was performed in a similar manner except that ATP $\gamma$ S was used in place of ATP. All reactions were performed in the Reaction Buffer at room temperature. Note that the  $\Delta$ N10-Mad2 binding assay was performed with the wild-type Mad2 used in the APC/C assay (see below) and with  $\Delta$ N10-Mad2, not with His<sub>6</sub>-Mad2 as above. All other parameters are the same.

### **ANALYTICAL ULTRACENTRIFUGATION**

All analytical ultracentrifugation (AUC) experiments were performed in the sedimentation velocity (SV) mode at 4 °C in an Optima XL-I ultracentrifuge (Beckman-Coulter, Indianapolis, IN). Samples (400  $\mu$ L) were introduced into the sample sectors of chilled, charcoal-filled dual-sector Epon centerpieces that had been sandwiched between sapphire windows in standard AUC cell housings. An equal volume of AUC buffer (10 mM HEPES, pH 7.4, 300 mM NaCl, 5 mM MgCl<sub>2</sub>, 1.357 M glycerol, and 1 mM TCEP) was placed in the reference sectors. One sample of monomeric bovine serum albumen (BSA, Sigma-Aldrich, St. Louis, MO) was also centrifuged to serve as a molar-mass standard, determining whether the calculated (see below) solution parameters were realistic. BSA had been purified over a Superdex 200 16/60 size-exclusion. When present, ATP or ATP $\gamma$ S was included at a concentration of 100  $\mu$ M in both the sample and reference buffers. The assembled cells were positioned in a chilled An50-Ti

rotor, which was then put into the centrifuge and incubated at the experimental temperature under vacuum overnight. Next, the rotor was accelerated to 50,000 rpm and concentration profiles were collected using the onboard absorbance optics tuned to 280 nm. Data were collected until there was no evidence of sedimentation. Solution parameters (density, viscosity) were calculated in SEDNTERP (Laue et al., 1992). Using SEDFIT (Schuck, 2000) and the  $c(s)$  methodology, we calculated the molar mass of BSA, which was within 10% of the known value (66,430 Da). Thus, the calculated solution parameters were deemed acceptable, and SEDFIT was used to analyze the TRIP13 samples. Maximum-entropy regularization with a confidence level of 0.683 was used, and time-invariant noise elements in the data were subtracted (Schuck and Demeler, 1999). An  $s$ -resolution of 100 was used. All sedimentation coefficients were converted to standard conditions (water, 20 °C) using GUSI (Brautigam, 2015).

### **APC/C UBIQUITINATION ASSAY**

BubR1N (residues 1-370), His<sub>6</sub>-Cdc20 full-length, and dimeric Mad2 used in the APC/C assays were purified as previously described (Ji et al., 2017). Uba1, UbcH10, and Securin-Myc were purified as previously described (Tang and Yu, 2004). Ube2S was a gift from Dr. Michael Rape (University of California at Berkeley). The APC/C assay was performed as previously described (Ji et al., 2017). In brief, APC/C was isolated from *Xenopus* egg extracts with anti-APC3 antibody-coupled Protein A beads (Bio-Rad). Each reaction contained 5  $\mu$ L of beads that were incubated with 50  $\mu$ L of extract. The beads were supplemented with 3.8  $\mu$ M His<sub>6</sub>-Cdc20 for 1 hr and washed. The minimal functional MCC was formed by an

incubation of BubR1N, Cdc20, and Mad2 for 20 min. APC/C<sup>Cdc20</sup> beads were incubated with the pre-formed MCC and washed. The ubiquitination reaction was performed in the presence of Securin-Myc for 30 min, and quenched with the SDS loading buffer. The reaction mixtures were analyzed by SDS-PAGE followed by immunoblotting with the anti-Myc antibody.

For TRIP13 inactivation of MCC, TRIP13 was diluted and mixed with p31<sup>comet</sup> and added to the MCC mixture in the presence of 5 mM MgCl<sub>2</sub> and 1 mM ATP. The final reaction volume was 8 μL. This reaction was incubated for 1 hr, and diluted to a final volume of 25 μL by the XB buffer (10 mM HEPES, pH 7.7, 100 mM KCl, 0.1 mM CaCl<sub>2</sub>, 1 mM MgCl<sub>2</sub>, and 50 mM sucrose) supplemented with 2 mg/mL BSA. The APC/C<sup>Cdc20</sup> beads (5 μL) were then added, and the APC/C ubiquitination assay was performed. In the case of MCC bound to APC/C, the MCC was first incubated with the APC/C<sup>Cdc20</sup> beads, and then the TRIP13 reaction was performed.

### **HIGH-THROUGHPUT SCREENING**

The ADP-Glo™ assay was performed as described above with the following changes: the protein, ATP, Glo reagent, and Detection reagent were dispensed using BioTek Microflo Dispenser (BioTek). Compounds were dispensed using the Echo 555 Liquid Handler (Labcyte) from an initial concentration of 5 mM to the final concentrations mentioned in the text. Luminescence was detected using the EnVision Multilabel Plate Reader (Perkin Elmer). Results were analyzed by Anwu Zhou in the high-throughput screening core.

### **ASSAY FOR THE GENERATION OF HYDROGEN PEROXIDE**

The hydrogen peroxide (H<sub>2</sub>O<sub>2</sub>) assay was performed as previously described (Johnston et al., 2008). All reactions were performed in Greiner 384 well plates, polystyrene (Sigma cat. No. M3311). In brief, compounds were diluted in Hank's Balanced Salt Solution (HBSS – Hyclone) to a final concentration of 3 μM or 60 μM, and dispensed at 20 μL per well. ATPase Reaction Buffer (25 mM Tris pH 7.5, 200 mM NaCl, 10 mM MgCl<sub>2</sub>, 1 mM DTT, 5% glycerol, and 0.05% Tween) was added at 20 μL per well, and incubated with the compound for 1 hr at room temperature. HRP-PR detection solution (180 μg/uL horseradish peroxidase, 300 μg/mL phenol red in HBSS) was added at 20 μL per well, and incubated for 5 min at room temperature. 10 μL of 1 N NaOH was added to each well, and incubated for 5 min at room temperature. Absorbance was detected at 610 nm on SpectraMax Plus 384 Microplate Reader (Molecular Devices).

**Table 1. Data Collection and Refinement Statistics for human TRIP13<sup>E253A/ΔC2</sup>**

Data Collection	
Crystal	Native
Space group	P6 <sub>5</sub>
Wavelength (Å)	0.97918
Cell dimensions	
<i>a</i> , <i>b</i> , <i>c</i> (Å)	98.37, 98.37, 122.11
$\alpha$ , $\beta$ , $\gamma$ (°)	90.00, 90.00, 120.00
Resolution range (Å)	40.00 – 2.50 (2.54 – 2.50) <sup>a</sup>
Unique reflections	23,254 (1,163)
Multiplicity	15.2 (10.9)
Data completeness (%)	100.0 (99.9)
R <sub>merge</sub> (%) <sup>b</sup>	7.9 (148.5)
R <sub>pim</sub> (%) <sup>c</sup>	2.1 (46.1)
I/σ(I)	40.6 (2.0)
Wilson <i>B</i> -value (Å <sup>2</sup> )	32.77
Refinement Statistics	
Resolution range (Å)	32.20 – 2.50 (2.61 – 2.50)
No. of reflections R <sub>work</sub> /R <sub>free</sub>	21,458/1,081 (1,349/73)
Data completeness (%)	92.4 (49.0)
Atoms (non-H protein/solvent/ligand)	2,895/138/27
R <sub>work</sub> (%)	18.8 (23.7)
R <sub>free</sub> (%)	22.6 (29.4)
R.m.s.d. bond length (Å)	0.003
R.m.s.d. bond angle (°)	0.615
Mean <i>B</i> -value (Å <sup>2</sup> ) (protein/solvent/ligand)	48.0/43.6/26.0
Ramachandran plot (%) (favored/additional/disallowed) <sup>d</sup>	98.02/1.69/0.28

<sup>a</sup>Data for the highest-resolution shell are shown in parentheses.

<sup>b</sup>R<sub>merge</sub> = 100  $\sum_h \sum_i |I_{h,i} - \langle I_h \rangle| / \sum_h \sum_i \langle I_{h,i} \rangle$ , where the outer sum (*h*) is over the unique reflections and the inner sum (*i*) is over the set of independent observations of each unique reflection.

<sup>c</sup>R<sub>pim</sub> = 100  $\sum_h \sum_i [1/(n_h - 1)]^{1/2} |I_{h,i} - \langle I_h \rangle| / \sum_h \sum_i \langle I_{h,i} \rangle$ , where *n<sub>h</sub>* is the number of observations of reflections *h*.

<sup>d</sup>As defined by the validation suite MolProbity.

## **CHAPTER THREE**

### **Mechanistic Insight into TRIP13-catalyzed Mad2 Structural Transition and Spindle Checkpoint Silencing**

#### **INTRODUCTION**

The spindle checkpoint is a cell-cycle surveillance system that ensures proper chromosome segregation in mitosis (Jia et al., 2013; London and Biggins, 2014b; Musacchio, 2015). Activated by unattached kinetochores, checkpoint proteins collaborate to inhibit the anaphase-promoting complex or cyclosome bound to its mitotic activator Cdc20 (APC/C<sup>Cdc20</sup>) (Chang and Barford, 2014; Kim and Yu, 2011; Sivakumar and Gorbsky, 2015; Yu, 2007), thus arresting cells in prometaphase until all chromosomes achieve bipolar attachment to spindle microtubules. A major effector of the spindle checkpoint is the mitotic checkpoint complex (MCC), which consists of the constitutive BubR1–Bub3 heterodimer, Cdc20, and Mad2 (Fang, 2002; Izawa and Pines, 2015; Sudakin et al., 2001; Tang et al., 2001). MCC binds to the substrate-binding site of APC/C<sup>Cdc20</sup>, preventing it from recognizing and ubiquitinating securin and cyclin B1 (Alfieri et al., 2016; Izawa and Pines, 2015; Lara-Gonzalez et al., 2011; Yamaguchi et al., 2016). Stabilization of securin and cyclin B1 delays sister-chromatid separation and mitotic exit.

A rate-limiting step in MCC formation is the conformational activation of the checkpoint protein Mad2 (Luo and Yu, 2008; Mapelli and Musacchio, 2007). Mad2 is an unusual protein with multiple folded conformers, including the latent open conformer (O-Mad2) and the active closed conformer (C-Mad2) (De Antoni et al., 2005; Luo et al., 2000; Luo et al., 2002; Luo et al., 2004; Sironi et al., 2002) (Fig. 5a). C-Mad2 can bind to Mad1, Cdc20, and other proteins through the Mad2-interaction motif (MIM) (Choi et al., 2016; Luo

et al., 2002; Sironi et al., 2002; Yu, 2007). O-Mad2 and C-Mad2 share the same stably folded core that consists of three  $\alpha$  helices sandwiched by three central  $\beta$  strands on one side and a twisted  $\beta$  hairpin on the other. They differ in their N- and C-terminal regions. When bound to a ligand, the C-terminal region of C-Mad2 wraps around the MIM and stretches across the core like a “safety belt” (Fig. 5a, right panel) (Hara et al., 2010; Kim et al., 2014; Luo et al., 2004; Rosenberg and Corbett, 2015; Sironi et al., 2002). Mad2 forms a constitutive complex with Mad1, in which Mad2 adopts the C-Mad2 conformation (Sironi et al., 2002). The C-terminal region of O-Mad2 does not form the safety belt and blocks the ligand-binding site (Fig. 5a, left panel). Because C-Mad2 is thermodynamically more stable than O-Mad2, O-Mad2 alone, in the absence of a ligand, can spontaneously convert to the unliganded C-Mad2 conformation, in which the safety belt is formed but does not trap a ligand (Luo et al., 2004; Yang et al., 2008) (Fig. 5a, middle panel).

Unattached kinetochores promote Mad2 activation and MCC formation through a series of signaling and recruitment events (Jia et al., 2013; London and Biggins, 2014b; Musacchio, 2015). The KMN network of proteins (consisting of Knl1–Zwint, the Ndc80 complex, and the Mis12 complex) serves both as a major microtubule receptor and as a docking platform for checkpoint proteins at outer kinetochores (Bharadwaj et al., 2004; Cheeseman et al., 2006; Hiruma et al., 2015; Ji et al., 2015; Kiyomitsu et al., 2007; Krenn et al., 2014; London et al., 2012; Martin-Lluesma et al., 2002; Primorac et al., 2013; Sheppard et al., 2012; Vleugel et al., 2013; Yamagishi et al., 2012; Zhang et al., 2014), and is required for spindle checkpoint signaling (Kim and Yu, 2015). When kinetochores are not attached by microtubules, the Ndc80 complex (Ndc80C) is phosphorylated by Aurora B and recruits the checkpoint kinase

Mps1 (Hiruma et al., 2015; Ji et al., 2015). Mps1 phosphorylates Knl1, providing docking sites for the Bub1–Bub3 complex (Kiyomitsu et al., 2007; Krenn et al., 2014; London et al., 2012; Primorac et al., 2013; Shepperd et al., 2012; Vleugel et al., 2013; Yamagishi et al., 2012; Zhang et al., 2014). Bub1–Bub3 phosphorylated by Mps1 and Cdk1 further recruits the Mad1–C-Mad2 complex, and other MCC components BubR1–Bub3 and Cdc20 (Di Fiore et al., 2015; Diaz-Martinez et al., 2015; Ji et al., 2017; Jia et al., 2016; Kang et al., 2008; London and Biggins, 2014a; Mora-Santos et al., 2016; Moyle et al., 2014; Overlack et al., 2015). The Mad1–C-Mad2 complex at kinetochores recruit additional O-Mad2 from the cytosol and converts it to a high-energy intermediate form (I-Mad2) (De Antoni et al., 2005; Hara et al., 2015; Mapelli et al., 2007). I-Mad2 is passed onto Cdc20 to form the Cdc20–C-Mad2 complex, which then associates with BubR1–Bub3 to produce MCC (Faesen et al., 2017; Hara et al., 2015; Kulukian et al., 2009). Once formed, the MCC diffuses away from kinetochores and inhibits APC/C<sup>Cdc20</sup> (Izawa and Pines, 2015; Ji et al., 2017).

Kinetochores attachment by microtubules inhibits binding of Mps1 to Ndc80C (Hiruma et al., 2015; Ji et al., 2015). This and other mechanisms reduce the levels and activities of Mps1 and downstream checkpoint components at the kinetochores. The C-Mad2-binding protein p31<sup>comet</sup> binds to the Mad1–C-Mad2 core and prevents further Mad2 conformational activation (Habu et al., 2002; Mapelli et al., 2006; Xia et al., 2004; Yang et al., 2007). These mechanisms collectively inhibit MCC formation. The existing MCC is then disassembled through APC/C-dependent ubiquitination of Cdc20 and through p31<sup>comet</sup>-mediated MCC disassembly, leading to APC/C<sup>Cdc20</sup> activation and anaphase onset (Foster and Morgan, 2012; Jia et al., 2011; Reddy et al., 2007; Teichner et al., 2011; Uzunova et al., 2012; Varetto et al.,

2011; Westhorpe et al., 2011). Recently, the AAA+ ATPase TRIP13 has been shown to collaborate with p31<sup>comet</sup> to promote MCC disassembly and checkpoint inactivation (Eytan et al., 2014; Marks et al., 2017; Miniowitz-Shemtov et al., 2015; Wang et al., 2014b; Ye et al., 2015). p31<sup>comet</sup> acts as an adaptor to recruit C-Mad2 to TRIP13. TRIP13 then induces the conformational change of C-Mad2 to O-Mad2 in a process that requires ATP hydrolysis (Ye et al., 2015). The mechanism by which TRIP13 converts C-Mad2 to O-Mad2 is not understood.

In this study, we confirm that, in the presence of p31<sup>comet</sup>, TRIP13 catalyzes the conversion of C-Mad2 to O-Mad2 using nuclear magnetic resonance (NMR) spectroscopy. Proton/deuterium (H/D) exchange experiments further show that TRIP13-catalyzed structural transition of Mad2 does not involve the global unfolding/refolding of Mad2, but rather entails local unfolding of minimally the C-terminal region. We have determined the crystal structure of human TRIP13 in its monomeric ADP-bound state, and identified TRIP13 residues critical for p31<sup>comet</sup>-Mad2 binding and for coupling ATP hydrolysis to Mad2 unfolding. Finally, we show that TRIP13-p31<sup>comet</sup> prevents inhibition of APC/C by MCC components *in vitro*, but does not restore APC/C activity after APC/C has already been inhibited by MCC. Our studies provide key insight into the mechanism of TRIP13-catalyzed conformational change of Mad2 and the molecular processes leading to spindle checkpoint silencing.

## RESULTS

### **TRIP13 and p31<sup>comet</sup> convert C-Mad2 to O-Mad2 without global unfolding of C-Mad2**

Aided by p31<sup>comet</sup>, TRIP13 has been shown to catalyze the conversion of C-Mad2 to O-Mad2, based on the different elution profiles of the two Mad2 conformers on anion exchange columns (Luo et al., 2004; Ye et al., 2015). To confirm that TRIP13 catalyzed the structural transition of Mad2 with a more definitive method, we performed NMR analysis of <sup>15</sup>N-labeled Mad2 in the presence or absence of TRIP13 and p31<sup>comet</sup>. For this purpose, we used the monomeric Mad2<sup>R133A</sup> mutant that retained strong binding to p31<sup>comet</sup> ( $K_d$  240 nM) and the ability to undergo the O–C structural transition (Luo et al., 2004; Xia et al., 2004). The <sup>1</sup>H-<sup>15</sup>N heteronuclear single quantum coherence (HSQC) spectrum of Mad2<sup>R133A</sup> (which had been incubated at 30°C for overnight) showed that it had adopted the C-Mad2 conformation (Fig. 5b and Fig. 6a). We then added ATP and sub-stoichiometric amounts of TRIP13 (1:325 molar ratio of TRIP13 hexamers to Mad2 monomers) and  $\Delta$ N35-p31<sup>comet</sup> (1:33 molar ratio of p31<sup>comet</sup> to Mad2) to the C-Mad2<sup>R133A</sup> sample, and acquired an HSQC spectrum after 5 h of incubation. The HSQC spectrum of the TRIP13-treated sample was completely different from that of the starting C-Mad2<sup>R133A</sup> sample, and perfectly matched that of O-Mad2<sup>R133A</sup> (Fig. 6a and Fig. 7c). Therefore, TRIP13–p31<sup>comet</sup> is sufficient to catalyze the conversion of unliganded C-Mad2 to O-Mad2 in the presence of ATP.

TRIP13 is a hexameric AAA+ ATPase with structural homology to the bacterial ClpX (Ye et al., 2015), an unfoldase that is thought to completely unfold and thread proteins through its central pore for degradation by ClpP (Glynn et al., 2009; Olivares et al., 2016). Because C-Mad2 and O-Mad2 share a common folded core with the same topology (Fig. 5a), TRIP13–

p31<sup>comet</sup> catalyzed C-Mad2–O-Mad2 conversion does not necessarily require the global unfolding of Mad2. Local unfolding of the C-terminal region of C-Mad2 can complete this conversion and, in the case of liganded C-Mad2, release the bound ligand. To test whether TRIP13-catalyzed structural transition of Mad2 involved global or local unfolding of Mad2, we performed H/D exchange NMR experiments. Amide protons that form hydrogen bonds in folded structural elements exchange slowly with solvent, and their NMR signals remain visible for hours after the protein is lyophilized and dissolved into D<sub>2</sub>O. In contrast, amide protons in loop regions or transiently folded regions that do not form stable hydrogen bonds exchange rapidly with solvent, and their NMR signals disappear in D<sub>2</sub>O.

As expected, the HSQC spectrum of C-Mad2<sup>R133A</sup> in a D<sub>2</sub>O solution for 2.5 hrs showed a set of slow-exchanging peaks that mostly belonged to residues in the stably folded core and strand  $\beta$ 9 (Fig. 7a,b). Strikingly, a set of slow-exchanging peaks remained at 6 hrs after the addition of TRIP13, p31<sup>comet</sup>, and ATP (Fig. 7c). The positions of these peaks matched those of peaks in O-Mad2<sup>R133A</sup>, indicating that C-Mad2 had been converted to O-Mad2 during the course of experiment. We still mapped these slow-exchanging amides onto the structure of C-Mad2 for comparison with those in the absence of TRIP13 and p31<sup>comet</sup>. The slow-exchanging amides in the presence of TRIP13 and p31<sup>comet</sup> belonged exclusively to residues in the folded core of Mad2 (Fig. 7d). The slow-exchanging amides on  $\beta$ 9 and alternating amides on  $\beta$ 5 that participated in hydrogen bonding with  $\beta$ 9 were no longer protected, indicating that the C-terminal region of C-Mad2 ( $\beta$ 8 and  $\beta$ 9) were expectedly unfolded during the structural transition. On the other hand, many amide protons in the Mad2 core ( $\beta$ 4-6 and  $\alpha$ A-C) were protected from exchange with solvent during the TRIP13-catalyzed structural transition from

C-Mad2 to O-Mad2, indicating that the structure core of Mad2 remained folded. These results clearly demonstrate that Mad2 does not undergo global unfolding during TRIP13-catalyzed structural conversion. Because the C-terminal region has to unfold and refold to allow C-Mad2 to convert to O-Mad2, the C-Mad2–O-Mad2 transition catalyzed by TRIP13–p31<sup>comet</sup> minimally involves the local unfolding of the C-terminal safety belt of C-Mad2. Because not all structural elements of C-Mad2 contain slow-exchanging residues (Fig. 7b), we cannot exclude the possibility of local unfolding of other structural elements, aside from the C-terminal region.

### **Crystal structure of human TRIP13 in its monomeric ADP-bound state**

The structure of PCH-2, the *C. elegans* homolog of TRIP13, has previously been determined, revealing an asymmetric hexameric architecture (Ye et al., 2015) (Fig. 8a). The asymmetry likely stems from the different nucleotide states of the six protomers. Only two of the six PCH-2 promoters are bound to ADP, whereas the rest are free of nucleotides (Ye et al., 2015). When viewed from the side, the PCH-2 hexamer forms a slightly curved structure with a convex face and a concave face (Fig. 8a), similar to ClpX (Olivares et al., 2016). The convex face in ClpX has been shown to bind to substrates, and has generally been referred to as the top face (Olivares et al., 2016). We will adopt this convention and refer to the convex surface of TRIP13 as the top face.

To understand how TRIP13 recognized p31<sup>comet</sup> and Mad2, we attempted to determine the structure of the human TRIP13–p31<sup>comet</sup>–Mad2 complex. We subjected human TRIP13 E253A mutant (which was deficient in ATP hydrolysis) bound to ATP and the p31<sup>comet</sup>–Mad2

complex to crystallization, and obtained diffracting crystals. Structure determination, however, revealed that the crystals contained TRIP13 alone in the monomeric ADP-bound state (Fig. 8b). Even though the ATPase-deficient mutant of TRIP13 was used in our studies, the residual ATPase activity of TRIP13 E253A presumably converted ATP to ADP, and contributed to the dissociation of the complex.

Structure of human TRIP13 bound to ADP is highly similar to that of the *C. elegans* PCH-2 promoter bound to ADP, with an RMSD of 1.57 Å for all atoms (Fig. 8b,c). Both contain an N-terminal domain (NTD), a large AAA+ subdomain, and a small AAA+ subdomain. ADP is bound at the interface between the large and small AAA+ subdomains. The NTD of human TRIP13 has a fold slightly different from that of PCH-2. In PCH-2 NTD, a single long, bent  $\alpha$  helix packs against a  $\beta$  sheet, whereas human TRIP13 NTD consists of two  $\alpha$  helices packing against the  $\beta$  sheet. The structures of the large and small AAA+ subdomains and their relative orientation are virtually identical between human TRIP13 and the ADP-bound protomer of *C. elegans* PCH-2. The only discernable difference is located at the so-called pore loop. This region forms a helix in the PCH-2 hexamer, but does not have visible electron density and is likely flexible in human TRIP13 monomer. The pore loop has been implicated in substrate binding and unfolding in other AAA+ ATPases (Iosefson et al., 2015; Olivares et al., 2016). The structural differences between human and *C. elegans* TRIP13 are consistent with the intrinsically dynamic nature of this loop. Because the human TRIP13 structure is monomeric and has a disordered pore loop, we used the structure of the *C. elegans* PCH-2 hexamer to guide our subsequent mutagenesis and biochemical studies.

## **Identification of TRIP13 residues critical for its p31<sup>comet</sup>-Mad2-stimulated ATPase activity**

To gain insight into the mechanism of TRIP13, we systematically mutated conserved residues in TRIP13 and studied the effects of these mutations on the ATPase activity, Mad2 unfolding, and binding to p31<sup>comet</sup>-Mad2. We describe our findings on the following mutants: W221A, F222A, K227A, K231E, N278A, and G320A. The recombinant mutant proteins were expressed in bacteria, and purified to reasonable purity (Fig. 9a).

We developed a high-throughput TRIP13 ATPase assay based on the ADP-Glo™ Kinase Assay kit from Promega, which used luminescence to measure the amount of ADP produced by ATP hydrolysis. ATP hydrolysis by TRIP13 wild type (WT) was dose-dependent, and the TRIP13 E253A mutant was deficient in ATP hydrolysis (Fig. 9b). TRIP13 E253A, however, had residual ATPase activity, explaining the fact that the structure of TRIP13 E253A was in the ADP-bound form even though it was crystallized in the presence of ATP. Consistent with a previous report (Ye et al., 2015), the ATPase activity of TRIP13 was stimulated by the p31<sup>comet</sup>-C-Mad2 complex, but not by either protein alone (Fig. 9c). Similar results were obtained when Mad2 was locked into the C-Mad2 conformation with the L13A mutation, with binding of the artificial peptide ligand MBP1, or with binding of the Cdc20 N-terminal 170-residue fragment (Cdc20N) (Fig. 9d). Mad2<sup>L13A</sup> stimulated TRIP13 more effectively, presumably because it could not stably adopt the O-Mad2 conformer and was expected to go through futile binding/unfolding cycles catalyzed by TRIP13. The ATPase activity of TRIP13 was greatly stimulated at 1:1 molar ratio of TRIP13 hexamer to p31<sup>comet</sup>-Mad2<sup>L13A</sup>, with the maximum observed at 1:2 molar ratio (Fig. 9e), suggesting that one TRIP13 hexamer likely

engages one or two p31<sup>comet</sup>-Mad2 heterodimers at a given time. Taken together, these results validate our TRIP13 ATPase assay.

We next tested our TRIP13 mutants in the ATPase assay (Fig. 10a). As reported previously for mouse TRIP13 (Ye et al., 2015), human TRIP13 W221A had much higher basal ATPase activity, nearly equal to the wild-type TRIP13 activity stimulated by p31<sup>comet</sup>-Mad2. The ATPase activity of TRIP13 W221A was not further stimulated by p31<sup>comet</sup>-Mad2. TRIP13 W221 is located in the pore loop (Fig. 10b), a structural element of AAA+ ATPases thought to be responsible for substrate translocation into the pore of the hexamer (Olivares et al., 2016). In contrast to W221A, mutation of F222, a neighboring residue in the pore loop, did change the basal ATPase activity of TRIP13, but completely abolished the stimulation by p31<sup>comet</sup>-Mad2 (Fig. 10a). Thus, the pore loop of TRIP13 serves two functions: (1) restraining the basal ATPase activity of TRIP13 and (2) coupling ATP hydrolysis to p31<sup>comet</sup>-Mad2 binding or the conformational change of Mad2. F222 is specifically involved in the second function.

The  $\alpha$ 2 helix in the large AAA+ subdomain is located on the top face of TRIP13 and is adjacent to the pore loop (Hanson and Whiteheart, 2005; Ye et al., 2015) (Fig. 10b). Mutations of K227 and K231, two residues in the  $\alpha$ 2 helix, both reduced the stimulation of TRIP13 by p31<sup>comet</sup>-Mad2, despite having opposite effects on the basal ATPase activity of TRIP13 (Fig. 10a). Intriguingly, mutation of N278, a residue in the  $\alpha$ 3 helix in the large AAA+ subdomain (Hanson and Whiteheart, 2005) (Fig. 10b), also completely abolished the stimulation of TRIP13 by p31<sup>comet</sup>-Mad2 (Fig. 10b). Finally, mutation of G320 in the hinge between the large and small AAA+ subdomains greatly reduced the ATPase activity of TRIP13 and its stimulation by p31<sup>comet</sup>-Mad2 (Fig. 10a,b). Thus, we have identified a set of residues in diverse

structural elements of TRIP13 that is critical for coupling ATP hydrolysis to substrate binding or unfolding. These mutants serve as important tools for understanding the mechanism by which TRIP13 catalyzes the conformational change of Mad2.

### **TRIP13 mutants not stimulated by p31<sup>comet</sup>-Mad2 fail to release C-Mad2 from ligands**

A major proposed function of TRIP13 is to collaborate with p31<sup>comet</sup> to disrupt Mad2–ligand complexes (Eytan et al., 2014; Wang et al., 2014b; Ye et al., 2015). Although NMR is a powerful method to assess Mad2 conformational change, it is time-consuming and requires large amounts of proteins. We thus developed a bead-based assay to monitor the disassembly of C-Mad2–ligand complexes by TRIP13 (Fig. 11a). Briefly, MBP1 or Cdc20N was covalently coupled to SulfoLink beads. Mad2 was then bound to MBP1 or Cdc20N on beads to form C-Mad2–ligand complexes. After incubation with TRIP13, p31<sup>comet</sup>, and ATP, Mad2 bound to beads was analyzed with SDS-PAGE and Coomassie staining. TRIP13 WT was capable of efficiently dissociating Mad2 from MBP1 in the presence of ATP and p31<sup>comet</sup> (Fig. 11b) and in a dose-dependent manner (Fig. 12a). The ATPase-deficient mutant TRIP13 E253A was unable to dissociate Mad2, but bound strongly to p31<sup>comet</sup>-Mad2-MBP1 in the presence of ATP. Interestingly, TRIP13 at 25 nM exhibited considerable ATPase activity (Fig. 10a), but no dissociation of Mad2 was observed at this concentration (Fig. 12a). Only at concentrations above 500 nM was TRIP13 able to efficiently dissociate Mad2. The requirement of higher concentrations of TRIP13 for Mad2 dissociation is likely due to the fact that the dissociated O-Mad2 can quickly re-bind to ligands on beads. For us to observe net

Mad2 dissociation from beads, the rate of Mad2 unfolding driven by ATP hydrolysis has to exceed that of Mad2 re-binding to ligands.

We next tested whether the TRIP13 mutations affected the ability of TRIP13 to release C-Mad2 from bound ligands. TRIP13 W221A, F222A, K227A, K231E, and N278A, which were deficient in p31<sup>comet</sup>-Mad2 stimulation, all failed to dissociate Mad2 from MBP1 (Fig. 11c) or Cdc20N (Fig. 12b). Thus, the coupling between ATP hydrolysis and p31<sup>comet</sup>-Mad2 binding or Mad2 unfolding is critical for releasing Mad2 from ligands.

### **The hinge impacts TRIP13 conformational dynamics and oligomerization**

Surprisingly, TRIP13 G320A, which at 25 nM showed little ATPase activity (Fig. 10a), was able to dissociate Mad2 from MBP1 or Cdc20 (Fig. 11c and Fig. 12b). This apparent discrepancy prompted us to perform further experiments on TRIP13 G320A. TRIP13 G320 is located at the hinge between its large and small AAA+ domains (Fig. 11d). Because the Mad2 dissociation assay was performed with 500 nM TRIP13, we tested whether TRIP13 G320A had ATPase activity at higher concentrations. Indeed, even though TRIP13 G320A at 25 nM had undetectable ATPase activity in the presence or absence of p31<sup>comet</sup>-Mad2, this mutant had substantial basal activities at 100 nM and 200 nM concentrations (Fig. 11e), which were further stimulated by p31<sup>comet</sup>-Mad2. This likely explains the ability of G320A at high concentrations to dissociate Mad2 from ligands.

One possibility for the lack of ATPase activity of G320A at low concentrations is that the mutation weakens the oligomerization of TRIP13 and prevents it from reaching/maintaining the functional hexameric state. To test this possibility, we compared the

elution profiles of TRIP13 WT and G320A in the presence of ATP on a gel filtration column. Both proteins had very similar fractionation profiles, and predominantly formed oligomers (Fig. 13). Thus, in the presence of ATP, the G320A mutation does not appear to disrupt the oligomerization of TRIP13.

We next subjected TRIP13 WT to analytical ultracentrifugation sedimentation velocity studies in the presence of 100  $\mu$ M ATP. While interpretable concentration profiles could be collected from such samples, the resulting  $c(s)$  distributions demonstrated a large degree of polydispersity in  $s_{20,w}$ -values greater than 5 S (data not shown). Thus, consistent with the broad fractionation profiles on gel filtration, ATP binding does not induce the formation of discrete TRIP13 oligomers *in vitro*, possibly due to the nucleotide-driven conformational dynamics of TRIP13. Interestingly, in the absence of ATP, TRIP13 WT at high concentrations displayed sedimentation behavior consistent with an equilibrium between discrete species (Fig. 11f). By contrast, TRIP13 G320A was monomeric under all concentrations tested. Thus, TRIP13 G320A is deficient for oligomerization in the nucleotide-free state, even though the hinge is not located in the hexamer interface.

Previous studies have shown that not all six protomers of AAA+ ATPases bind to and hydrolyze nucleotides at the same time (Olivares et al., 2016). The relative positions of the small and large AAA+ subdomains in a given protomer are very different between its nucleotide-bound and nucleotide-free states (Ye et al., 2015). Thus, the flexibility of the hinge might enable relative movements between the small and large AAA+ subdomains during the ATPase cycle. These movements not only drive substrate remodeling, but also maintain the functional hexamer state of the enzyme. We propose that the G320A mutation interferes with

conformational dynamics of TRIP13, weakens TRIP13 oligomerization in a nucleotide-state-specific manner, and reduces the ATPase activity of TRIP13. Intriguingly, sequence alignment of the hinge regions of TRIP13 and two other eukaryotic AAA+ ATPases, p97/VCP and NSF, revealed a conserved motif with the consensus of  $\phi$ GXP ( $\phi$ , a hydrophobic residue; X, any residue) (Fig. 11g). Even though the amino-acid sequence is not conserved, bacterial ClpX has a hinge of similar length. Mutations affecting the length of the hinge in ClpX uncouple the ATPase activity from substrate unfolding (Glynn et al., 2012). We speculate that hinge flexibility in AAA+ ATPases may be generally important for the conformational dynamics between the large and small AAA+ subdomains during the ATPase cycle.

### **Identification of p31<sup>comet</sup>-Mad2-binding residues on TRIP13**

The TRIP13 mutants deficient for stimulation by p31<sup>comet</sup>-Mad2 and for Mad2 release from ligands might have lost their ability to bind p31<sup>comet</sup>-Mad2 or be defective in coupling ATP hydrolysis to Mad2 unfolding. To distinguish these possibilities, we wished to directly assay the binding of p31<sup>comet</sup>-Mad2 to TRIP13. We observed that TRIP13 E253A, which was deficient in ATP hydrolysis and Mad2 dissociation, was able to bind to p31<sup>comet</sup>-Mad2-MBP1 beads in the Mad2 dissociation assay (Fig. 11b,c). We hypothesized that the ATP-bound state of TRIP13 might bind more strongly to p31<sup>comet</sup>-Mad2. Indeed, addition of ATP $\gamma$ S, a slowly hydrolyzable ATP analog, did not support Mad2 dissociation, but greatly enhanced the binding of TRIP13 WT to beads bound with p31<sup>comet</sup>-Mad2-MBP1 (Fig. 14a). Addition of ADP did not enhance TRIP13 WT binding to p31<sup>comet</sup>-Mad2-MBP1, and reduced the binding of TRIP13 E253A, presumably because ADP displaced some ATP bound to this mutant. These

results show that p31<sup>comet</sup>-Mad2 prefers to bind to the ATP-bound state of TRIP13. The use of ATP $\gamma$ S in place of ATP converts the Mad2 dissociation assay into an assay that can monitor the binding between TRIP13 and p31<sup>comet</sup>-Mad2.

We next tested the binding of the TRIP13 mutants to p31<sup>comet</sup>-Mad2 with this assay. TRIP13 W221A, F222A, K227A, and K231E were deficient in binding to p31<sup>comet</sup>-Mad2-MBP1 (Fig. 15a) or p31<sup>comet</sup>-Mad2-Cdc20N (Fig. 14b), suggesting that these residues at the pore loop and the  $\alpha$ 2 helix mediate binding of p31<sup>comet</sup>-Mad2 to TRIP13 (Fig. 15b). Therefore, p31<sup>comet</sup>-Mad2 likely binds to the top face of TRIP13 through charged interactions with the  $\alpha$ 2 helix and through interactions with the pore loop.

TRIP13 G320A expectedly retained binding to p31<sup>comet</sup>-Mad2 (Fig. 14b and Fig. 15a), as it was capable of dissociating Mad2 from ligands in the presence of ATP. The weakened binding of TRIP13 G320A to p31<sup>comet</sup>-Mad2 is likely an indirect consequence of altered conformational dynamics of the mutant.

Surprisingly, the TRIP13 N278A mutant, which was deficient in promoting Mad2 dissociation from ligands and whose ATPase activity was not stimulated by p31<sup>comet</sup>-Mad2, retained substantial binding to p31<sup>comet</sup>-Mad2. Thus, the N278 mutation uncouples p31<sup>comet</sup>-Mad2 binding from ATP hydrolysis and subsequent conformational change of Mad2. N278 is therefore critical for harnessing the energy of ATP hydrolysis to switch the conformation of Mad2. TRIP13 N278 is located at the interface between adjacent TRIP13 protomers. Interestingly, it is in close proximity to the pore loop at four such interfaces between one nucleotide-bound protomer and one nucleotide-free protomer (I and II), but is far away from the pore loop at the other two interfaces between two nucleotide-free protomers (III) (Fig. 15c).

We speculate that N278 engages with the pore loop in specific nucleotide states of TRIP13 when it is bound to p31<sup>comet</sup>-Mad2, and facilitates the dynamic movements of the pore loop during ATP hydrolysis. Mutation of N278 might hinder the ability of the pore loop to change conformation, decrease ATP hydrolysis in the substrate-bound state, and inhibit the ability of TRIP13 to dissociate Mad2 from ligands.

### **Reconstitution of TRIP13-dependent MCC inactivation *in vitro***

We have demonstrated so far that, aided by p31<sup>comet</sup>, TRIP13 catalyzes the conversion of C-Mad2 to O-Mad2 and disassembles C-Mad2-peptide complexes *in vitro*. MCC disassembly has been proposed to be the key function of TRIP13 in checkpoint silencing (Eytan et al., 2014; Miniowitz-Shemtov et al., 2015; Wang et al., 2014b). We tested whether TRIP13, with the help of p31<sup>comet</sup>, could inactivate MCC *in vitro*. As shown previously (Ji et al., 2017; Jia et al., 2016; Lara-Gonzalez et al., 2011), incubation of recombinant BubR1N (residues 1-370), dimeric Mad2 WT, and full-length Cdc20 produced a minimal, functional MCC, which inhibited the ubiquitination of securin by APC/C<sup>Cdc20</sup> (Fig. 16a,b). Addition of TRIP13, p31<sup>comet</sup>, and ATP to the mixture of MCC components (prior to the addition of APC/C<sup>Cdc20</sup>) completely restored the ubiquitination activity of APC/C<sup>Cdc20</sup> (Fig. 16b), indicating that TRIP13 was able to inactivate MCC. As expected, TRIP13-dependent MCC inactivation required p31<sup>comet</sup> and ATP. The ATPase-deficient TRIP13 E253A was unable to restore APC/C<sup>Cdc20</sup> ubiquitination activity. The TRIP13 mutants defective for Mad2 dissociation from peptide ligands, W221A, F222A, K227A, K231E, and N278A, were also unable to inactivate MCC. TRIP13 G320A, which was capable of releasing Mad2 from ligands, was able to

inactivate MCC to allow APC/C<sup>Cdc20</sup>-mediated ubiquitination of securin. The perfect correlation between the abilities of TRIP13 mutants to release Mad2 from ligands and to inactivate MCC strongly suggest that TRIP13 inactivates MCC through promoting the C-Mad2 to O-Mad2 conversion and disrupting the C-Mad2–Cdc20 interaction.

We next tested whether TRIP13–p31<sup>comet</sup> could inactivate MCC that was already bound to APC/C<sup>Cdc20</sup>. We pre-incubated the MCC components with APC/C<sup>Cdc20</sup> and then added TRIP13, p31<sup>comet</sup>, and ATP, before performing the ubiquitination assay. TRIP13–p31<sup>comet</sup> was unable to relieve the inhibition of APC/C<sup>Cdc20</sup> by the pre-bound MCC (Fig. 16c). Therefore, our results indicate that TRIP13 can catalyze the disassembly of free MCC, but cannot effectively inactivate MCC already bound to APC/C<sup>Cdc20</sup>.

### **The N-terminus of Mad2 is necessary for TRIP13 inactivation of MCC.**

Another report about the mechanism of TRIP13 unfolding of Mad2 has recently been published (Ye et al., 2017). Based on indirect crosslinking results, Ye, et al. (2017) suggest that TRIP13 binds and unfolds the N-terminus of Mad2. As we have shown, the structural transition of C-Mad2 to O-Mad2 by TRIP13 is directed by a conformational change in the C-terminus of the protein. Our NMR data reveals that TRIP13 performs only local unfolding of Mad2, and does not completely unfold the protein (Fig. 7), and thus unfolding the N-terminus would not logically lead to the conformational change in the C-terminus of Mad2. As such, we decided to perform further experiments to test the results reported by Ye, et al. (2017).

We first tested the report that TRIP13 binds the N-terminus of Mad2. We purified  $\Delta$ N10-Mad2, which we have previously characterized (Hara et al., 2015; Yang et al., 2008),

and performed the Mad2 binding assay. We confirmed that  $\Delta$ N10-Mad2 retains binding to p31<sup>comet</sup>, but it is unable to bind to TRIP13 (Figure 17a). This confirms the previous report that the N-terminus of Mad2 is required for engagement of TRIP13 (Ye et al., 2017). We also tested  $\Delta$ N10-Mad2 in the APC/C ubiquitination assay.  $\Delta$ N10-Mad2 was able to be incorporated into the MCC and inhibit APC/C ubiquitination, but TRIP13 was unable to inactivate MCC containing  $\Delta$ N10-Mad2 (Figure 17b). This confirms that the N-terminus of Mad2 is dispensable for its incorporation into the MCC and MCC inhibition of APC/C, but that the N-terminus is necessary for checkpoint silencing by TRIP13.

Ye, et al. (2017) postulates that in addition to binding to the N-terminus of Mad2, TRIP13 unfolds the N-terminus by engagement at the pore loop of TRIP13. To demonstrate this, they mutated the W221 residue of the pore loop to cysteine and performed crosslinking experiments to Mad2. This crosslinking appeared to show that the N-terminus of Mad2 binds to TRIP13 at the pore loop (Ye et al., 2017). We have shown that mutation of the W221 residue to alanine abrogates binding of TRIP13 to Mad2 (Fig. 15), and thus we questioned the validity of the crosslinking data. We mutated W221 to cysteine and repeated the binding experiment, along with our ATPase assay and Mad2 dissociation assay. We show that TRIP13 W221C cannot bind to Mad2, and that it phenocopies TRIP13 W221A (Figure 18). Thus, the crosslinking of the pore loop to Mad2 may have been an artifact of the crosslinking conditions, and it is unclear whether or not the N-terminus of Mad2 engages the pore loop of TRIP13.

## DISCUSSION

TRIP13 has recently been discovered as the specific ATPase that provides energy for the conformational change of C-Mad2 to O-Mad2, and has been suggested to promote spindle checkpoint silencing through MCC disassembly (Eytan et al., 2014; Wang et al., 2014b; Ye et al., 2015). The structure of the *C. elegans* homolog of TRIP13, PCH-2, has been determined, and reveals an asymmetric hexameric architecture typical of AAA+ ATPases (Olivares et al., 2016; Ye et al., 2015). In this study, using NMR spectroscopy, we have definitively shown that, with p31<sup>comet</sup> as the adaptor, TRIP13 catalyzes the conversion of C-Mad2 to O-Mad2. H/D exchange experiments indicate that TRIP13–p31<sup>comet</sup>-mediated structural transition of Mad2 does not involve the global unfolding of Mad2. We have determined the crystal structure of human TRIP13 monomer in the ADP-bound state, revealing conserved features of TRIP13 and important differences in the N-terminal domain. Systematic mutagenesis studies have identified functional residues of TRIP13 in multiple structure elements that mediate p31<sup>comet</sup>–Mad2 binding, ATP hydrolysis, or Mad2 unfolding. Through *in vitro* reconstitution, we show that TRIP13–p31<sup>comet</sup> inactivates the ability of free MCC to inhibit APC/C<sup>Cdc20</sup>, but does not inactivate MCC already bound to APC/C<sup>Cdc20</sup>. Finally, we have confirmed that the N-terminus of Mad2 is necessary for MCC inactivation by TRIP13. Our results provide key insight into the mechanisms by which TRIP13 catalyzes the C-Mad2–O-Mad2 conversion and promotes spindle checkpoint silencing.

### **Mechanism of TRIP13-catalyzed Mad2 structural transition**

The asymmetric hexameric ring structure of TRIP13 is reminiscent of that of the bacterial unfoldase ClpX (Glynn et al., 2009; Olivares et al., 2016; Ye et al., 2015). ClpX binds to substrates with its convex, top surface, and is believed to completely unfold substrates and thread them through an inner pore that is lined by the pore loop conserved in AAA+ ATPases (Olivares et al., 2016). The unfolded substrates that emerge from the pore are then degraded by the ClpP protease, which is bound to the concave, bottom surface of ClpX (Olivares et al., 2016). We have found that, similar to ClpX, TRIP13 binds to p31<sup>comet</sup>-Mad2 on its convex, top surface through charged interactions with the  $\alpha$ 2 helix in the large AAA+ subdomain and through engaging the conserved pore loop. Because blocking ATP hydrolysis by mutations or ATP $\gamma$ S enhances p31<sup>comet</sup>-Mad2 binding to TRIP13, p31<sup>comet</sup>-Mad2 likely binds to the ATP-bound protomers of TRIP13.

Unlike ClpX, however, TRIP13-catalyzed conformational change does not involve the complete, global unfolding of Mad2, as slowly exchanging amide protons are protected from D<sub>2</sub>O during the entire process. We propose that the p31<sup>comet</sup>-Mad2-MIM complex docks on TRIP13 protomers in the ATP-bound state and at a site involving the  $\alpha$ 2 helix (Fig. 19a). This binding is dependent on the N-terminus of Mad2. Mad2 then engages the pore loop of TRIP13 and relieves the autoinhibition of the ATPase activity. At present, it is unclear if the N-terminus or C-terminus of Mad2 binds to the pore loop, but we speculate here that it is the C-terminus since it is the C-terminus of Mad2 that undergoes conformational change in the structures of C-Mad2 versus O-Mad2 (Figure 5a). After the engagement of Mad2 at the pore loop of TRIP13, ATP hydrolysis drives conformational changes in TRIP13 and the

translocation of the Mad2 C-terminus, which is anchored by the pore loop with the support of other structural elements, such as N278 in  $\alpha 3$ . The local unfolding of the C-terminal safety belt of Mad2 releases the bound MIM and disrupts the p31<sup>comet</sup>-Mad2 interaction. As TRIP13 does not bind strongly to either Mad2 or p31<sup>comet</sup>, the breakup of the p31<sup>comet</sup>-Mad2 complex causes both proteins to be released from TRIP13. TRIP13 can then bind another p31<sup>comet</sup>-Mad2-MIM complex to repeat the process.

At present, we do not know whether the local unfolding of Mad2 C-terminal region involves the threading of this region through the central pore of the TRIP13 hexamer. If it does, mechanisms must exist to release the partially unfolded Mad2 from TRIP13 so that the stable core of Mad2 is not threaded through the pore and unfolded. Alternatively, ATP-driven translocation events of the Mad2 C-terminus may suffice to unravel the C-terminal safety belt of Mad2 and occur solely on the top face of TRIP13.

### **Mechanistic insight into MCC inactivation by TRIP13**

Our reconstitution of TRIP13-p31<sup>comet</sup>-dependent MCC inactivation *in vitro* has provided insight into the mechanism by which TRIP13 promotes spindle checkpoint silencing. Perhaps our most important finding is that TRIP13-p31<sup>comet</sup> only inactivates free MCC prior to its binding to APC/C<sup>Cdc20</sup>, but not MCC already bound to APC/C<sup>Cdc20</sup>. We propose that TRIP13-p31<sup>comet</sup> disassembles free MCC in a stepwise fashion (Fig. 19b). Because p31<sup>comet</sup> and BubR1 bind to overlapping interfaces on C-Mad2 and compete for C-Mad2 binding (Alfieri et al., 2016; Chao et al., 2012; Yang et al., 2007), p31<sup>comet</sup> binding to C-Mad2 disrupts the integrity of MCC and releases BubR1. The p31<sup>comet</sup>-C-Mad2-Cdc20 complex is then recognized by

TRIP13. TRIP13-catalyzed conversion of C-Mad2 to O-Mad2 dissociates Mad2 from Cdc20, causing the complete disassembly of MCC. In this way, TRIP13–p31<sup>comet</sup> reduces the cellular concentration of free MCC and helps to turn off the spindle checkpoint.

Our results suggest that additional mechanisms are required to inactivate MCC bound to APC/C and promote checkpoint silencing. One such mechanism is APC/C<sup>Cdc20</sup>-dependent ubiquitination of the Cdc20 molecule that is part of the MCC (Foster and Morgan, 2012; Uzunova et al., 2012). Cdc20 ubiquitination is likely sufficient to release MCC from APC/C, which can then be acted on by TRIP13–p31<sup>comet</sup> (Fig. 19b). Alternatively, degradation of ubiquitinated Cdc20 by the proteasome can cause the complete disassembly of MCC.

In addition to promoting MCC disassembly, we have shown that TRIP13–p31<sup>comet</sup> can catalyze the conversion of unliganded C-Mad2 to O-Mad2. Because C-Mad2 is the low-energy, thermodynamically more stable state of Mad2, O-Mad2 can spontaneously convert to C-Mad2 (Luo et al., 2004). TRIP13–p31<sup>comet</sup> is needed to revert the spontaneously converted C-Mad2 back to O-Mad2. Mad2 released by Cdc20 degradation that is still in the C-Mad2 conformer may also be converted to O-Mad2 by TRIP13–p31<sup>comet</sup> (Fig. 19b). TRIP13–p31<sup>comet</sup> may therefore be required to maintain the pool of O-Mad2 in the cell by converting free, unliganded C-Mad2 back to the O-Mad2. Failure to do so causes premature accumulation of C-Mad2 and spindle checkpoint defects (Ma and Poon, 2016), as O-Mad2 is the Mad2 conformer that is activated by Mad1–Mad2 at kinetochores to become I-Mad2, which is subsequently incorporated into MCC.

In conclusion, using a combination of biophysical and biochemical approaches, we have demonstrated that TRIP13–p31<sup>comet</sup> catalyzes the conversion of C-Mad2 to O-Mad2

without the global unfolding of Mad2. We have defined the functional roles of multiple structural elements of TRIP13 in coupling ATP hydrolysis to Mad2 unfolding. Finally, we have reconstituted TRIP13–p31<sup>comet</sup>-dependent MCC inactivation *in vitro*, leading to new testable models of how TRIP13 and p31<sup>comet</sup> promote spindle checkpoint silencing and the metaphase–anaphase transition.

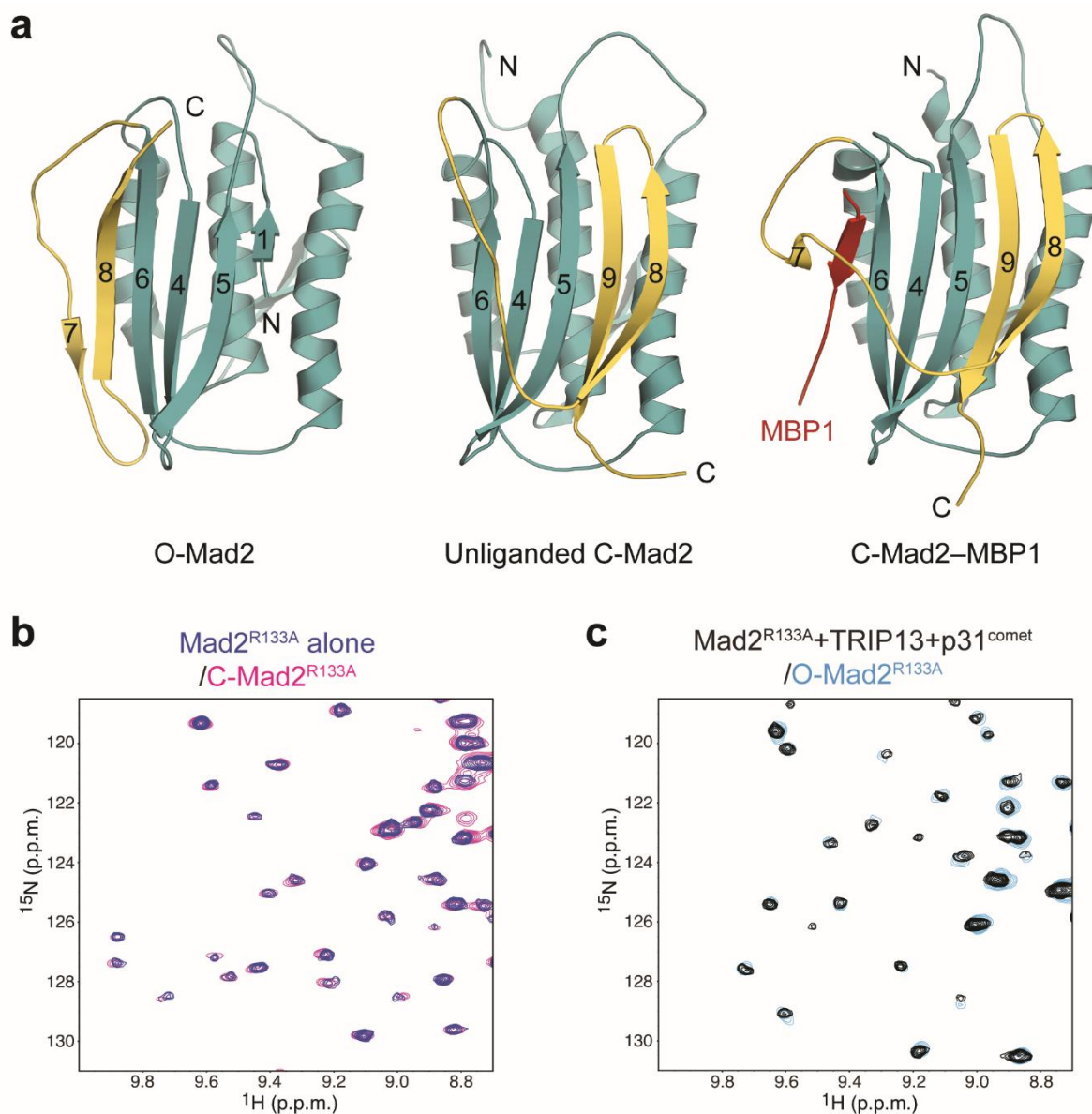


**Figure 5: TRIP13 catalyzes C-Mad2 to O-Mad2 conversion in the presence of p31<sup>comet</sup>.** (a) Ribbon diagrams of O-Mad2 (left), unliganded C-Mad2 (middle), and C-Mad2 bound to its high-affinity artificial ligand MBP1 (right). The C-terminal region that undergoes a large conformational change and forms the safety belt structure in C-Mad2 is colored yellow while the rest of the protein is in cyan. Strands in the major  $\beta$  sheet are labeled with their numbers. The N- and C-termini are indicated. All protein structure figures in this study were generated with PyMOL (Schrödinger, LLC; <http://www.pymol.org>). (b) Overlay of regions of the  $^1\text{H}$ - $^{15}\text{N}$  HSQC spectra of C-Mad2<sup>R133A</sup> (in magenta) and  $^{15}\text{N}$ -Mad2<sup>R133A</sup> before the addition of TRIP13 and  $\Delta\text{N}35$ -p31<sup>comet</sup> (in blue). (c) Overlay of regions of the  $^1\text{H}$ - $^{15}\text{N}$  HSQC spectra of O-Mad2<sup>R133A</sup> (in cyan) and  $^{15}\text{N}$ -Mad2<sup>R133A</sup> after the addition of ATP and sub-stoichiometric amounts of TRIP13 and  $\Delta\text{N}35$ -p31<sup>comet</sup> (in black).

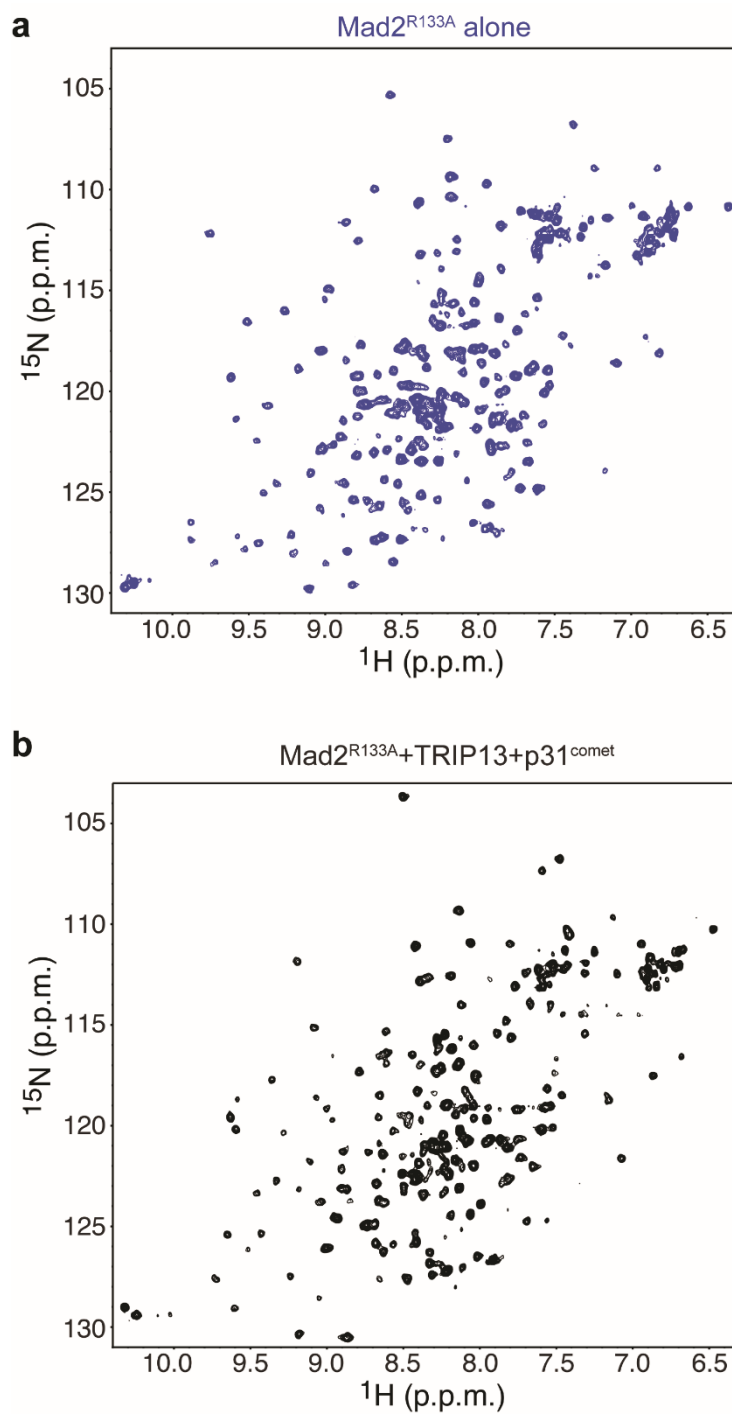


**Figure 6: TRIP13 catalyzes the conversion of C-Mad2 to O-Mad2 with the help of p31<sup>comet</sup>.** (a) The <sup>1</sup>H-<sup>15</sup>N HSQC spectrum of <sup>15</sup>N-Mad2<sup>R133A</sup> before the addition of TRIP13 and ΔN35-p31<sup>comet</sup>. (b) The <sup>1</sup>H-<sup>15</sup>N HSQC spectrum of <sup>15</sup>N-Mad2<sup>R133A</sup> after the addition of ATP and sub-stoichiometric amounts of TRIP13 and ΔN35-p31<sup>comet</sup>.

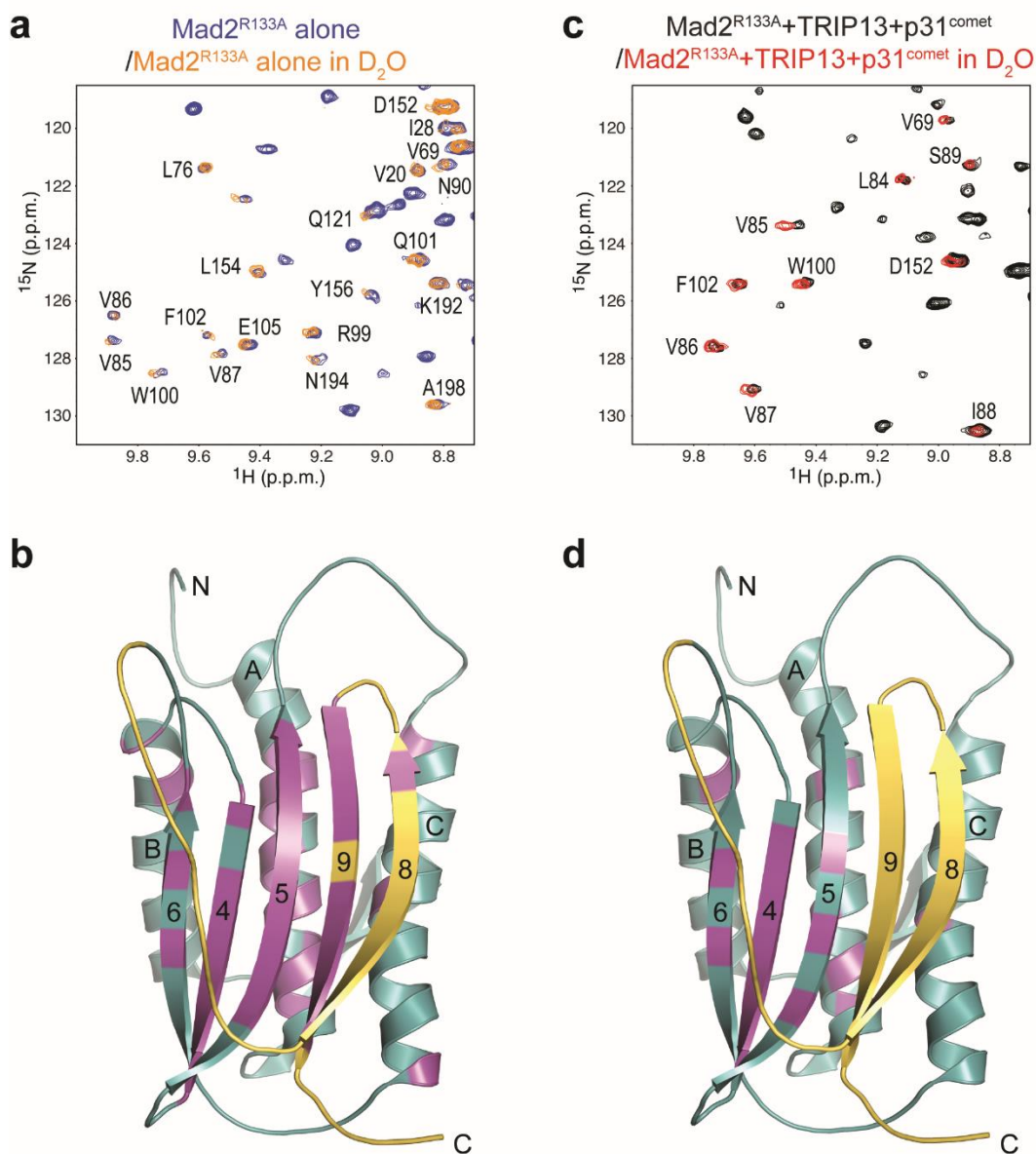


**Figure 7: TRIP13-catalyzed structural transition of Mad2 does not involve Mad2 global unfolding.** (a) Overlay of regions of the  $^1\text{H}$ - $^{15}\text{N}$  HSQC spectra of  $^{15}\text{N}$ -labeled C-Mad2<sup>R133A</sup> in H<sub>2</sub>O (blue) and C-Mad2<sup>R133A</sup> in D<sub>2</sub>O (orange). Residues with slow-exchanging amides are labeled. (b) Ribbon diagrams of unliganded C-Mad2, with slow-exchanging residues in the absence of TRIP13 colored magenta. Strands in the major  $\beta$  sheet are labeled with their numbers. The N- and C-termini are indicated. (c) Overlay of regions of the  $^1\text{H}$ - $^{15}\text{N}$  HSQC spectra of  $^{15}\text{N}$ -labeled Mad2<sup>R133A</sup> in H<sub>2</sub>O (black) and D<sub>2</sub>O (red) after the addition of ATP and sub-stoichiometric amounts of TRIP13 and  $\Delta\text{N35-p31}^{\text{comet}}$ . Residues with slow-exchanging amides are labeled. (d) Ribbon diagrams of unliganded C-Mad2, with slow-exchanging residues in the presence of TRIP13 colored magenta.

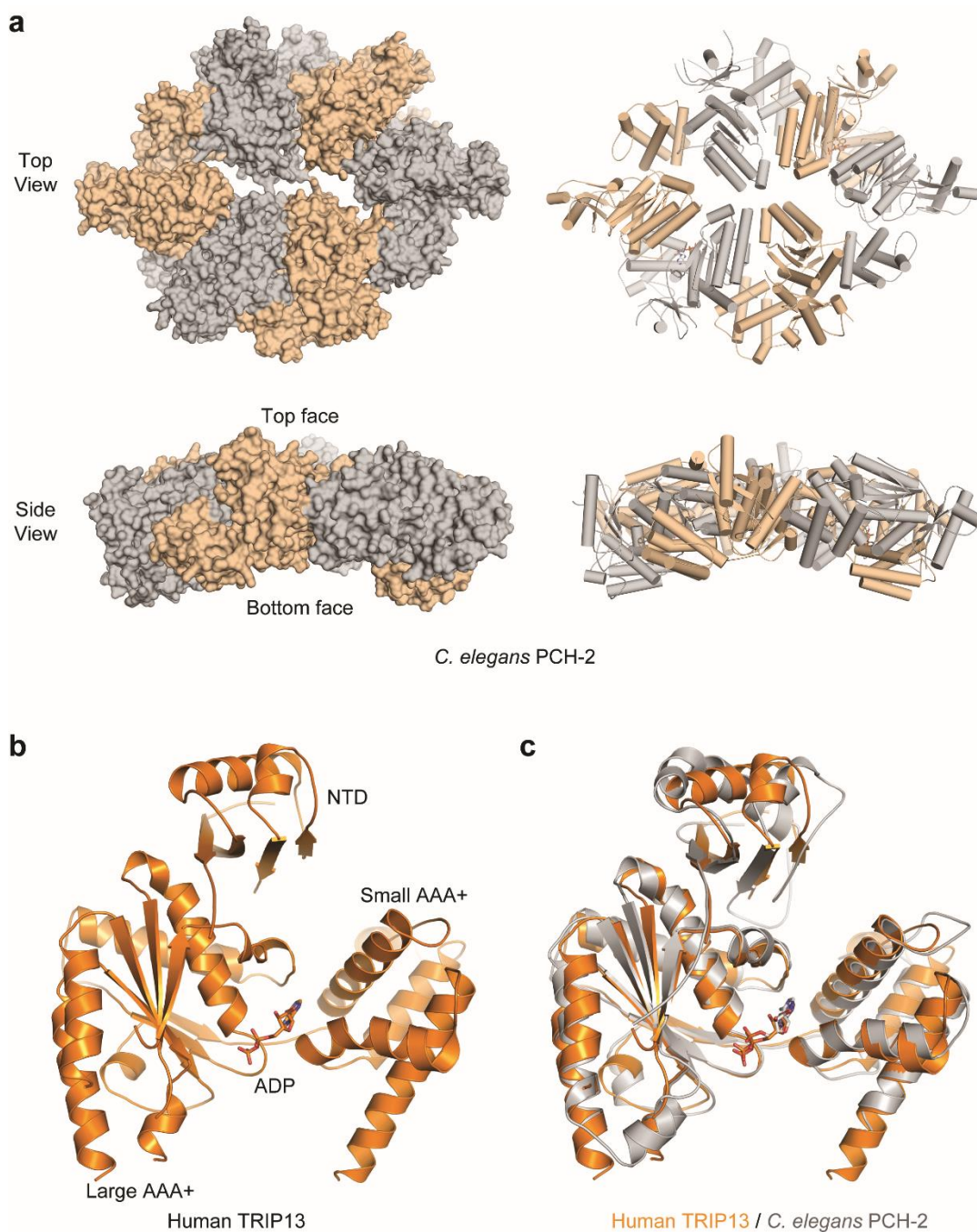


**Figure 8: Crystal structure of human TRIP13 in its monomeric ADP-bound state.** (a) Surface and ribbon diagrams of *C. elegans* PCH-2 (PDB ID: 4XGU) in top and side views. Neighboring protomers are shown in different colors. (b) Ribbon diagram of the crystal structure of human TRIP13, with the bound ADP shown in sticks. (c) Overlay of the ribbon diagrams of the structures of human TRIP13 (orange) and the ADP-bound protomer of *C. elegans* PCH-2 (gray), with the bound ADP molecules shown in sticks.

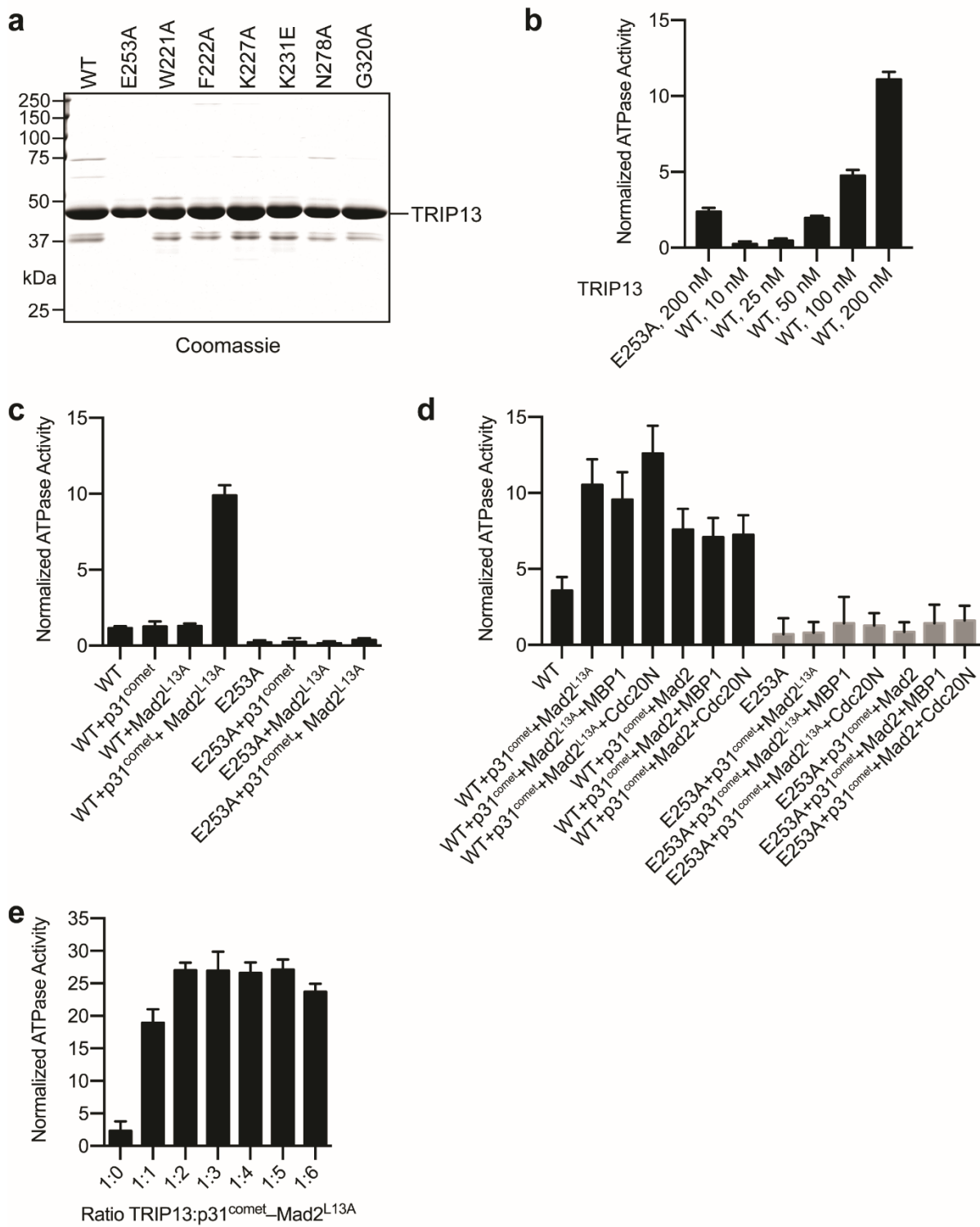


**Figure 9: Development of a high-throughput assay to assess the ATPase activity of TRIP13 mutants.** (a) Coomassie-stained SDS-PAGE gel of recombinant purified TRIP13 wild type (WT) and the indicated mutants. (b) Normalized ATPase activities of TRIP13 WT and TRIP13 E253A at the indicated concentrations. Mean  $\pm$  SD;  $n = 3$ . (c) Stimulation of the ATPase activity of TRIP13 (25 nM) by  $\Delta$ N35-p31<sup>comet</sup> (50 nM), Mad2<sup>L13A</sup> (50 nM), or the  $\Delta$ N35-p31<sup>comet</sup>-Mad2<sup>L13A</sup> complex (50 nM). Mean  $\pm$  SD;  $n = 10$ . (d) Stimulation of the ATPase activity of TRIP13 (25 nM) by  $\Delta$ N35-p31<sup>comet</sup> (125 nM) and different forms of C-Mad2, including Mad2<sup>L13A</sup> (125 nM), dimeric Mad2 (125 nM), Mad2-MBP1 (125 nM), or Mad2-Cdc20N (125 nM). Mean  $\pm$  SD;  $n = 10$ . (e) Stimulation of the ATPase activity of TRIP13 (25 nM) by  $\Delta$ N35-p31<sup>comet</sup>-Mad2<sup>L13A</sup> at the indicated molar ratios. Mean  $\pm$  SD;  $n = 4$ .

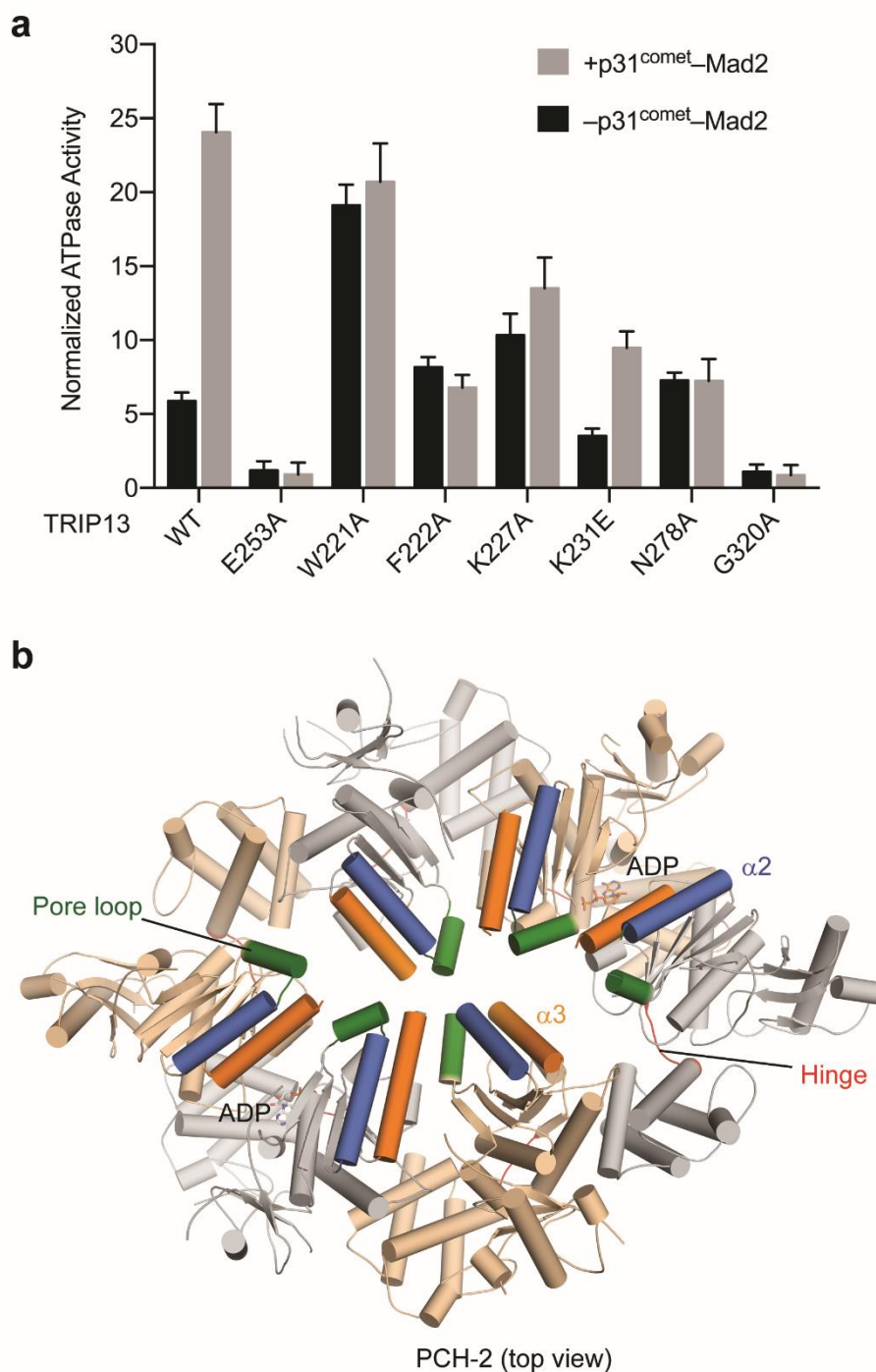


**Figure 10: Identification of TRIP13 mutants with defective p31<sup>comet</sup>-Mad2 stimulation.** (a) Normalized ATPase activities of the indicated TRIP13 proteins at 25 nM with (+) or without (-) 50 nM  $\Delta$ N35-p31<sup>comet</sup>-Mad2<sup>L13A</sup>. Mean  $\pm$  SD;  $n = 9$  independent experiments. (b) Cartoon diagram of *C. elegans* PCH-2 in the top view. The pore loop, the  $\alpha 2$  helix, the  $\alpha 3$  helix, and the hinge are shown in green, blue, orange, and red, respectively. The bound ADP molecules are shown in sticks.

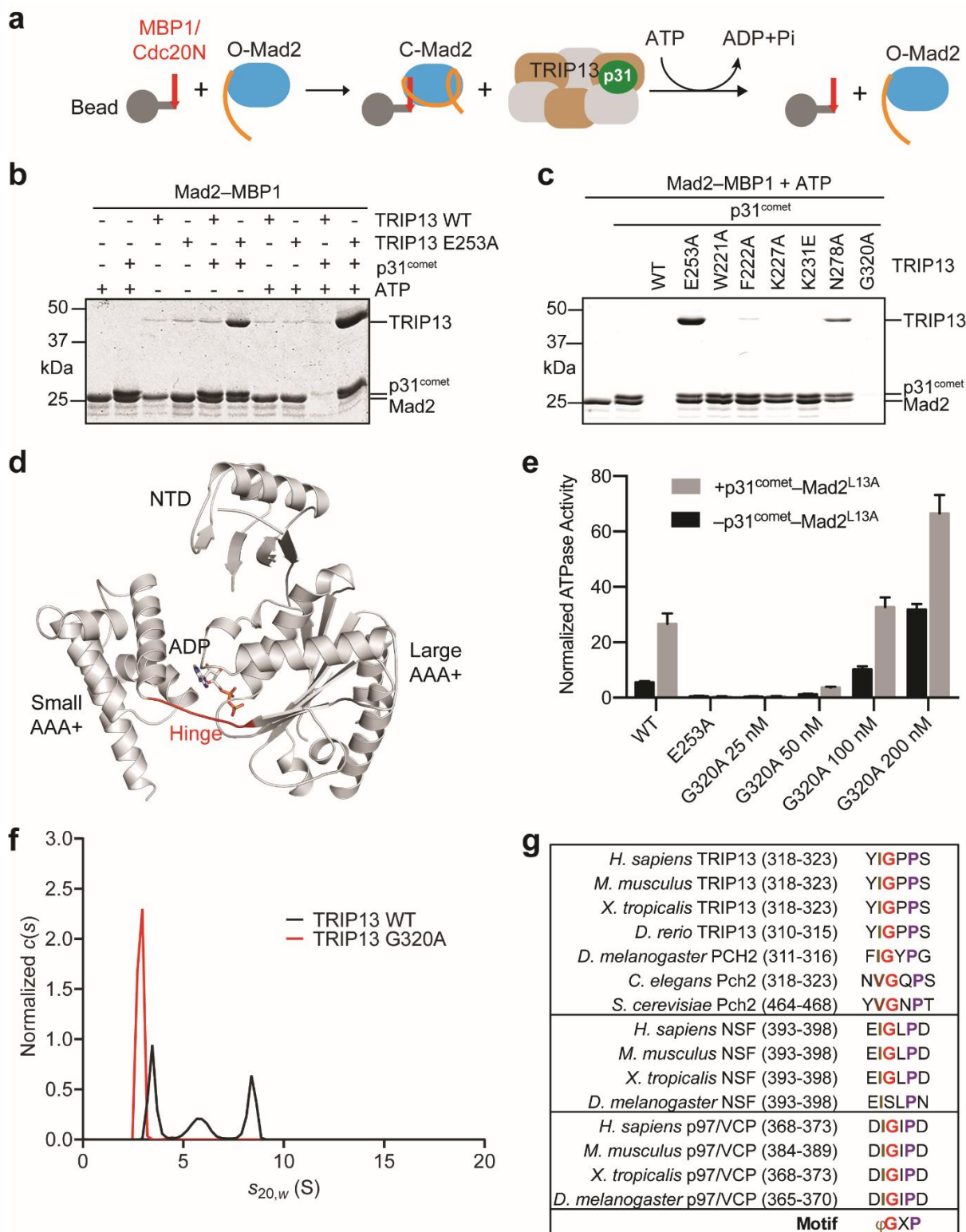


**Figure 11: The TRIP13 hinge is required for conformational dynamics and oligomerization.** (a) Schematic drawing of the Mad2 dissociation assay. (b) MBP1-coupled beads were first incubated with Mad2 and then incubated with or without TRIP13 wild type (WT) or E253A (1  $\mu$ M),  $\Delta$ N35-p31<sup>comet</sup> (2  $\mu$ M), or ATP (1 mM). Proteins bound to beads were analyzed by SDS-PAGE and stained with Coomassie blue. (c) MBP1-coupled beads were first incubated with Mad2 and then incubated with TRIP13 wild type (WT) and the indicated mutants (500 nM) in the presence of  $\Delta$ N35-p31<sup>comet</sup> (1  $\mu$ M) and ATP (1 mM). Proteins bound to beads were analyzed by SDS-PAGE and stained with Coomassie blue. (d) Ribbon diagram of human TRIP13, with the hinge connecting the large and small AAA+ subdomains colored red. ADP is shown in sticks. (e) Normalized ATPase activities of TRIP13 WT at 25 nM and G320A at the indicated concentrations with (+) or without (-)  $\Delta$ N35-p31<sup>comet</sup>-Mad2<sup>L13A</sup>. The concentrations of p31<sup>comet</sup>-Mad2 were kept at 2:1 molar ratio of those of TRIP13. Mean  $\pm$  SD;  $n = 8$  independent experiments. (f) Sedimentation velocity analysis of TRIP13 WT and G320A in the absence of ATP. (g) Sequence alignment of the hinge region of TRIP13, the D1 domain NSF, and the D1 domain p97/VCP from different organisms.



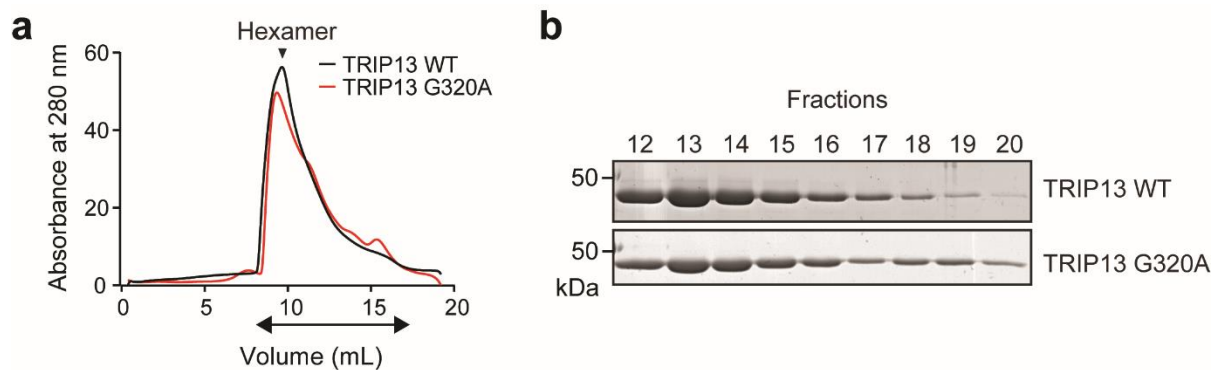


**Figure 13: TRIP13 G320A forms oligomers in the presence of ATP. (a)** UV traces of TRIP13 wild type (WT) and G320A fractionated on a gel filtration column. **(b)** Protein-containing fractions in **a** were analyzed by SDS-PAGE and stained with Coomassie.

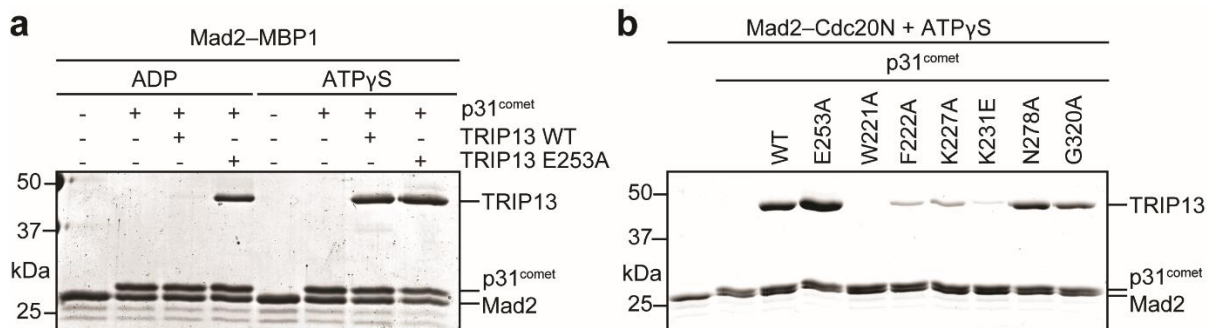


**Figure 14: The p31<sup>comet</sup>-Mad2 complex prefers to bind to TRIP13 in the ATP-bound state.** (a) MBP1-coupled beads were first incubated with Mad2 and then incubated with 500 nM TRIP13 wild type (WT) or E253A and 1  $\mu$ M  $\Delta$ N35-p31<sup>comet</sup> in the presence of 1 mM ADP or ATP $\gamma$ S. Proteins bound to beads were analyzed by SDS-PAGE and stained with Coomassie blue. (b) Cdc20N-coupled beads were first incubated with Mad2, and then incubated with TRIP13 wild type (WT) or the indicated mutants (500 nM),  $\Delta$ N35-p31<sup>comet</sup> (1  $\mu$ M), and ATP $\gamma$ S (1 mM). Proteins bound to beads were analyzed by SDS-PAGE and stained with Coomassie blue.

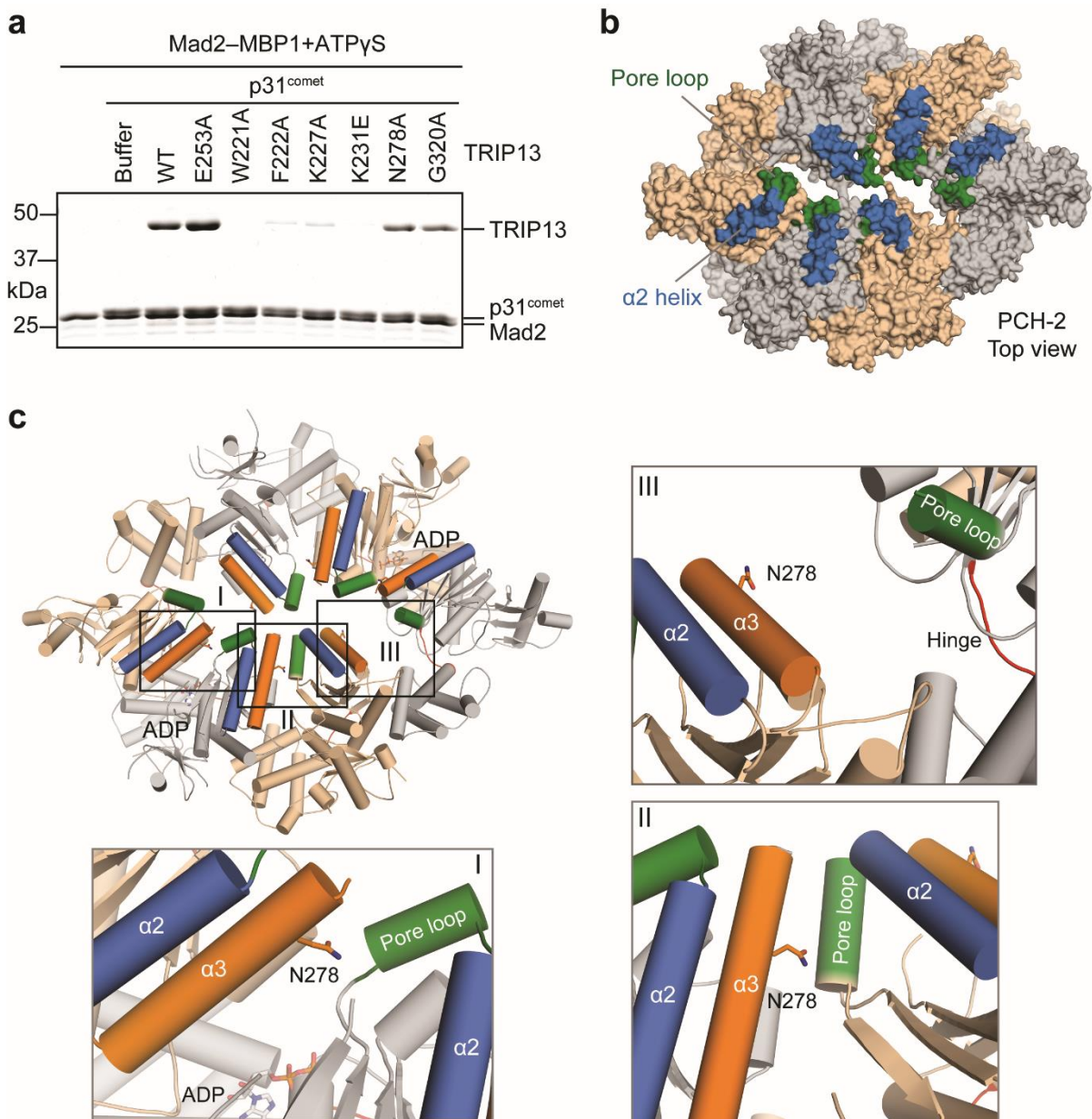


**Figure 15: Identification of a p31<sup>comet</sup>-Mad2-binding site on TRIP13.** (a) MBP1-coupled beads were first incubated with Mad2, and then incubated with TRIP13 wild type (WT) or the indicated mutants (500 nM),  $\Delta$ N35-p31<sup>comet</sup> (1  $\mu$ M), and ATP $\gamma$ S (1 mM). Proteins bound to beads were analyzed by SDS-PAGE and stained with Coomassie blue. (b) Surface diagram of *C. elegans* PCH-2 in the top view, with the pore loop and  $\alpha$ 2 helix colored green and blue, respectively. (c) Cartoon diagram of *C. elegans* PCH-2, with zoomed-in views of the boxed interfaces (I-III) shown. N278 and ADP are shown in sticks. The pore loop, the  $\alpha$ 2 helix, and the  $\alpha$ 3 helix are colored green, blue, and orange, respectively. Each of the three types of interfaces is present twice in the PCH-2 hexamer.



**Figure 16: TRIP13 prevents APC/C<sup>Cdc20</sup> inhibition by MCC components.** (a) Schematic diagram of the APC/C ubiquitination assay in the absence or presence of MCC components, TRIP13, or p31<sup>comet</sup>. (b) Ubiquitination of securin-Myc by APC/C<sup>Cdc20</sup> in the presence of MCC components (780 nM BubR1N, 1  $\mu$ M Mad2, and 600 nM Cdc20), TRIP13 wild type (WT) or the indicated mutants (50 nM), and  $\Delta$ N35-p31<sup>comet</sup> (1  $\mu$ M). MCC components were pre-incubated with TRIP13, p31<sup>comet</sup>, and ATP (1 mM). The protein mixture was then added to APC/C<sup>Cdc20</sup>. The ubiquitination reaction mixtures were blotted with the anti-Myc antibody. (c) Ubiquitination of securin-Myc by APC/C<sup>Cdc20</sup> that was first incubated with MCC components (780 nM BubR1N, 1  $\mu$ M Mad2, and 600 nM Cdc20) for 20 minutes and then incubated with TRIP13 WT (50 nM) and  $\Delta$ N35-p31<sup>comet</sup> (1  $\mu$ M). The ubiquitination reaction mixtures were blotted with the anti-Myc antibody.

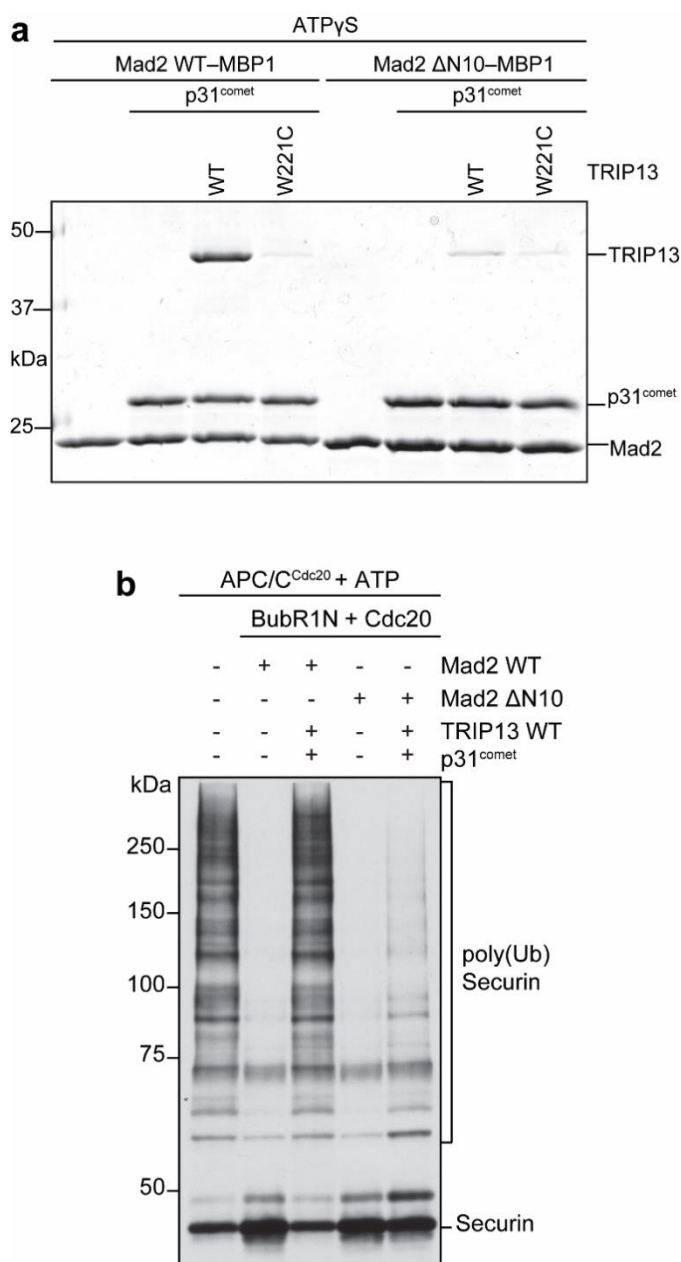


**Figure 17: The N-terminus of Mad2 is required for binding TRIP13 and for inactivation of MCC by TRIP13.** (a) MBP1-coupled beads were first incubated with Mad2 or ΔN10-Mad2, and then incubated with TRIP13 wild type (WT) (500 nM), ΔN35-p31<sup>comet</sup> (1 μM), and ATPγS (1 mM). Proteins bound to beads were analyzed by SDS-PAGE and stained with Coomassie blue. (b) Ubiquitination of securin-Myc by APC/C<sup>Cdc20</sup> in the presence of MCC components (780 nM BubR1N, 1 μM Mad2 or ΔN10-Mad2, and 600 nM Cdc20), TRIP13 wild type (WT) (50 nM), and ΔN35-p31<sup>comet</sup> (1 μM). MCC components were pre-incubated with TRIP13, p31<sup>comet</sup>, and ATP (1 mM). The protein mixture was then added to APC/C<sup>Cdc20</sup>. The ubiquitination reaction mixtures were blotted with the anti-Myc antibody.

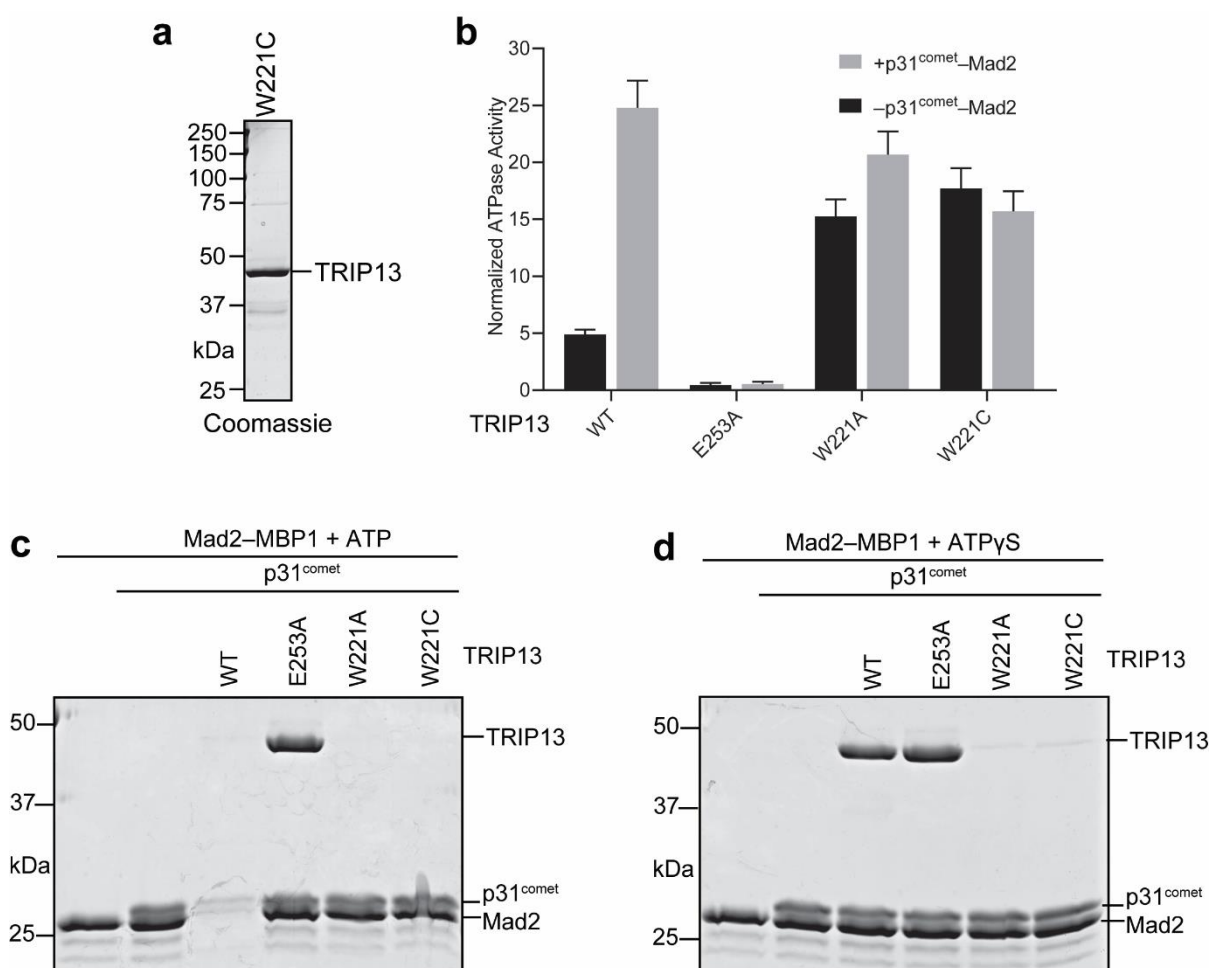


**Figure 18: TRIP13 W221C phenocopies TRIP13 W221A, and it cannot bind to p31<sup>comet</sup>-Mad2.** (a) Coomassie-stained SDS-PAGE gel of recombinant purified TRIP13 W221C. (b) Normalized ATPase activities of the indicated TRIP13 proteins at 25 nM with (+) or without (-) 50 nM  $\Delta$ N35-p31<sup>comet</sup>-Mad2<sup>L13A</sup>. Mean  $\pm$  SD;  $n = 9$  independent experiments. (c) MBP1-coupled beads were first incubated with Mad2 and then incubated with TRIP13 wild type (WT) and the indicated mutants (500 nM) in the presence of  $\Delta$ N35-p31<sup>comet</sup> (1  $\mu$ M) and ATP (1 mM). Proteins bound to beads were analyzed by SDS-PAGE and stained with Coomassie blue. (d) MBP1-coupled beads were first incubated with Mad2, and then incubated with TRIP13 wild type (WT) or the indicated mutants (500 nM),  $\Delta$ N35-p31<sup>comet</sup> (1  $\mu$ M), and ATP $\gamma$ S (1 mM). Proteins bound to beads were analyzed by SDS-PAGE and stained with Coomassie blue.

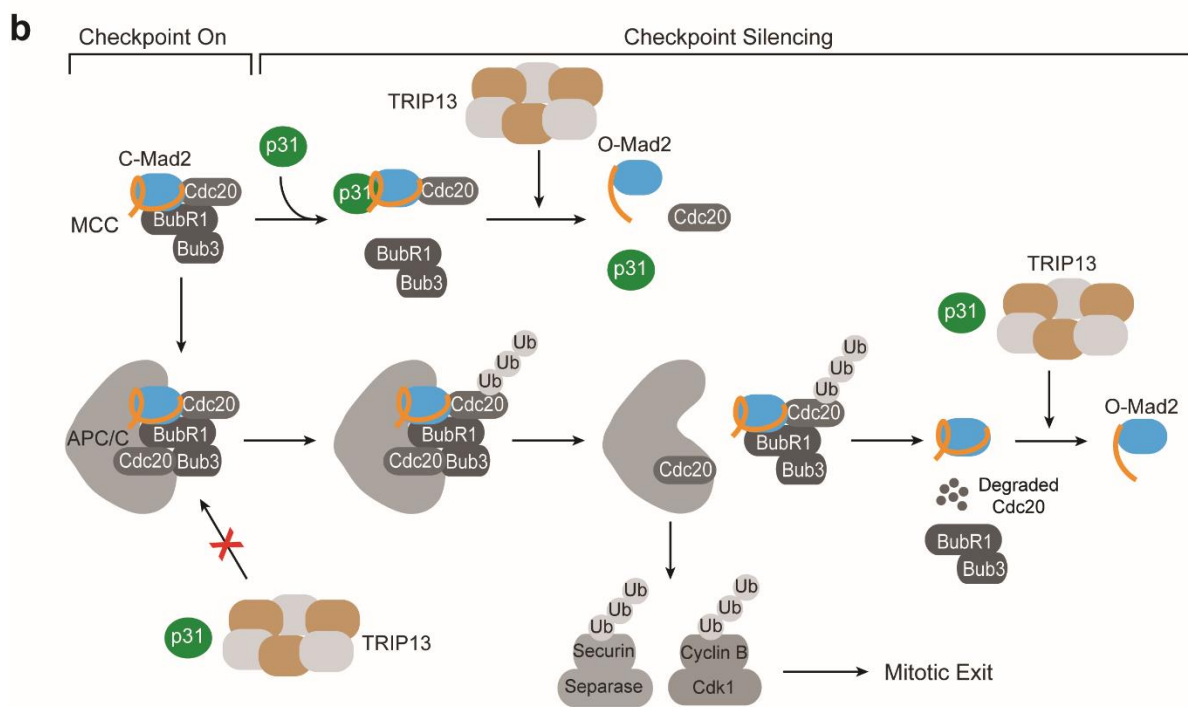
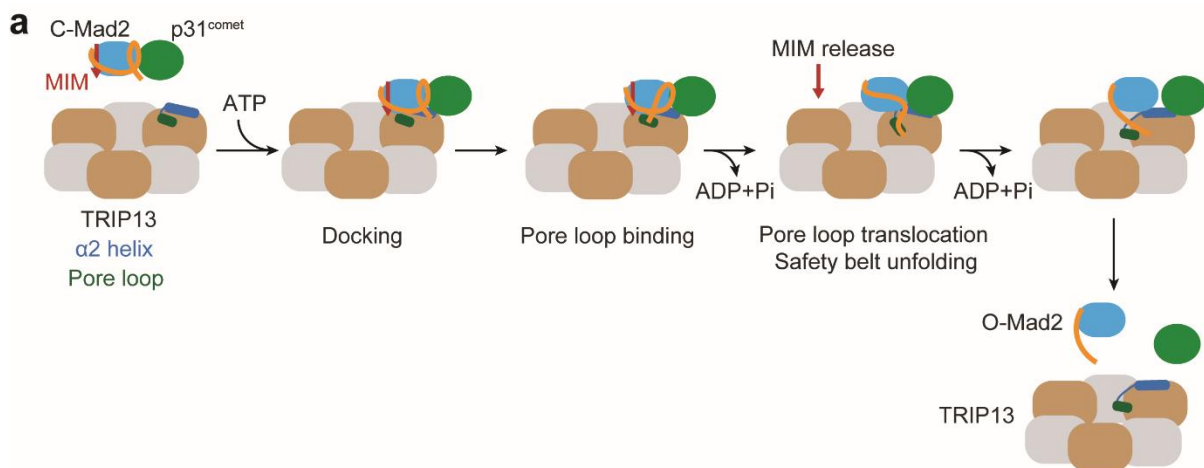


**Figure 19: Mechanisms of TRIP13-dependent Mad2 conformational change and checkpoint silencing.** (a) Model of TRIP13-catalyzed conversion of C-Mad2 to O-Mad2. The p31<sup>comet</sup>-C-Mad2-MIM complex docks on the  $\alpha 2$  helix of TRIP13. The pore loop of TRIP13 engages the C-terminus of Mad2. ATP hydrolysis drives the translocation of the pore loop and the associated Mad2 C-terminus, leading to the local unfolding of the C-terminal safety belt of C-Mad2. This Mad2 local unfolding releases MIM and disrupts the p31<sup>comet</sup>-Mad2 interaction. Mad2 refolding produces O-Mad2. Both p31<sup>comet</sup> and O-Mad2 dissociate from TRIP13. (b) Model of TRIP13-dependent checkpoint silencing. Upon spindle checkpoint activation, MCC is produced at unattached kinetochores and diffuses into the cytosol to inhibit APC/C<sup>Cdc20</sup>. During checkpoint silencing, the production of MCC is attenuated. p31<sup>comet</sup> binds to C-Mad2 in MCC and displaces BubR1-Bub3 from MCC. TRIP13 then binds to p31<sup>comet</sup>-C-Mad2-Cdc20, disassembles the C-Mad2-Cdc20 complex, and converts C-Mad2 to O-Mad2. Because TRIP13 cannot act on MCC already bound to APC/C<sup>Cdc20</sup>, MCC must first be released from APC/C<sup>Cdc20</sup> through alternative mechanisms. Cdc20 ubiquitination is a potential MCC-releasing mechanism. Proteasome-mediated degradation of ubiquitinated Cdc20 then disassembles MCC. C-Mad2 that persists during this process can be recognized by p31<sup>comet</sup> and TRIP13, and converted to O-Mad2. Collectively, these mechanisms reduce the levels of MCC and promote the activation of APC/C<sup>Cdc20</sup>, which ubiquitinates securin and cyclin B1 to trigger chromosome segregation and mitotic exit.

## **CHAPTER FOUR**

### **Exploring Chemical Inhibition of the TRIP13 Oncoprotein**

#### **INTRODUCTION**

Genomic instability is a hallmark of cancer (Hanahan and Weinberg, 2011). As previously discussed, the spindle checkpoint protects against genomic instability by ensuring the proper chromosome segregation in mitosis. As TRIP13 is involved in silencing the spindle checkpoint, overexpression or overactivation of TRIP13 may lead to premature mitotic exit, generating aneuploidy and other forms of genomic instability that can lead to cancer. Indeed, TRIP13 has been suggested as an oncogene even before the discovery of its role in mitosis in 2014 (Eytan et al., 2014; Wang et al., 2014a).

In 2008, TRIP13 was found to have a high copy number increase in non-small cell lung cancer (Kang et al., 2008), and in 2012 it was discovered that overexpression of TRIP13 predicted recurrence in prostate cancer (Larkin et al., 2012). In one of the first papers that described TRIP13 as a spindle checkpoint protein, Wang et al. (2014) determined that knockdown of the gene reduced invasion in breast cancer cell lines. Overexpression of TRIP13 in breast cancer was later described as being associated with poor clinical outcome (Nieto-Jimenez et al., 2016). TRIP13 is also overexpressed in squamous cell carcinoma of the head and neck (SCCHN) (Banerjee et al., 2014), colorectal cancer (CRC) (Kurita et al., 2016), chronic lymphocytic leukemia (Zhou et al., 2017), lung cancer in Xuanwei, China (Zhang et al., 2017), and multiple myeloma (Tao et al., 2017). In CRC cell lines, knockdown of TRIP13 reduced cell migration and invasion (Kurita et al., 2016). In both SCCHN and multiple myeloma, extensive studies were performed to assess TRIP13's role as an oncogene (Banerjee et al., 2014; Tao et al., 2017). Both studies showed that knockdown of TRIP13 in mouse

xenograft models reduced tumor growth (Banerjee et al., 2014; Tao et al., 2017). Clearly, TRIP13 is an oncogene in a variety of cancer types.

Given TRIP13's important role in promoting mitotic exit and the evidence that it is an oncogene in a variety of cancers, we hypothesized that chemical inhibition of TRIP13 may block mitotic exit by prolonging the spindle checkpoint, leading to mitotic arrest and cell death. We further chose TRIP13 as a cancer target because it has catalytic activity as a AAA+ ATPase. ATP analogs have been successfully used to target kinases and other ATPases for cancer treatment. In fact, an ATP-competitive inhibitor for the AAA+ ATPase p97/VCP, CB-5083, entered phase 1 clinical trials in 2014 for treatment of multiple myeloma (Zhou et al., 2015). Furthermore, we theorized that an allosteric inhibitor that affected ATPase activity, TRIP13 hexamerization, or binding to p31<sup>comet</sup>-Mad2 may also be effective in blocking mitotic exit.

We therefore designed a high-throughput screen (HTS) in 384-well format to identify chemical inhibitors of TRIP13. The screen was developed using an *in vitro* ATPase assay, ADP-Glo™ (Promega), to simultaneously assess TRIP13's ATPase activity and ATPase stimulation by p31<sup>comet</sup>-Mad2. Screening was first performed on an 8,000 compound library to assess the fidelity of the ADP Glo™ assay and of the secondary assays used to confirm lead compounds. A 200,000 compound library screen was then performed. After confirmation screens using several secondary assays, 12 lead compounds were identified as TRIP13 inhibitors. Five of these compounds were toxoflavin derivatives, and are termed "redox cyclers" due to the generation of hydrogen peroxide (H<sub>2</sub>O<sub>2</sub>) in the presence of DTT (Baell and Walters, 2014; Raouf et al., 2013; Thorne et al., 2010). Since H<sub>2</sub>O<sub>2</sub> can oxidize proteins and

therefore indirectly inhibit protein activity, the toxoflavins were eliminated as potential inhibitors. Three additional compounds were identified as redox cyclers and eliminated. One was eliminated due to the presence of toxic mercury in the compound. Finally, the remaining three hits were tested again for inhibition of TRIP13 and did not repeat consistently as inhibitors of the protein under the current experimental conditions. Therefore, we have not yet identified chemical inhibitors of TRIP13, demonstrating that TRIP13 may be a difficult protein to target.

## RESULTS

### Development of an HTS assay for inhibitors of TRIP13

TRIP13 harnesses the energy of ATP hydrolysis to catalyze the conversion of C-Mad2 to O-Mad2. There are many assays that have been developed to measure ATP hydrolysis, and we decided to take advantage of those systems to develop an HTS assay for inhibitors of TRIP13. We initially tested the Kinase-Glo® Luminescent Kinase Assay kit (Promega), which measures the amount of ATP in a reaction by coupling luciferase to a proprietary buffer system to generate a luminescent signal. While this assay was successful in measuring the ATPase activity of TRIP13, we observed a lower activity than we expected due to the detection limit of the assay (Fig. 20a). Kinase-Glo® requires that a maximum of only 10  $\mu$ M of ATP is used in the reaction. This is very close to the approximate  $K_M$  of TRIP13 (Ye et al., 2015), and thus leads to a low rate of ATP hydrolysis. Furthermore, the TRIP13 catalytically dead mutant, E253A, consistently reported a negative activity score in the assay, calling into question the validity of the results. Finally, we were only able to use the Kinase Glo® assay with a 10  $\mu$ L

reaction volume and 200 nM of TRIP13 protein, which would require a substantial amount of protein for HTS.

We thus tested the ADP-Glo™ Kinase Assay (Promega). This assay measures the amount of ADP produced by the hydrolysis of ATP, also by coupling luciferase to a proprietary buffer system to generate a luminescent signal. ADP-Glo™ differs from Kinase-Glo® in that it allows for up to 1 mM of ATP to be used in the reaction, and it can be used with a reaction volume of only 5 µL. As described in Chapter III, we found that p31<sup>comet</sup>-Mad2 robustly stimulated the ATPase activity of TRIP13 in this assay. We were therefore able to reduce the concentration of TRIP13 to 25 nM. The lower reaction volume and lower concentration amounted to an 8-fold decrease in the amount of protein required for the ADP-Glo™ assay compared to the Kinase-Glo® assay. The optimization of the assay is described in Chapter III.

We next tested the fidelity of the ADP-Glo™ assay for high-throughput screening by performing the assay on a large number of replicates and by calculating the Z-factor (Z') of TRIP WT to controls. This is a statistical measurement that calculates the difference in the experimental condition versus the controls by taking into account both the average of a set of samples and the standard deviation of the samples. An assay with a Z-factor of 0.5 or higher is considered a strong assay for HTS, while less than 0.5 is not a viable assay. It is calculated by the following equation ( $\mu$  = mean,  $\sigma$  = standard deviation, p = positive control, n = negative control):

$$Z' = 1 - \frac{3(\sigma_p + \sigma_n)}{|\mu_p - \mu_n|}$$

In our case, TRIP13 WT + p31<sup>comet</sup> + Mad2 was the positive control, and TRIP13 E253A + p31<sup>comet</sup> + Mad2 or p31<sup>comet</sup> + Mad2 (no TRIP13) was the negative control. The Z-factor for

TRIP13 WT + p31<sup>comet</sup> + Mad2 versus p31<sup>comet</sup> + Mad2 (no TRIP13) was 0.525, and for TRIP13 WT + p31<sup>comet</sup> + Mad2 versus TRIP13 E253A + p31<sup>comet</sup> + Mad2 was 0.634 (Fig. 21b). Therefore, the ADP-Glo™ assay is a suitable assay for identifying inhibitors of TRIP13. TRIP13 E253A + p31<sup>comet</sup> + Mad2 was chosen as the negative control for this assay since it had a higher Z-factor.

### **Development of a counter-screen to identify non-specific inhibitors of AAA+ ATPases**

TRIP13 belongs to the AAA+ ATPase family. We wished to identify inhibitors that were specific to TRIP13 and do not inhibit other family members. As such, we chose to counter-screen all inhibitors against the AAA+ ATPase p97/VCP because it is a well-characterized protein that has several identified inhibitors (Alvarez et al., 2016; Banerjee et al., 2016; Chou et al., 2014; Zhou et al., 2015). We chose to use the CB-5083 inhibitor as a negative control for p97/VCP activity (Zhou et al., 2015). We purified p97/VCP (Fig. 20c), and tested it in the ADP-Glo™ assay with a dose response of CB-5083 to determine the minimal concentration to use in the counter-screen. p97/VCP showed robust ATPase activity that was inhibited by CB-5083, whereas TRIP13 was not inhibited by CB-5083 (Fig. 20d). The chosen dose for CB-5083 was 250 nM. Inhibition of p97/VCP is thus a viable counter-screen to identify and eliminate non-specific inhibitors of TRIP13 ATPase activity.

### **Secondary screening of lead compounds from the 8,000 compound screen**

To further ensure the fidelity of the ATPase assay for HTS, we first tested it on an 8,000 compound screen with 5  $\mu$ M of each compound. The screen identified 329 statistically

significant hits for inhibition of TRIP13. Several hits were eliminated because they were pan-assay interference compounds (PAINS), compounds that are known to appear as hits in multiple high-throughput screens due to off-target effects. The hit list was further reduced by choosing only the compounds that had an activity score of -10 or lower. The activity score is calculated as:

$$\frac{(\text{sampleRawValues} - \text{medianOfDMSOcontrols})}{(\text{medianOfPositiveControls} - \text{medianOfDMSOcontrols})} \times 100$$

Therefore, the DMSO controls are set to 0 and the TRIP13 E253A negative controls are set to -100 to represent complete inhibition. An activity score of -10 is thus approximately 10% inhibition, -50 would be 50% inhibition, etc. This left 142 inhibitors, and the top 90 were chosen to be repeated in the ADP-Glo™ assay at three different concentrations (16.2 μM, 5 μM, 1.25 μM), all in triplicate. Of the 90 compounds, 18 had an activity score of -30 or lower at 16.2 μM. These 18 were chosen for secondary screening. A summary of the 8,000 compound screen is in Figure 21a. The activity scores of the 18 lead compounds are in Table 2.

The Mad2 dissociation assay described in Chapter III was chosen for secondary screening as it assesses the ability of TRIP13 to convert C-Mad2 to O-Mad2. The assay was performed with 20 μM of each of the 18 compounds. Of the 18 compounds, only one – SW104317 – significantly inhibited TRIP13 (Fig. 21b). The chemical structure of SW104317 is shown in Figure 21c. This compound was then tested for inhibition of p97/VCP in the ADP-Glo™ assay, and it was found to inhibit p97/VCP by about 50% (Fig. 21d). TRIP13 was also inhibited by about 50%. Therefore, SW104317 is a non-specific inhibitor of AAA+ ATPases, and is not a good candidate for specific inhibition of TRIP13. While the 8,000 compound screen did not identify any inhibitors for TRIP13, it did demonstrate that the ADP-Glo™ assay

is suitable for HTS, and that the Mad2 dissociation assay and p97/VCP assay are appropriate secondary screens for the identification of specific TRIP13 inhibitors.

### **Secondary screening of lead compounds from the screen of 200,000 compounds**

We next performed an HTS for inhibitors of TRIP13 using the compound library at UT Southwestern, which contains over 200,000 compounds and natural product fractions. Compounds were screened at 5  $\mu$ M. The screen identified 4,938 statistically significant hits for inhibition of TRIP13 (hits were 3 standard deviations or more below the negative control). PAINS compounds and compounds with an activity score greater than -20 were eliminated, leaving 286 lead compounds. These compounds were repeated in the ADP-Glo™ assay at three different concentrations (16.2  $\mu$ M, 5  $\mu$ M, 1.25  $\mu$ M), all in triplicate, and were tested with both TRIP13 and p97/VCP. At this time, we decided to follow-up only on those compounds that had identified chemical structures, and thus any unidentified natural products were eliminated as lead compounds. There were 54 compounds with identified structures that repeated with activity scores lower than -20 at 5  $\mu$ M compound. Though several of these compounds also inhibited p97/VCP with varying activity scores, we decided to continue testing them as non-specific inhibitors of AAA+ ATPases. A summary of the 200,000 compound screen is in Figure 22.

The 54 lead compounds were then tested in the Mad2 dissociation assay. At 5  $\mu$ M concentration, seven compounds inhibited Mad2 dissociation from its ligand and presumably the conversion of C-Mad2 to O-Mad2 – SW105179, SW049330, SW014419, SW125395, SW014421, SW041693, and SW044938 (Fig. 23a). At 20  $\mu$ M concentration, an additional five

compounds inhibited the conversion of C-Mad2 to O-Mad2 – SW154207, SW109708, SW196245, SW199253, and SW101308 (Fig. 23b). We therefore identified 12 lead compounds for inhibition of TRIP13. The activity scores with TRIP13 and p97/VCP for the 12 compounds are in Table 3.

### **Toxoflavins and other lead compounds interfere with the ATPase assay by redox cycling**

We next examined the structures of the 12 lead compounds (Fig. 24). Compound SW014419 is toxoflavin, a natural pigment discovered in 1934 to be produced by *Bacterium bongkrek* under aerobic conditions (Stern, 1935). It is produced by several other species of bacteria as well (Kim et al., 2004; Latuasan and Berends, 1961; Philmus et al., 2015). Four of the other compounds also had the toxoflavin ring in their structures (Fig. 24a). Toxoflavins are known as “redox cyclers” because they produce H<sub>2</sub>O<sub>2</sub> in the presence of reducing agents such as DTT, which was used in our buffer systems for both the ADP-Glo™ assay and the Mad2 dissociation assay. Since H<sub>2</sub>O<sub>2</sub> can oxidize proteins and therefore indirectly inhibit protein activity, toxoflavins are considered PAINS compounds (Baell and Walters, 2014; Johnston et al., 2008; Raof et al., 2013; Soares et al., 2010; Thorne et al., 2010). Unfortunately, they were not delineated as such in the UT Southwestern compound database. We therefore concluded that the five toxoflavin compounds were not specific inhibitors of TRIP13.

The knowledge that the toxoflavins are redox cyclers made us wary that the other seven lead compounds for inhibitors of TRIP13 (Fig. 24b) may also produce H<sub>2</sub>O<sub>2</sub> in our buffer system. We therefore tested these compounds for the generation of H<sub>2</sub>O<sub>2</sub> using an established colorimetric assay (Johnston et al., 2008). Known concentrations of H<sub>2</sub>O<sub>2</sub> were used in the

assay, and three of the toxoflavins were used as positive controls. When used at 1  $\mu\text{M}$ , the toxoflavins generated approximately 500  $\mu\text{M}$  of  $\text{H}_2\text{O}_2$  after 1 hour incubation in buffer containing DTT (Fig. 25a). Three of the seven remaining lead compounds also generated  $\text{H}_2\text{O}_2$  (Fig. 25a), and are therefore redox cyclers and not specific inhibitors of TRIP13. Expectedly, all of the redox cycling compounds also inhibited p97/VCP in the ADP-Glo™ assay (Table 3).

There were four remaining compounds for inhibition of TRIP13. Compound SW199253 contains mercury, which might be non-specifically toxic to cells, and it was thus eliminated as a lead compound. The remaining three compounds did not generate  $\text{H}_2\text{O}_2$  even at high concentrations (Fig. 25b). We therefore repeated the Mad2 dissociation assay with these compounds, and found that while the toxoflavin SW105179 inhibited C-Mad2 to O-Mad2 conversion, the three remaining lead compounds did not (Fig. 25c). Therefore, none of our original 12 lead compounds are specific inhibitors for TRIP13.

We then returned to the list of 54 lead compounds from the 200,000 compound screen. We noticed that compound SW056958 had the highest inhibition of TRIP13 ATPase activity. I confirmed this by repeating the ATPase assay (Figure 26a). I also tested SW056958 in the  $\text{H}_2\text{O}_2$  assay, and found it was not a redox cyler (Figure 26b). Though SW056958 did not prevent Mad2 dissociation from beads by TRIP13 (Figure 23), we thought that it may still be an inhibitor for TRIP13 ATPase activity. This would be reminiscent of the TRIP13 G320A mutation discussed in Chapter III (Figures 11 and 13). We, therefore, need to develop better experiments to assess the relationship between inhibition of TRIP13 ATPase activity, and the ability of TRIP13 to catalyze the conformation change of Mad2. SW056958 remains a candidate compound for inhibition of TRIP13 enzymatic activity.

## DISCUSSION

TRIP13 is a potential oncogene in a variety of cancers, and its ATPase activity makes it an attractive target for chemical inhibition. We developed a high-throughput ATPase assay to assess TRIP13 activity using the ADP-Glo™ Kinase Assay (Promega), and also applied this assay to measure the activity of another AAA+ ATPase, p97/VCP. We performed an 8000 compound screen and a 200,000 compound screen to identify chemical inhibitors of TRIP13. Initial compounds for inhibition of TRIP13 were first confirmed by repeating the ADP-Glo™ assay at three concentrations and in triplicate, and the resulting hits were further confirmed in the Mad2 dissociation assay. This resulted in 12 lead compounds for inhibition of TRIP13. Eight of the lead compounds were redox cyclers that non-specifically inhibit proteins, and one contained mercury, another non-specific toxin. The remaining three compounds did not show consistent inhibition of C-Mad2 to O-Mad2 conversion, eliminating all 12 compounds as specific inhibitors of TRIP13.

However, we identified that SW056958, from the original list of 54 compounds, was a partial inhibitor of TRIP13 ATPase activity (Figure 26a), though it did not show inhibition of TRIP13-induced Mad2 dissociation from beads (Figure 23). This is similar to the TRIP13 G320A mutation (Chapter III, Figures 11 and 13), and therefore SW056958 remains a candidate for TRIP13 inhibition. We are currently developing better assays to correlate partial inhibition of TRIP13 ATPase activity with TRIP13's ability to catalyze the conformational change of Mad2.

We were initially interested in targeting TRIP13 because, as an ATPase, it could be susceptible to inhibition by non-hydrolysable ATP analogs. There are many such analogs in

the UT Southwestern compound library, however none of them inhibited TRIP13 specifically. We speculate that TRIP13 may be a difficult protein to target enzymatically because it binds ATP very tightly, and a non-hydrolysable analog may not be able to compete for binding.

We were also interested in identifying allosteric inhibitors of TRIP13 that could disrupt binding to p31<sup>comet</sup>-Mad2 or hexamerization. The binding interface of p31<sup>comet</sup>-Mad2 is extensive (Fig. 15), and thus a small chemical inhibitor may not be able to completely disrupt TRIP13 binding to p31<sup>comet</sup>-Mad2. The hexamerization of TRIP13 may be difficult to target because of the dynamic nature of hexamerization, revealed by both the structure of the protein and the role of the hinge region (see Chapter III). However, compound SW056958 may be disrupting hexamerization since its activity is similar to the TRIP13 G320A hinge mutation.

An important lesson from this screen is the identification of the toxoflavins and the other redox cycling compounds. Several publications have identified this class of compounds as PAINS (Baell and Walters, 2014; Johnston et al., 2008; Raouf et al., 2013; Soares et al., 2010; Thorne et al., 2010), however they were not labelled as such in the UT Southwestern library. Furthermore, the toxoflavin compounds continue to be identified as specific inhibitors despite this classification. For example, in 2017 it was suggested that toxoflavin disrupts TCF/ $\beta$ -catenin binding (Martinez-Font et al., 2017) and that it is an inhibitor of KDM4A (Franci et al., 2017). It may be prudent when using large compounds libraries to ensure they have been screened for redox cycling compounds before following up on lead compounds that prove to be non-specific inhibitors.

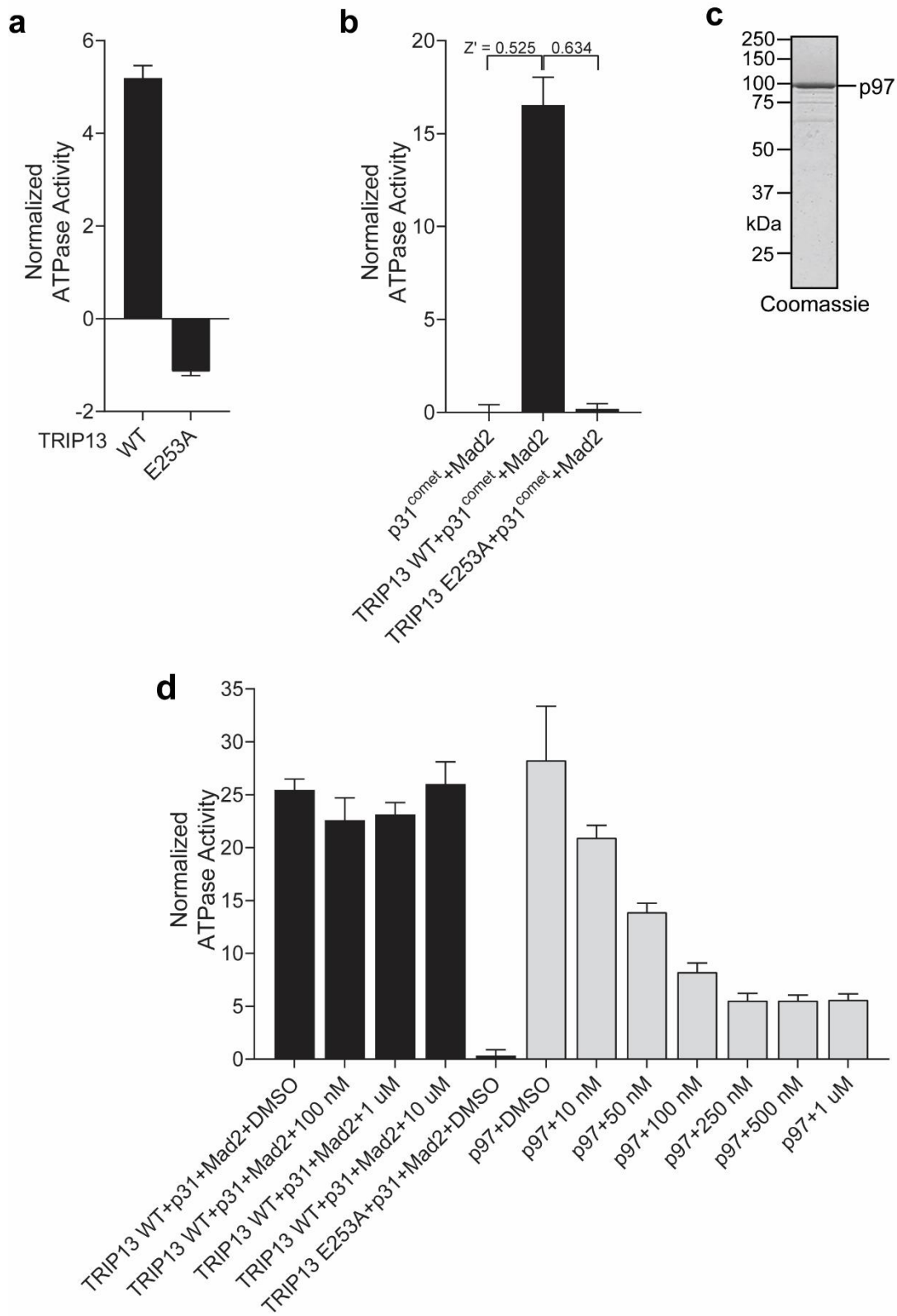


**Figure 20: Development of a HTS assay for inhibitors of TRIP13.** (a) Normalized ATPase activities of TRIP13 WT and TRIP13 E253A at 200 nM using the Kinase Glo® assay. Mean  $\pm$  SD;  $n = 3$  independent experiments. (b) Normalized ATPase activities of TRIP13 WT and TRIP13 E253A at 25 nM with 50 nM  $\Delta$ N35-p31<sup>comet</sup>-Mad2<sup>L13A</sup> using the ADP Glo™ assay. Mean  $\pm$  SD;  $n = 40$  independent experiments.  $Z'$  = calculated Z-factor. (c) Coomassie-stained SDS-PAGE gel of recombinant purified p97/VCP. (d) Normalized ATPase activities of TRIP13 WT and TRIP13 E253A at 25 nM with 50 nM  $\Delta$ N35-p31<sup>comet</sup>-Mad2<sup>L13A</sup> and of p97/VCP at 25 nM in the presence of the indicated concentrations of CB-5083 inhibitor using the ADP Glo™ assay. Mean  $\pm$  SD;  $n = 5$  independent experiments.

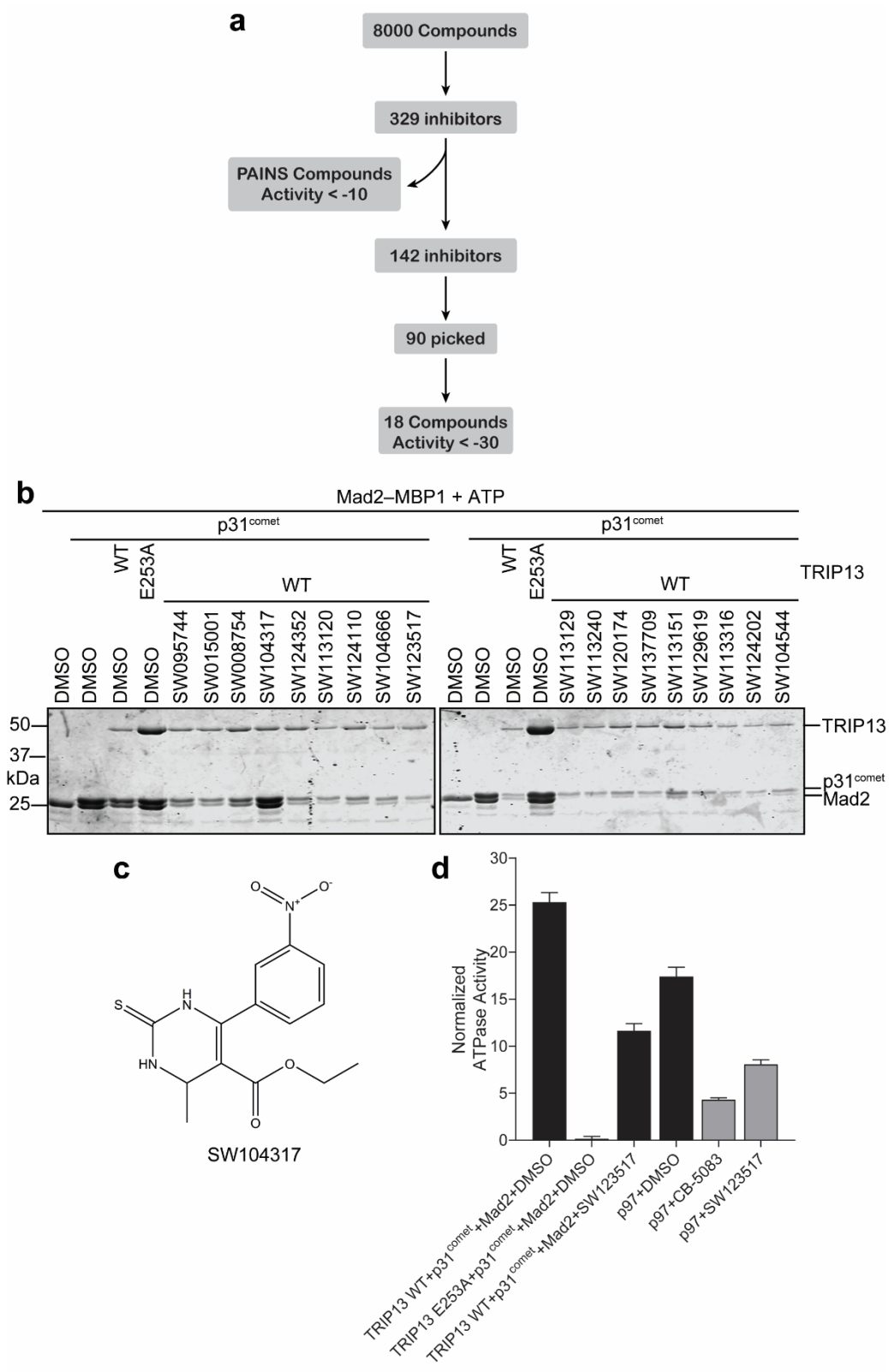


**Figure 21: No lead compounds for inhibition or activation of TRIP13 were identified in the 8000 compound screen.** (a) Schematic of results from the 8000 compound screen. (b) MBP1-coupled beads were first incubated with Mad2 and then incubated with TRIP13 WT or TRIP13 E253A (750 nM) in the presence of  $\Delta$ N35-p31<sup>comet</sup> (1.5  $\mu$ M), ATP (1 mM), and the indicated compound (20  $\mu$ M). Proteins bound to beads were analyzed by SDS-PAGE and stained with Coomassie blue. (c) Chemical structure of lead compound SW104317. (d) Normalized ATPase activities of TRIP13 WT and TRIP13 E253A at 25 nM with 50 nM  $\Delta$ N35-p31<sup>comet</sup>-Mad2<sup>L13A</sup> and of p97/VCP at 25 nM in the presence of the indicated compounds. Mean  $\pm$  SD; n = 5 independent experiments.

Table 2: Activity scores of the 18 lead compounds from the 8000 compound screen.

Barcode	Compound concentration: 16.2uM						TRIP13 ADP-Glo™						4.995uM						1.25uM					
	Activity[1]	Activity[2]	Activity[3]	Condensed_Activity	Activity[1]	Activity[2]	Activity[3]	Condensed_Activity	Activity[1]	Activity[2]	Activity[3]	Condensed_Activity	Activity[1]	Activity[2]	Activity[3]	Condensed_Activity	Activity[1]	Activity[2]	Activity[3]	Condensed_Activity				
SW095744-1	-91.2557	-93.1997	-90.8812	-91.2557	-53.5669	-60.8215	-51.0552	-53.5669	4.672532	-20.8637	-13.7851	-13.7851	4.672532	-20.8637	-13.7851	-13.7851	4.672532	-20.8637	-13.7851	-13.7851				
SW015001-1	-77.9125	-81.6539	-81.0128	-81.0128	-24.05	-29.7616	-29.6884	-29.6884	-2.59462	-6.0004	-5.94014	-5.94014	-2.59462	-6.0004	-5.94014	-5.94014	-2.59462	-6.0004	-5.94014	-5.94014				
SW008754-1	-66.2432	-67.386	-66.6999	-66.6999	-22.2498	-22.0056	-21.2159	-22.0056	-4.97492	-6.34382	-5.68809	-5.68809	-4.97492	-6.34382	-5.68809	-5.68809	-4.97492	-6.34382	-5.68809	-5.68809				
SW104317-1	-51.8973	-52.6314	-53.4108	-52.6314	-6.14013	-16.102	-13.1983	-13.1983	-3.96922	-13.1488	-9.80609	-9.80609	-3.96922	-13.1488	-9.80609	-9.80609	-3.96922	-13.1488	-9.80609	-9.80609				
SW124352-1	-39.8862	-48.5759	-55.4033	-48.5759	5.120262	-17.5037	-19.2525	-17.5037	-6.4031	-8.66925	-6.50756	-6.50756	-6.4031	-8.66925	-6.50756	-6.50756	-6.4031	-8.66925	-6.50756	-6.50756				
SW113120-1	-47.1152	-52.6192	-47.3094	-47.3094	-21.3229	-25.9653	-22.5142	-22.5142	-7.17108	-11.8853	-8.53489	-8.53489	-7.17108	-11.8853	-8.53489	-8.53489	-7.17108	-11.8853	-8.53489	-8.53489				
SW124110-1	-43.3245	-46.2872	-46.3963	-46.2872	-20.6036	-23.6067	-24.8867	-23.6067	-3.32441	-5.17678	-5.17678	-5.17678	-3.32441	-5.17678	-5.17678	-5.17678	-3.32441	-5.17678	-5.17678	-5.17678				
SW104666-1	-39.1287	-46.2613	-44.7237	-44.7237	-16.0727	-26.57	-22.405	-22.405	-1.0174	-16.4296	-11.0741	-11.0741	-1.0174	-16.4296	-11.0741	-11.0741	-1.0174	-16.4296	-11.0741	-11.0741				
SW113129-1	-44.0131	-46.154	-44.6488	-44.6488	-15.9064	-18.7125	-18.5139	-18.5139	-6.00217	-9.69517	-8.4541	-8.4541	-6.00217	-9.69517	-8.4541	-8.4541	-6.00217	-9.69517	-8.4541	-8.4541				
SW123517-1	-42.6274	-44.5939	-45.7532	-44.5939	-19.1785	-20.4591	-21.8796	-20.4591	-11.9317	-7.98962	-9.04544	-9.04544	-11.9317	-7.98962	-9.04544	-9.04544	-11.9317	-7.98962	-9.04544	-9.04544				
SW113240-1	-36.9104	-40.6284	-39.469	-39.469	-13.0969	-16.9472	-18.793	-16.9472	-4.41202	-7.52165	-6.73827	-6.73827	-4.41202	-7.52165	-6.73827	-6.73827	-4.41202	-7.52165	-6.73827	-6.73827				
SW120174-1	-36.5624	-37.8372	-33.4897	-36.5624	-19.1736	-18.5001	-16.82	-18.5001	-13.2102	-10.022	-7.27403	-7.27403	-13.2102	-10.022	-7.27403	-7.27403	-13.2102	-10.022	-7.27403	-7.27403				
SW137709-1	-27.08	-36.0647	-36.2771	-36.0647	-10.1746	-17.1682	-17.7726	-17.1682	-1.74227	-10.873	-11.2641	-11.2641	-1.74227	-10.873	-11.2641	-11.2641	-1.74227	-10.873	-11.2641	-11.2641				
SW113151-1	-28.3086	-39.0518	-32.8357	-32.8357	-10.522	-15.4209	-12.1346	-12.1346	-3.84666	-8.24304	-6.3182	-6.3182	-3.84666	-8.24304	-6.3182	-6.3182	-3.84666	-8.24304	-6.3182	-6.3182				
SW129619-1	-23.25	-32.2403	-31.7875	-31.7875	-8.42251	-8.97739	-12.3724	-8.97739	-1.82048	-3.49211	-3.49211	-3.49211	-1.82048	-3.49211	-3.49211	-3.49211	-1.82048	-3.49211	-3.49211	-3.49211				
SW113316-1	-30.5424	-37.0849	-31.7371	-31.7371	-11.1588	-16.5138	-12.9237	-12.9237	-2.98939	-7.33735	-6.03902	-6.03902	-2.98939	-7.33735	-6.03902	-6.03902	-2.98939	-7.33735	-6.03902	-6.03902				
SW124202-1	-31.4403	-33.7738	-30.2888	-30.2888	-16.8567	-19.269	-19.197	-19.197	-8.05361	-8.40071	-8.40071	-8.40071	-8.05361	-8.40071	-8.40071	-8.40071	-8.05361	-8.40071	-8.40071	-8.40071				
SW104544-1	-21.4393	-30.4901	-31.231	-30.4901	-4.76122	-15.418	-14.1626	-14.1626	2.102547	-8.85356	-6.45262	-6.45262	2.102547	-8.85356	-6.45262	-6.45262	2.102547	-8.85356	-6.45262	-6.45262				

**Condensed Activity:** The most representative single value of the triplicates. Values are obtained by two-point normalization.

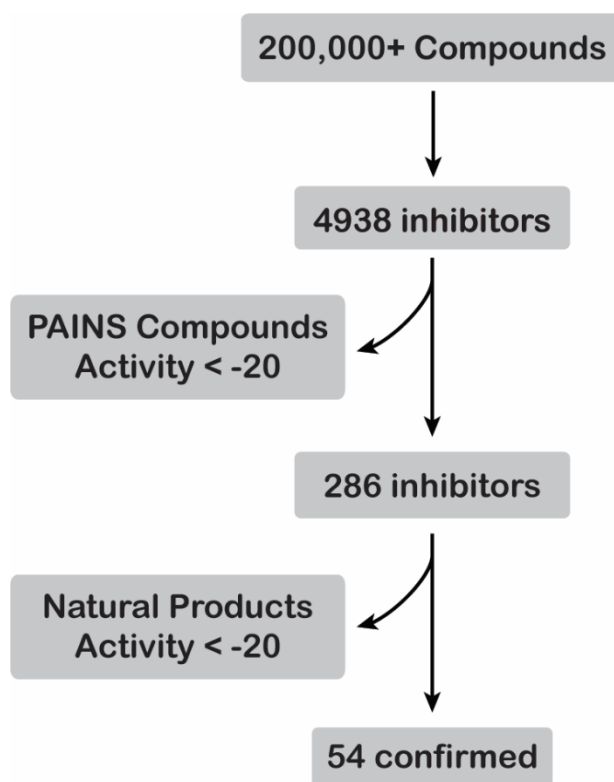


**Figure 22: The 200,000 compound screen identified 54 compounds that inhibit the ATPase activity of TRIP13.**

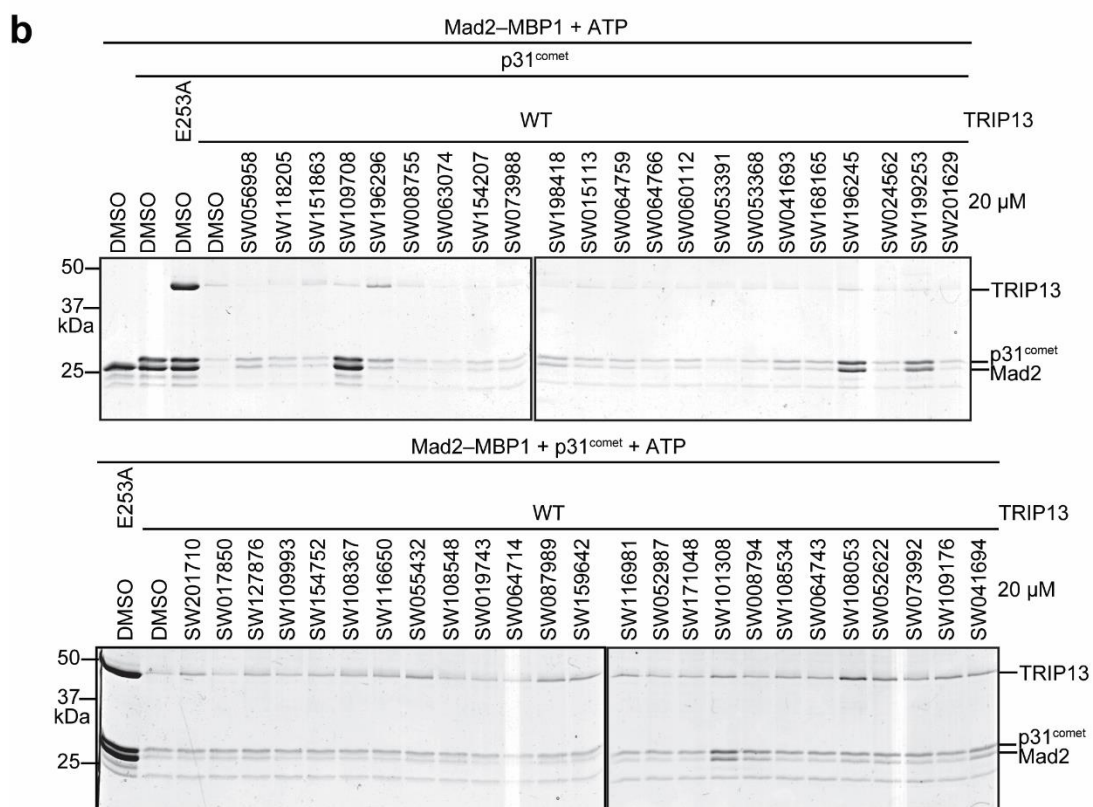
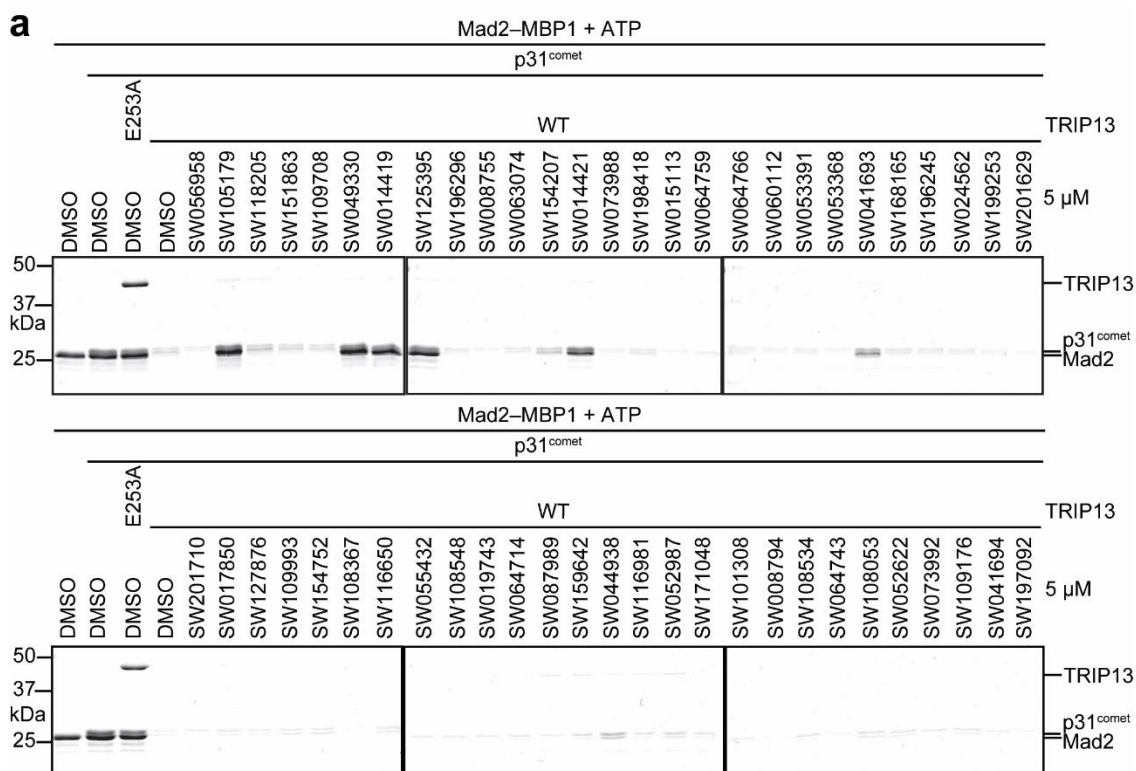


**Figure 23: Secondary screening identified 12 compounds that inhibit Mad2 conformational change by TRIP13.** MBP1-coupled beads were first incubated with Mad2 and then incubated with TRIP13 WT or TRIP13 E253A (500 nM) in the presence of  $\Delta$ N35-p31<sup>comet</sup> (1  $\mu$ M), ATP (1 mM), and the indicated compounds at either 5  $\mu$ M (**a**) or 20  $\mu$ M (**b**) concentration. Proteins bound to beads were analyzed by SDS-PAGE and stained with Coomassie blue.

Table 3: Activity scores of the 12 lead compounds from the 200,000 compound screen.

TRIP13 ADP-Glo™												
Barcode	Confirmation: 16.2uM			Confirmation: 4.995uM			Confirmation: 1.25uM					
	Activity[1]	Activity[2]	Activity[3]	Condensed_Activity	Activity[1]	Activity[2]	Activity[3]	Condensed_Activity	Activity[1]			Activity[2]
SW105179-1	-54.58776	-58.03891	-55.88416	-55.88416	-57.02235	-59.5307	-58.154	-58.154	-54.30239	-56.02687	-52.00863	-54.30239
SW049330-1	-45.92764	-39.51279	-43.85389	-43.85389	-55.17897	-49.6053	-53.076	-53.076	-59.22805	-53.54415	-56.25232	-56.25232
SW014419-1	-43.9047	-37.48939	-42.2079	-42.2079	-52.16343	-45.83197	-50.23619	-50.23619	-58.84472	-53.42478	-56.96962	-56.96962
SW125395-1	-36.47572	-40.60702	-37.61232	-37.61232	-47.86139	-51.30806	-48.78675	-48.78675	-55.47908	-57.94491	-56.42485	-56.42485
SW014421-1	-44.68242	-38.16386	-42.78786	-42.78786	-47.63905	-40.57329	-42.66448	-42.66448	-33.61719	-25.10841	-30.78055	-30.78055
SW154207-1	-50.34681	-53.29771	-51.259	-51.259	-40.89888	-42.90258	-43.08134	-42.90258	-15.99291	-16.5311	-22.1955	-16.5311
SW041693-1	-66.76805	-60.45693	-60.96206	-60.96206	-36.68515	-33.16838	-29.65036	-33.16838	-13.33345	-12.62842	-9.595619	-12.62842
SW044938-1	-47.96598	-43.26071	-46.32023	-46.32023	-22.37371	-23.87802	-24.15077	-23.87802	-8.700188	-11.55997	-7.518223	-8.700188
SW109708-1	-51.81162	-54.5837	-52.07869	-52.07869	-54.20145	-58.56288	-54.89579	-54.89579	-6.637197	-6.758072	-6.649016	-6.649016
SW196245-1	-61.37952	-66.1433	-60.0286	-60.0286	-29.33358	-30.90516	-31.13576	-30.90516	-6.774076	-4.054375	-6.074559	-5.774076
SW199253-1	-43.61969	-44.8829	-42.36073	-42.36073	-29.96718	-7.719045	-32.96106	-29.96718	-9.19612	-11.38991	-17.50493	-11.38991
SW101308-1	-26.97587	-28.02788	-22.00529	-22.00529	-22.98446	-23.46273	-16.00756	-22.98446	-15.40366	-14.61519	-9.584888	-14.61519
p97 ADP-Glo™												
Barcode	Counter: 16.2uM			Counter: 4.995uM			Counter: 1.25uM					
	Activity[1]	Activity[2]	Activity[3]	Condensed_Activity	Activity[1]	Activity[2]	Activity[3]	Condensed_Activity	Activity[1]			Activity[2]
SW105179-1	-31.53847	-31.78199	-23.41339	-31.53847	-27.72358	-28.30283	-22.18378	-27.72358	-18.85973	-18.09518	-13.10543	-18.09518
SW049330-1	-26.16111	-25.18269	-23.4413	-25.18269	-27.62145	-28.37906	-27.2849	-27.62145	-22.69683	-21.41519	-23.28293	-22.69683
SW014419-1	-27.34591	-23.83423	-28.37599	-27.34591	-25.61427	-20.42455	-24.65479	-24.65479	-26.62583	-22.33892	-23.46271	-23.46271
SW125395-1	-25.90528	-25.76476	-20.53438	-25.76476	-24.90194	-23.70625	-17.42629	-23.70625	-7.137076	1.135095	-22.73779	-7.137076
SW014421-1	-23.56555	-19.81663	-20.86134	-20.86134	-23.34103	-18.50142	-21.21173	-21.21173	-9.518817	-7.104269	-4.843488	-7.104269
SW154207-1	-1.22927	-2.120697	-0.6486455	-1.22927	1.227102	0.1682094	0.3139209	0.3139209	0.7513155	-1.155534	-1.128011	-1.128011
SW041693-1	-6.546169	-6.177886	-3.482967	-6.177886	0.0228615	-2.148263	0.5208497	0.02286148	3.093382	-1.503729	3.372717	3.093382
SW044938-1	-30.07168	-33.05397	-30.1043	-30.1043	-9.495347	-14.76703	-8.739494	-9.495347	2.805859	-6.199736	2.198878	2.198878
SW109708-1	-50.32601	-47.84763	-42.36686	-47.84763	-15.95137	-25.3835	-9.403019	-15.95137	-3.457315	-0.231978	-0.4924265	-0.4924265
SW196245-1	-13.73508	-14.0972	-12.32749	-13.73508	-16.34019	-14.42336	-10.79164	-14.42336	-0.252379	-1.671856	-4.363634	-1.671856
SW199253-1	-10.34008	-9.250713	-12.32978	-10.34008	-1.715678	0.702294	-4.697163	-1.715678	-3.681595	1.78032	26.21797	1.78032
SW101308-1	-8.676867	-2.1444	-0.6989072	-2.1444	-10.53674	-3.581985	-2.509407	-3.581985	-8.307384	0.8924789	0.3172787	0.3172787

Condensed Activity: The most representative single value of the triplicates.

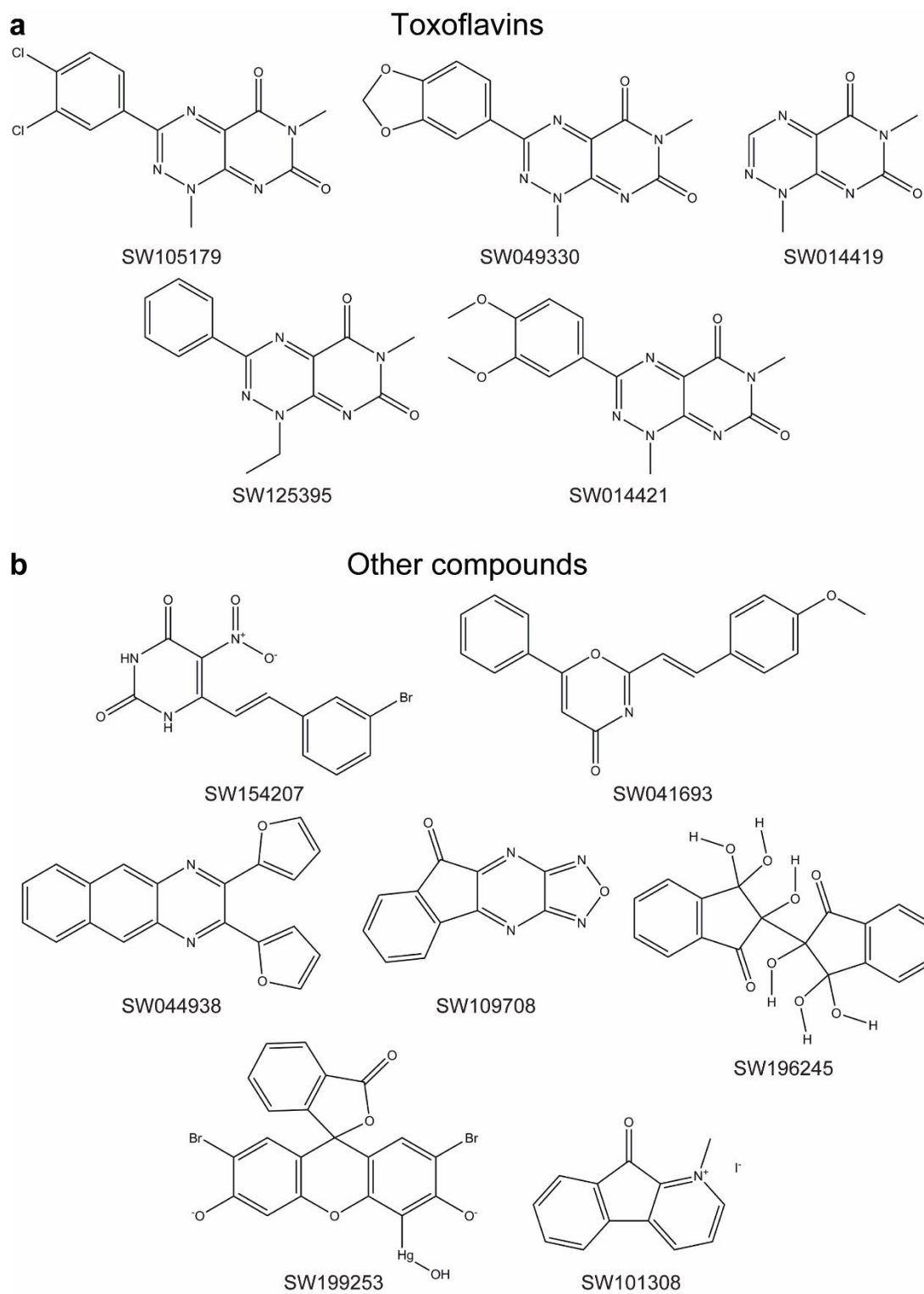


**Figure 24: Structures of lead compounds that may inhibit TRIP13. (a) Structures of compounds with the toxoflavin backbone. (b) Structures of non-toxoflavin compounds.**

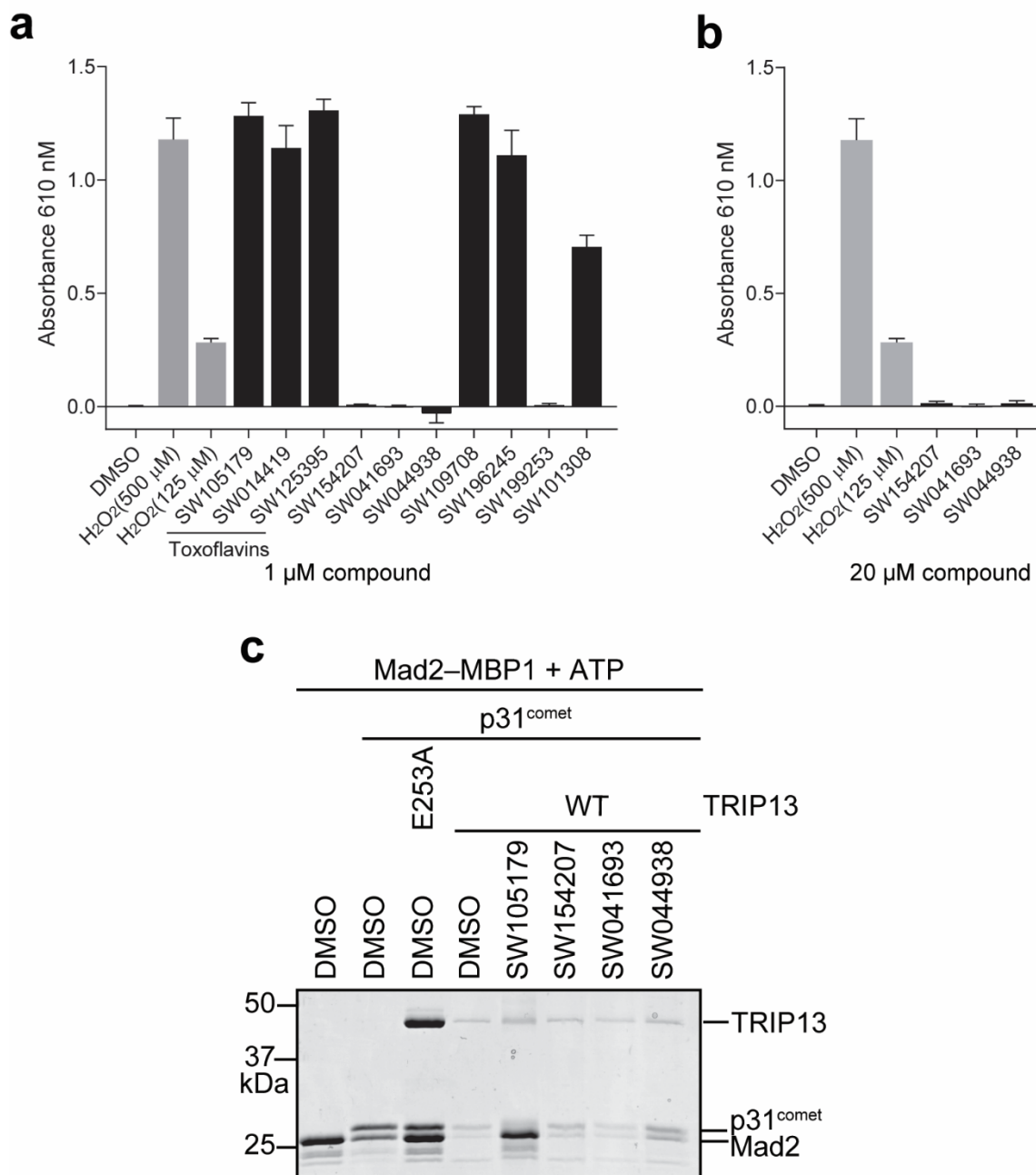


**Figure 25: Toxoflavins and other lead compounds interfere with the ATPase assay by redox cycling. (a)** The indicated compounds were tested at 1  $\mu$ M for the production of H<sub>2</sub>O<sub>2</sub> in the presence of ATPase buffer containing DTT. **(b)** The indicated compounds were tested at 20  $\mu$ M for the production of H<sub>2</sub>O<sub>2</sub> in the presence of ATPase buffer containing DTT. **(c)** MBP1-coupled beads were first incubated with Mad2 and then incubated with TRIP13 WT or TRIP13 E253A (500 nM) in the presence of  $\Delta$ N35-p31<sup>comet</sup> (1  $\mu$ M), ATP (1 mM), and the indicated compounds (20  $\mu$ M). Proteins bound to beads were analyzed by SDS-PAGE and stained with Coomassie blue.

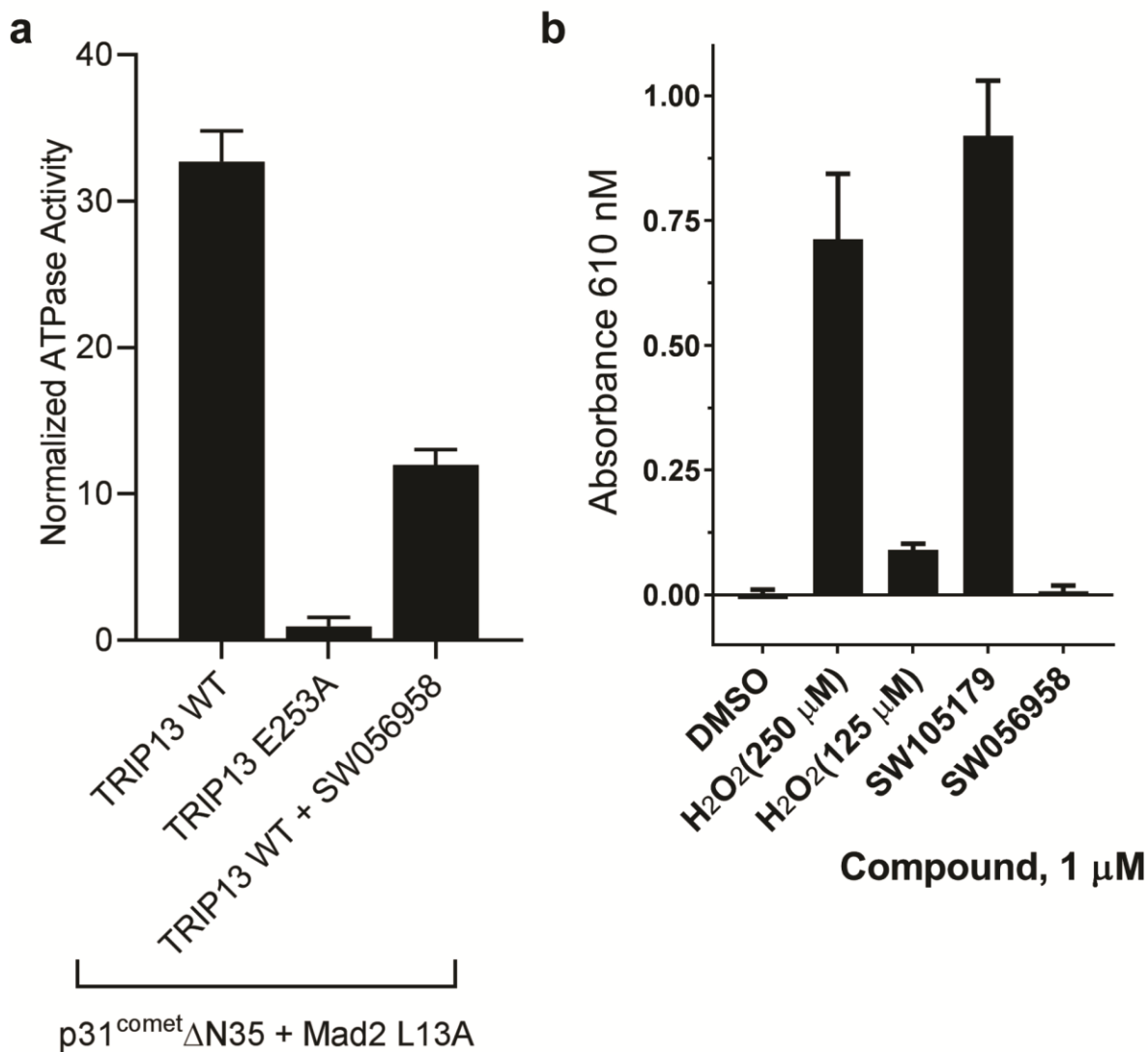


**Figure 26: Compound SW056958 may be a candidate for TRIP13 inhibition.** (a) Normalized ATPase activities of TRIP13 WT and TRIP13 E253A at 25 nM with 50 nM ΔN35-p31<sup>comet</sup>-Mad2<sup>L13A</sup> in the presence of DMSO or 10 μM SW056958. Mean ± SD; n = 8 independent experiments. (b) The indicated compounds were tested at 1 μM for the production of H<sub>2</sub>O<sub>2</sub> in the presence of ATPase buffer containing DTT.

## CHAPTER FIVE

### Perspectives

My work as described here has provided important insight into TRIP13-mediated spindle checkpoint silencing. The spindle checkpoint is an important mechanism for ensuring proper chromosome segregation during mitosis. Without the checkpoint, cells can develop aneuploidy, which can lead to diseases such as Down syndrome and cancer. Spindle checkpoint silencing is also crucial to cell survival and genomic integrity. Several mechanisms for spindle checkpoint silencing exist: the reduction of checkpoint signaling to halt checkpoint protein recruitment at kinetochores, the physical removal of checkpoint proteins from kinetochores, the cessation of MCC formation, and the disassembly of the MCC by both ubiquitination of Cdc20 and conformational change of Mad2. These processes likely work together to fine-tune checkpoint silencing such that it can occur quickly, explaining the classic image of fast chromosome segregation at the metaphase-to-anaphase transition that biologists have seen for over a century.

As described in Chapter III, I attempted to integrate some of these checkpoint silencing mechanisms by examining the specific mechanism of Mad2 conformational change by TRIP13-p31<sup>comet</sup>. I confirmed that TRIP13-p31<sup>comet</sup> physically converts C-Mad2 to O-Mad2 by locally unfolding the C-terminal region of the protein. By performing mutagenesis analysis, I discovered the binding site for p31<sup>comet</sup>-Mad2 on the TRIP13 pore loop and  $\alpha 2$  helix, and provided insight into how Mad2 is unfolded by the ATPase. Notably, I discovered that the hinge region of TRIP13 is important for hexamerization and for conformational dynamics of the ATPase. I identified a sequence motif on the hinge that is present in other AAA+ ATPases, and thus propose that this hinge motif may be required for the proper activities of these other

ATPases. Mutation of TRIP13 N278 revealed further insights into the conformational dynamics of TRIP13, demonstrating that the  $\alpha 3$  helix may be important for pore loop movement during Mad2 unfolding.

Arguably, the most insight into spindle checkpoint silencing came from the *in vitro* reconstitution of the process. I discovered that, in addition to converting free C-Mad to O-Mad2, TRIP13-p31<sup>comet</sup> can promote the dissociation of Mad2 from the diffusible MCC complex. However, it cannot access Mad2 in the MCC that is bound to APC/C. This led me to propose a model that integrates the activity of TRIP13 with two other spindle checkpoint silencing mechanisms: the ability of p31<sup>comet</sup> to displace BubR1 from Mad2 in the MCC, and the ubiquitination of Cdc20<sup>MCC</sup> by APC/C<sup>Cdc20</sup> (Figure 19). These findings provided insight into how the multiple mechanisms of checkpoint silencing work together to fine-tune the timing of chromosome segregation.

In my second project, I attempted to discover chemical inhibitors of TRIP13 for both mechanistic studies, and for feasibility studies on the potential of targeting TRIP13 in cancer therapy. I was able to identify only one candidate for inhibition, SW056958, which may suggest that TRIP13 is a difficult protein to target. Further experiments need to be performed before we can definitively prove that SW056958 is a potent and specific inhibitor of TRIP13. The search for an inhibitor did provide an important lesson for high-throughput compound screening: All hits from the large compound libraries should be screened for redox cyclers as a secondary screen before additional assays with the hits are performed. I hope that this lesson helps others avoid following false lead compounds in the future.

## BIBLIOGRAPHY

- Adams, P.D., Afonine, P.V., Bunkoczi, G., Chen, V.B., Davis, I.W., Echols, N., Headd, J.J., Hung, L.W., Kapral, G.J., Grosse-Kunstleve, R.W., *et al.* (2010). PHENIX: a comprehensive Python-based system for macromolecular structure solution. *Acta Crystallogr. D Biol. Crystallogr.* *66*, 213-221.
- Alfieri, C., Chang, L., Zhang, Z., Yang, J., Maslen, S., Skehel, M., and Barford, D. (2016). Molecular basis of APC/C regulation by the spindle assembly checkpoint. *Nature* *536*, 431-436.
- Alushin, G.M., Musinipally, V., Matson, D., Tooley, J., Stukenberg, P.T., and Nogales, E. (2012). Multimodal microtubule binding by the Ndc80 kinetochore complex. *Nature structural & molecular biology* *19*, 1161-1167.
- Alvarez, C., Bulfer, S.L., Chakrasali, R., Chimenti, M.S., Deshaies, R.J., Green, N., Kelly, M., LaPorte, M.G., Lewis, T.S., Liang, M., *et al.* (2016). Allosteric Indole Amide Inhibitors of p97: Identification of a Novel Probe of the Ubiquitin Pathway. *ACS medicinal chemistry letters* *7*, 182-187.
- Baell, J., and Walters, M.A. (2014). Chemistry: Chemical con artists foil drug discovery. *Nature* *513*, 481-483.
- Banerjee, R., Russo, N., Liu, M., Basrur, V., Bellile, E., Palanisamy, N., Scanlon, C.S., van Tubergen, E., Inglehart, R.C., Metwally, T., *et al.* (2014). TRIP13 promotes error-prone nonhomologous end joining and induces chemoresistance in head and neck cancer. *Nature communications* *5*, 4527.
- Banerjee, S., Bartesaghi, A., Merk, A., Rao, P., Bulfer, S.L., Yan, Y., Green, N., Mroczkowski, B., Neitz, R.J., Wipf, P., *et al.* (2016). 2.3 Å resolution cryo-EM structure of human p97 and mechanism of allosteric inhibition. *Science* *351*, 871-875.
- Barisic, M., and Geley, S. (2011). Spindly switch controls anaphase: spindly and RZZ functions in chromosome attachment and mitotic checkpoint control. *Cell cycle* *10*, 449-456.
- Bharadwaj, R., Qi, W., and Yu, H. (2004). Identification of two novel components of the human NDC80 kinetochore complex. *J. Biol. Chem.* *279*, 13076-13085.
- Bharadwaj, R., and Yu, H. (2004). The spindle checkpoint, aneuploidy, and cancer. *Oncogene* *23*, 2016-2027.
- Black, B.E., and Cleveland, D.W. (2011). Epigenetic centromere propagation and the nature of CENP-a nucleosomes. *Cell* *144*, 471-479.
- Black, B.E., Jansen, L.E., Maddox, P.S., Foltz, D.R., Desai, A.B., Shah, J.V., and Cleveland, D.W. (2007). Centromere identity maintained by nucleosomes assembled with histone H3 containing the CENP-A targeting domain. *Molecular cell* *25*, 309-322.
- Boveri, T. (1887). Ueber den Antheil des Spermatozoon an der Teilung des Eies. *Sitzungsber. Ges. Morph. Physiol. München* *3*, 151-164.
- Boveri, T. (1902). Über mehrpolige mitosen als mittel zur analyse des zellkerns. . *Verh. Phys. Med. Ges. Würzburg* *35*, 67-90.

- Boveri, T. (1904). Ergebnisse über die Konstitution der chromatischen Substanz des Zellkerns. Fisher, Jena.
- Boveri, T. (1914). Zur Frage der Entstehung Maligner Tumoren. . Gustav Fischer, Jena., 1-64.
- Brautigam, C.A. (2015). Calculations and Publication-Quality Illustrations for Analytical Ultracentrifugation Data. *Methods Enzymol.* 562, 109-133.
- Chang, L., and Barford, D. (2014). Insights into the anaphase-promoting complex: a molecular machine that regulates mitosis. *Current opinion in structural biology* 29, 1-9.
- Chao, W.C., Kulkarni, K., Zhang, Z., Kong, E.H., and Barford, D. (2012). Structure of the mitotic checkpoint complex. *Nature* 484, 208-213.
- Cheeseman, I.M., Chappie, J.S., Wilson-Kubalek, E.M., and Desai, A. (2006). The conserved KMN network constitutes the core microtubule-binding site of the kinetochore. *Cell* 127, 983-997.
- Cheeseman, I.M., and Desai, A. (2008). Molecular architecture of the kinetochore-microtubule interface. *Nature reviews. Molecular cell biology* 9, 33-46.
- Choi, E., Zhang, X., Xing, C., and Yu, H. (2016). Mitotic checkpoint regulators control insulin signaling and metabolic homeostasis. *Cell* 166, 567-581.
- Chou, T.F., Bulfer, S.L., Weihl, C.C., Li, K., Lis, L.G., Walters, M.A., Schoenen, F.J., Lin, H.J., Deshaies, R.J., and Arkin, M.R. (2014). Specific inhibition of p97/VCP ATPase and kinetic analysis demonstrate interaction between D1 and D2 ATPase domains. *Journal of molecular biology* 426, 2886-2899.
- Ciferri, C., Pasqualato, S., Screpanti, E., Varetto, G., Santaguida, S., Dos Reis, G., Maiolica, A., Polka, J., De Luca, J.G., De Wulf, P., *et al.* (2008). Implications for kinetochore-microtubule attachment from the structure of an engineered Ndc80 complex. *Cell* 133, 427-439.
- De Antoni, A., Pearson, C.G., Cimini, D., Canman, J.C., Sala, V., Nezi, L., Mapelli, M., Sironi, L., Faretta, M., Salmon, E.D., *et al.* (2005). The Mad1/Mad2 complex as a template for Mad2 activation in the spindle assembly checkpoint. *Curr. Biol.* 15, 214-225.
- Delaglio, F., Grzesiek, S., Vuister, G.W., Zhu, G., Pfeifer, J., and Bax, A. (1995). NMRPipe: a multidimensional spectral processing system based on UNIX pipes. *Journal of biomolecular NMR* 6, 277-293.
- DeLuca, J.G., Gall, W.E., Ciferri, C., Cimini, D., Musacchio, A., and Salmon, E.D. (2006). Kinetochore microtubule dynamics and attachment stability are regulated by Hec1. *Cell* 127, 969-982.
- Di Fiore, B., Davey, N.E., Hagting, A., Izawa, D., Mansfeld, J., Gibson, T.J., and Pines, J. (2015). The ABBA Motif Binds APC/C Activators and Is Shared by APC/C Substrates and Regulators. *Dev. Cell* 32, 358-372.
- Diaz-Martinez, L.A., Tian, W., Li, B., Warrington, R., Jia, L., Brautigam, C.A., Luo, X., and Yu, H. (2015). The Cdc20-binding Phe box of the spindle checkpoint protein BubR1 maintains the mitotic checkpoint complex during mitosis. *The Journal of biological chemistry* 290, 2431-2443.

- Emsley, P., and Cowtan, K. (2004). Coot: model-building tools for molecular graphics. *Acta Crystallogr. D Biol. Crystallogr.* *60*, 2126-2132.
- Eytan, E., Wang, K., Miniowitz-Shemtov, S., Sitry-Shevah, D., Kaisari, S., Yen, T.J., Liu, S.T., and Hershko, A. (2014). Disassembly of mitotic checkpoint complexes by the joint action of the AAA-ATPase TRIP13 and p31(comet). *Proceedings of the National Academy of Sciences of the United States of America* *111*, 12019-12024.
- Faesen, A.C., Thanasoula, M., Maffini, S., Breit, C., Muller, F., van Gerwen, S., Bange, T., and Musacchio, A. (2017). Basis of catalytic assembly of the mitotic checkpoint complex. *Nature* *542*, 498-502.
- Fang, G. (2002). Checkpoint protein BubR1 acts synergistically with Mad2 to inhibit anaphase-promoting complex. *Mol. Biol. Cell* *13*, 755-766.
- Fisk, H.A. (2015). The Discovery of the Mitotic Spindle Assembly Checkpoint. *Nature Education* *8*, 8.
- Flemming, W. (1882). *Zellsubstanz, Kern und Zelltheilung*. Leipzig, F. C. W. Vogel.
- Foster, S.A., and Morgan, D.O. (2012). The APC/C subunit Mnd2/Apc15 promotes Cdc20 autoubiquitination and spindle assembly checkpoint inactivation. *Molecular cell* *47*, 921-932.
- Franci, G., Sarno, F., Nebbioso, A., and Altucci, L. (2017). Identification and characterization of PKF118-310 as a KDM4A inhibitor. *Epigenetics* *12*, 198-205.
- Gassmann, R., Essex, A., Hu, J.S., Maddox, P.S., Motegi, F., Sugimoto, A., O'Rourke, S.M., Bowerman, B., McLeod, I., Yates, J.R., 3rd, *et al.* (2008). A new mechanism controlling kinetochore-microtubule interactions revealed by comparison of two dynein-targeting components: SPDL-1 and the Rod/Zwilch/Zw10 complex. *Genes & development* *22*, 2385-2399.
- Glynn, S.E., Martin, A., Nager, A.R., Baker, T.A., and Sauer, R.T. (2009). Structures of asymmetric ClpX hexamers reveal nucleotide-dependent motions in a AAA+ protein-unfolding machine. *Cell* *139*, 744-756.
- Glynn, S.E., Nager, A.R., Baker, T.A., and Sauer, R.T. (2012). Dynamic and static components power unfolding in topologically closed rings of a AAA+ proteolytic machine. *Nat. Struct. Mol. Biol.* *19*, 616-622.
- Griffis, E.R., Stuurman, N., and Vale, R.D. (2007). Spindly, a novel protein essential for silencing the spindle assembly checkpoint, recruits dynein to the kinetochore. *The Journal of cell biology* *177*, 1005-1015.
- Guimaraes, G.J., Dong, Y., McEwen, B.F., and Deluca, J.G. (2008). Kinetochore-microtubule attachment relies on the disordered N-terminal tail domain of Hec1. *Current biology : CB* *18*, 1778-1784.
- Habu, T., Kim, S.H., Weinstein, J., and Matsumoto, T. (2002). Identification of a MAD2-binding protein, CMT2, and its role in mitosis. *The EMBO journal* *21*, 6419-6428.
- Han, J.S., Vitre, B., Fachinetti, D., and Cleveland, D.W. (2014). Bimodal activation of BubR1 by Bub3 sustains mitotic checkpoint signaling. *Proceedings of the National Academy of Sciences of the United States of America* *111*, E4185-4193.
- Hanahan, D., and Weinberg, R.A. (2011). Hallmarks of cancer: the next generation. *Cell* *144*, 646-674.

- Hanson, P.I., and Whiteheart, S.W. (2005). AAA+ proteins: have engine, will work. *Nat. Rev. Mol. Cell Biol.* 6, 519-529.
- Hara, K., Hashimoto, H., Murakumo, Y., Kobayashi, S., Kogame, T., Unzai, S., Akashi, S., Takeda, S., Shimizu, T., and Sato, M. (2010). Crystal structure of human REV7 in complex with a human REV3 fragment and structural implication of the interaction between DNA polymerase zeta and REV1. *The Journal of biological chemistry* 285, 12299-12307.
- Hara, M., Ozkan, E., Sun, H., Yu, H., and Luo, X. (2015). Structure of an intermediate conformer of the spindle checkpoint protein Mad2. *Proceedings of the National Academy of Sciences of the United States of America* 112, 11252-11257.
- Hiruma, Y., Sacristan, C., Pachis, S.T., Adamopoulos, A., Kuijt, T., Ubbink, M., von Castelmur, E., Perrakis, A., and Kops, G.J. (2015). Competition between MPS1 and microtubules at kinetochores regulates spindle checkpoint signaling. *Science* 348, 1264-1267.
- Holland, A.J., and Cleveland, D.W. (2009). Boveri revisited: chromosomal instability, aneuploidy and tumorigenesis. *Nature reviews. Molecular cell biology* 10, 478-487.
- Howell, B.J., McEwen, B.F., Canman, J.C., Hoffman, D.B., Farrar, E.M., Rieder, C.L., and Salmon, E.D. (2001). Cytoplasmic dynein/dynactin drives kinetochore protein transport to the spindle poles and has a role in mitotic spindle checkpoint inactivation. *The Journal of cell biology* 155, 1159-1172.
- Hoyt, M.A., Totis, L., and Roberts, B.T. (1991). *S. cerevisiae* genes required for cell cycle arrest in response to loss of microtubule function. *Cell* 66, 507-517.
- Iosefson, O., Nager, A.R., Baker, T.A., and Sauer, R.T. (2015). Coordinated gripping of substrate by subunits of a AAA+ proteolytic machine. *Nature chemical biology* 11, 201-206.
- Izawa, D., and Pines, J. (2015). The mitotic checkpoint complex binds a second CDC20 to inhibit active APC/C. *Nature* 517, 631-634.
- Ji, Z., Gao, H., Jia, L., Li, B., and Yu, H. (2017). A sequential multi-target Mps1 phosphorylation cascade promotes spindle checkpoint signaling. *eLife* 6.
- Ji, Z., Gao, H., and Yu, H. (2015). Kinetochore attachment sensed by competitive Mps1 and microtubule binding to Ndc80C. *Science* 348, 1260-1264.
- Jia, L., Kim, S., and Yu, H. (2013). Tracking spindle checkpoint signals from kinetochores to APC/C. *Trends in biochemical sciences* 38, 302-311.
- Jia, L., Li, B., Warrington, R.T., Hao, X., Wang, S., and Yu, H. (2011). Defining pathways of spindle checkpoint silencing: functional redundancy between Cdc20 ubiquitination and p31(comet). *Molecular biology of the cell* 22, 4227-4235.
- Jia, L., Li, B., and Yu, H. (2016). The Bub1-Plk1 kinase complex promotes spindle checkpoint signalling through Cdc20 phosphorylation. *Nature communications* 7, 10818.
- Johnson, B.A., and Blevins, R.A. (1994). NMRView: A computer program for visualization and analysis of NMR data. *Journal of biomolecular NMR* 4, 603-614.
- Johnston, P.A., Soares, K.M., Shinde, S.N., Foster, C.A., Shun, T.Y., Takyi, H.K., Wipf, P., and Lazo, J.S. (2008). Development of a 384-well colorimetric assay to quantify

- hydrogen peroxide generated by the redox cycling of compounds in the presence of reducing agents. *Assay and drug development technologies* 6, 505-518.
- Kaisari, S., Sitry-Shevah, D., Miniowitz-Shemtov, S., Teichner, A., and Hershko, A. (2017). Role of CCT chaperonin in the disassembly of mitotic checkpoint complexes. *Proceedings of the National Academy of Sciences of the United States of America* 114, 956-961.
- Kang, J., Yang, M., Li, B., Qi, W., Zhang, C., Shokat, K.M., Tomchick, D.R., Machius, M., and Yu, H. (2008). Structure and substrate recruitment of the human spindle checkpoint kinase Bub1. *Mol. Cell* 32, 394-405.
- Kim, J., Kim, J.G., Kang, Y., Jang, J.Y., Jog, G.J., Lim, J.Y., Kim, S., Suga, H., Nagamatsu, T., and Hwang, I. (2004). Quorum sensing and the LysR-type transcriptional activator ToxR regulate toxoflavin biosynthesis and transport in *Burkholderia glumae*. *Molecular microbiology* 54, 921-934.
- Kim, S., and Yu, H. (2011). Mutual regulation between the spindle checkpoint and APC/C. *Seminars in cell & developmental biology* 22, 551-558.
- Kim, S., and Yu, H. (2015). Multiple assembly mechanisms anchor the KMN spindle checkpoint platform at human mitotic kinetochores. *J. Cell Biol.* 208, 181-196.
- Kim, Y., Rosenberg, S.C., Kugel, C.L., Kostow, N., Rog, O., Davydov, V., Su, T.Y., Dernburg, A.F., and Corbett, K.D. (2014). The chromosome axis controls meiotic events through a hierarchical assembly of HORMA domain proteins. *Developmental cell* 31, 487-502.
- Kiyomitsu, T., Obuse, C., and Yanagida, M. (2007). Human Blinkin/AF15q14 is required for chromosome alignment and the mitotic checkpoint through direct interaction with Bub1 and BubR1. *Dev. Cell* 13, 663-676.
- Kops, G.J., Kim, Y., Weaver, B.A., Mao, Y., McLeod, I., Yates, J.R., 3rd, Tagaya, M., and Cleveland, D.W. (2005). ZW10 links mitotic checkpoint signaling to the structural kinetochore. *The Journal of cell biology* 169, 49-60.
- Krenn, V., Overlack, K., Primorac, I., van Gerwen, S., and Musacchio, A. (2014). KI motifs of human Knl1 enhance assembly of comprehensive spindle checkpoint complexes around MELT repeats. *Current biology : CB* 24, 29-39.
- Kulukian, A., Han, J.S., and Cleveland, D.W. (2009). Unattached kinetochores catalyze production of an anaphase inhibitor that requires a Mad2 template to prime Cdc20 for BubR1 binding. *Developmental cell* 16, 105-117.
- Kurita, K., Maeda, M., Mansour, M.A., Kokuryo, T., Uehara, K., Yokoyama, Y., Nagino, M., Hamaguchi, M., and Senga, T. (2016). TRIP13 is expressed in colorectal cancer and promotes cancer cell invasion. *Oncology letters* 12, 5240-5246.
- Lara-Gonzalez, P., Scott, M.I., Diez, M., Sen, O., and Taylor, S.S. (2011). BubR1 blocks substrate recruitment to the APC/C in a KEN-box-dependent manner. *J. Cell Sci.* 124, 4332-4345.
- Larkin, S.E., Holmes, S., Cree, I.A., Walker, T., Basketter, V., Bickers, B., Harris, S., Garbis, S.D., Townsend, P.A., and Aukim-Hastie, C. (2012). Identification of markers of prostate cancer progression using candidate gene expression. *British journal of cancer* 106, 157-165.

- Latuasan, H.E., and Berends, W. (1961). On the origin of the toxicity of toxoflavin. *Biochimica et biophysica acta* 52, 502-508.
- Laue, T.M., Shah, B.D., Ridgeway, R.M., and Pelletier, S.L. (1992). Computer-aided interpretation of analytical sedimentation data for proteins. In *Analytical ultracentrifugation in biochemistry and polymer science*, S.E. Harding, A.J. Rowe, and J.C. Horton, eds. (Cambridge, UK: The Royal Society of Chemistry), pp. 90-125.
- Li, R., and Murray, A.W. (1991). Feedback control of mitosis in budding yeast. *Cell* 66, 519-531.
- Lischetti, T., Zhang, G., Sedgwick, G.G., Bolanos-Garcia, V.M., and Nilsson, J. (2014). The internal Cdc20 binding site in BubR1 facilitates both spindle assembly checkpoint signalling and silencing. *Nature communications* 5, 5563.
- Liu, D., Vleugel, M., Backer, C.B., Hori, T., Fukagawa, T., Cheeseman, I.M., and Lampson, M.A. (2010). Regulated targeting of protein phosphatase 1 to the outer kinetochore by KNL1 opposes Aurora B kinase. *The Journal of cell biology* 188, 809-820.
- London, N., and Biggins, S. (2014a). Mad1 kinetochore recruitment by Mps1-mediated phosphorylation of Bub1 signals the spindle checkpoint. *Genes & development* 28, 140-152.
- London, N., and Biggins, S. (2014b). Signalling dynamics in the spindle checkpoint response. *Nature reviews. Molecular cell biology* 15, 736-747.
- London, N., Ceto, S., Ranish, J.A., and Biggins, S. (2012). Phosphoregulation of Spc105 by Mps1 and PP1 regulates Bub1 localization to kinetochores. *Curr. Biol.* 22, 900-906.
- Luo, X., Fang, G., Coldiron, M., Lin, Y., Yu, H., Kirschner, M.W., and Wagner, G. (2000). Structure of the Mad2 spindle assembly checkpoint protein and its interaction with Cdc20. *Nature structural biology* 7, 224-229.
- Luo, X., Tang, Z., Rizo, J., and Yu, H. (2002). The Mad2 spindle checkpoint protein undergoes similar major conformational changes upon binding to either Mad1 or Cdc20. *Molecular cell* 9, 59-71.
- Luo, X., Tang, Z., Xia, G., Wassmann, K., Matsumoto, T., Rizo, J., and Yu, H. (2004). The Mad2 spindle checkpoint protein has two distinct natively folded states. *Nature structural & molecular biology* 11, 338-345.
- Luo, X., and Yu, H. (2005). Purification and assay of Mad2: a two-state inhibitor of anaphase-promoting complex/cyclosome. *Methods in enzymology* 398, 246-255.
- Luo, X., and Yu, H. (2008). Protein metamorphosis: the two-state behavior of Mad2. *Structure* 16, 1616-1625.
- Ma, H.T., and Poon, R.Y. (2016). TRIP13 Regulates Both the Activation and Inactivation of the Spindle-Assembly Checkpoint. *Cell reports* 14, 1086-1099.
- Maderspacher, F. (2008). Theodor Boveri and the natural experiment. *Current biology : CB* 18, R279-286.
- Manchester, K.L. (1995). Theodor Boveri and the origin of malignant tumours. *Trends in cell biology* 5, 384-387.

- Mapelli, M., Filipp, F.V., Rancati, G., Massimiliano, L., Nezi, L., Stier, G., Hagan, R.S., Confalonieri, S., Piatti, S., Sattler, M., *et al.* (2006). Determinants of conformational dimerization of Mad2 and its inhibition by p31comet. *The EMBO journal* *25*, 1273-1284.
- Mapelli, M., Massimiliano, L., Santaguida, S., and Musacchio, A. (2007). The Mad2 conformational dimer: structure and implications for the spindle assembly checkpoint. *Cell* *131*, 730-743.
- Mapelli, M., and Musacchio, A. (2007). MAD contortions: conformational dimerization boosts spindle checkpoint signaling. *Curr. Opin. Struct. Biol.* *17*, 716-725.
- Marks, D.H., Thomas, R., Chin, Y., Shah, R., Khoo, C., and Benezra, R. (2017). Mad2 Overexpression Uncovers a Critical Role for TRIP13 in Mitotic Exit. *Cell Rep.* *19*, 1832-1845.
- Martin-Lluesma, S., Stucke, V.M., and Nigg, E.A. (2002). Role of Hec1 in spindle checkpoint signaling and kinetochore recruitment of Mad1/Mad2. *Science* *297*, 2267-2270.
- Martinez-Font, E., Felipe-Abrio, I., Calabuig-Farinas, S., Ramos, R., Terrasa, J., Vogler, O., Alemany, R., Martin-Broto, J., and Obrador-Hevia, A. (2017). Disruption of TCF/beta-Catenin Binding Impairs Wnt Signaling and Induces Apoptosis in Soft Tissue Sarcoma Cells. *Molecular cancer therapeutics* *16*, 1166-1176.
- Matson, D.R., and Stukenberg, P.T. (2014). CENP-I and Aurora B act as a molecular switch that ties RZZ/Mad1 recruitment to kinetochore attachment status. *The Journal of cell biology* *205*, 541-554.
- McCoy, A.J., Grosse-Kunstleve, R.W., Adams, P.D., Winn, M.D., Storoni, L.C., and Read, R.J. (2007). Phaser crystallographic software. *J Appl Crystallogr* *40*, 658-674.
- Meadows, J.C., Shepperd, L.A., Vanoosthuysen, V., Lancaster, T.C., Sochaj, A.M., Buttrick, G.J., Hardwick, K.G., and Millar, J.B. (2011). Spindle checkpoint silencing requires association of PP1 to both Spc7 and kinesin-8 motors. *Developmental cell* *20*, 739-750.
- Miller, S.A., Johnson, M.L., and Stukenberg, P.T. (2008). Kinetochore attachments require an interaction between unstructured tails on microtubules and Ndc80(Hec1). *Current biology : CB* *18*, 1785-1791.
- Miniowitz-Shemtov, S., Eytan, E., Ganoh, D., Sitry-Shevah, D., Dumin, E., and Hershko, A. (2012). Role of phosphorylation of Cdc20 in p31(comet)-stimulated disassembly of the mitotic checkpoint complex. *Proceedings of the National Academy of Sciences of the United States of America* *109*, 8056-8060.
- Miniowitz-Shemtov, S., Eytan, E., Kaisari, S., Sitry-Shevah, D., and Hershko, A. (2015). Mode of interaction of TRIP13 AAA-ATPase with the Mad2-binding protein p31comet and with mitotic checkpoint complexes. *Proceedings of the National Academy of Sciences of the United States of America* *112*, 11536-11540.
- Miniowitz-Shemtov, S., Teichner, A., Sitry-Shevah, D., and Hershko, A. (2010). ATP is required for the release of the anaphase-promoting complex/cyclosome from inhibition by the mitotic checkpoint. *Proceedings of the National Academy of Sciences of the United States of America* *107*, 5351-5356.

- Mora-Santos, M.D., Hervas-Aguilar, A., Sewart, K., Lancaster, T.C., Meadows, J.C., and Millar, J.B. (2016). Bub3-Bub1 Binding to Spc7/KNL1 Toggles the Spindle Checkpoint Switch by Licensing the Interaction of Bub1 with Mad1-Mad2. *Curr. Biol.* *26*, 2642-2650.
- Moyle, M.W., Kim, T., Hattersley, N., Espeut, J., Cheerambathur, D.K., Oegema, K., and Desai, A. (2014). A Bub1-Mad1 interaction targets the Mad1-Mad2 complex to unattached kinetochores to initiate the spindle checkpoint. *J. Cell Biol.* *204*, 647-657.
- Musacchio, A. (2015). The Molecular Biology of Spindle Assembly Checkpoint Signaling Dynamics. *Current biology : CB* *25*, R1002-1018.
- Musacchio, A., and Salmon, E.D. (2007). The spindle-assembly checkpoint in space and time. *Nature reviews. Molecular cell biology* *8*, 379-393.
- Nieto-Jimenez, C., Alcaraz-Sanabria, A., Paez, R., Perez-Pena, J., Corrales-Sanchez, V., Pandiella, A., and Ocana, A. (2016). DNA-damage related genes and clinical outcome in hormone receptor positive breast cancer. *Oncotarget*.
- Olivares, A.O., Baker, T.A., and Sauer, R.T. (2016). Mechanistic insights into bacterial AAA+ proteases and protein-remodelling machines. *Nature reviews. Microbiology* *14*, 33-44.
- Otwinowski, Z., and Minor, W. (1997). Processing X-ray diffraction data collected in oscillation mode. *Methods Enzymol.* *276*, 307-326.
- Overlack, K., Primorac, I., Vleugel, M., Krenn, V., Maffini, S., Hoffmann, I., Kops, G.J., and Musacchio, A. (2015). A molecular basis for the differential roles of Bub1 and BubR1 in the spindle assembly checkpoint. *eLife* *4*, e05269.
- Paweletz, N. (2001). Walther Flemming: pioneer of mitosis research. *Nature reviews. Molecular cell biology* *2*, 72-75.
- Pesenti, M.E., Weir, J.R., and Musacchio, A. (2016). Progress in the structural and functional characterization of kinetochores. *Current opinion in structural biology* *37*, 152-163.
- Philmus, B., Shaffer, B.T., Kidarsa, T.A., Yan, Q., Raaijmakers, J.M., Begley, T.P., and Loper, J.E. (2015). Investigations into the Biosynthesis, Regulation, and Self-Resistance of Toxoflavin in *Pseudomonas protegens* Pf-5. *Chembiochem : a European journal of chemical biology* *16*, 1782-1790.
- Primorac, I., Weir, J.R., Chiroli, E., Gross, F., Hoffmann, I., van Gerwen, S., Ciliberto, A., and Musacchio, A. (2013). Bub3 reads phosphorylated MELT repeats to promote spindle assembly checkpoint signaling. *eLife* *2*, e01030.
- Raof, A., Depledge, P., Hamilton, N.M., Hamilton, N.S., Hitchin, J.R., Hopkins, G.V., Jordan, A.M., Maguire, L.A., McGonagle, A.E., Mould, D.P., *et al.* (2013). Toxoflavins and deazaflavins as the first reported selective small molecule inhibitors of tyrosyl-DNA phosphodiesterase II. *Journal of medicinal chemistry* *56*, 6352-6370.
- Reddy, S.K., Rape, M., Margansky, W.A., and Kirschner, M.W. (2007). Ubiquitination by the anaphase-promoting complex drives spindle checkpoint inactivation. *Nature* *446*, 921-925.

- Rosenberg, J.S., Cross, F.R., and Funabiki, H. (2011). KNL1/Spc105 recruits PP1 to silence the spindle assembly checkpoint. *Current biology : CB* 21, 942-947.
- Rosenberg, S.C., and Corbett, K.D. (2015). The multifaceted roles of the HORMA domain in cellular signaling. *The Journal of cell biology* 211, 745-755.
- San-Segundo, P.A., and Roeder, G.S. (1999). Pch2 links chromatin silencing to meiotic checkpoint control. *Cell* 97, 313-324.
- Scheer, U. (2014). Historical roots of centrosome research: discovery of Boveri's microscope slides in Wurzburg. *Philosophical transactions of the Royal Society of London. Series B, Biological sciences* 369.
- Schuck, P. (2000). Size-distribution analysis of macromolecules by sedimentation velocity ultracentrifugation and lamm equation modeling. *Biophysical journal* 78, 1606-1619.
- Schuck, P., and Demeler, B. (1999). Direct sedimentation analysis of interference optical data in analytical ultracentrifugation. *Biophys J.* 76, 2288-2296.
- Shepherd, L.A., Meadows, J.C., Sochaj, A.M., Lancaster, T.C., Zou, J., Buttrick, G.J., Rappsilber, J., Hardwick, K.G., and Millar, J.B. (2012). Phosphodependent recruitment of Bub1 and Bub3 to Spc7/KNL1 by Mph1 kinase maintains the spindle checkpoint. *Current biology : CB* 22, 891-899.
- Sironi, L., Mapelli, M., Knapp, S., De Antoni, A., Jeang, K.T., and Musacchio, A. (2002). Crystal structure of the tetrameric Mad1-Mad2 core complex: implications of a 'safety belt' binding mechanism for the spindle checkpoint. *EMBO J.* 21, 2496-2506.
- Sivakumar, S., and Gorbsky, G.J. (2015). Spatiotemporal regulation of the anaphase-promoting complex in mitosis. *Nature reviews. Molecular cell biology* 16, 82-94.
- Sivakumar, S., Janczyk, P.L., Qu, Q., Brautigam, C.A., Stukenberg, P.T., Yu, H., and Gorbsky, G.J. (2016). The human SKA complex drives the metaphase-anaphase cell cycle transition by recruiting protein phosphatase 1 to kinetochores. *eLife* 5.
- Skinner, J.J., Wood, S., Shorter, J., Englander, S.W., and Black, B.E. (2008). The Mad2 partial unfolding model: regulating mitosis through Mad2 conformational switching. *The Journal of cell biology* 183, 761-768.
- Soares, K.M., Blackmon, N., Shun, T.Y., Shinde, S.N., Takyi, H.K., Wipf, P., Lazo, J.S., and Johnston, P.A. (2010). Profiling the NIH Small Molecule Repository for compounds that generate H<sub>2</sub>O<sub>2</sub> by redox cycling in reducing environments. *Assay and drug development technologies* 8, 152-174.
- Stegmeier, F., Rape, M., Draviam, V.M., Nalepa, G., Sowa, M.E., Ang, X.L., McDonald, E.R., 3rd, Li, M.Z., Hannon, G.J., Sorger, P.K., *et al.* (2007). Anaphase initiation is regulated by antagonistic ubiquitination and deubiquitination activities. *Nature* 446, 876-881.
- Stern, K.G. (1935). Oxidation-reduction potentials of toxoflavin. *The Biochemical journal* 29, 500-508.
- Sudakin, V., Chan, G.K., and Yen, T.J. (2001). Checkpoint inhibition of the APC/C in HeLa cells is mediated by a complex of BUBR1, BUB3, CDC20, and MAD2. *J. Cell Biol.* 154, 925-936.

- Tang, Z., Bharadwaj, R., Li, B., and Yu, H. (2001). Mad2-independent inhibition of APC<sup>Cdc20</sup> by the mitotic checkpoint protein BubR1. *Dev. Cell* *1*, 227-237.
- Tang, Z., and Yu, H. (2004). Functional analysis of the spindle-checkpoint proteins using an in vitro ubiquitination assay. *Methods Mol. Biol.* *281*, 227-242.
- Tao, Y., Yang, G., Yang, H., Song, D., Hu, L., Xie, B., Wang, H., Gao, L., Gao, M., Xu, H., *et al.* (2017). TRIP13 impairs mitotic checkpoint surveillance and is associated with poor prognosis in multiple myeloma. *Oncotarget* *8*, 26718-26731.
- Teichner, A., Eytan, E., Sitry-Shevah, D., Miniowitz-Shemtov, S., Dumin, E., Gromis, J., and Hershko, A. (2011). p31<sup>comet</sup> Promotes disassembly of the mitotic checkpoint complex in an ATP-dependent process. *Proceedings of the National Academy of Sciences of the United States of America* *108*, 3187-3192.
- Thorne, N., Auld, D.S., and Inglese, J. (2010). Apparent activity in high-throughput screening: origins of compound-dependent assay interference. *Current opinion in chemical biology* *14*, 315-324.
- Uzunova, K., Dye, B.T., Schutz, H., Ladurner, R., Petzold, G., Toyoda, Y., Jarvis, M.A., Brown, N.G., Poser, I., Novatchkova, M., *et al.* (2012). APC15 mediates CDC20 autoubiquitylation by APC/C(MCC) and disassembly of the mitotic checkpoint complex. *Nature structural & molecular biology* *19*, 1116-1123.
- Varetti, G., Guida, C., Santaguida, S., Chirolì, E., and Musacchio, A. (2011). Homeostatic control of mitotic arrest. *Mol. Cell* *44*, 710-720.
- Varma, D., Wan, X., Cheerambathur, D., Gassmann, R., Suzuki, A., Lawrimore, J., Desai, A., and Salmon, E.D. (2013). Spindle assembly checkpoint proteins are positioned close to core microtubule attachment sites at kinetochores. *The Journal of cell biology* *202*, 735-746.
- Vleugel, M., Tromer, E., Omerzu, M., Groenewold, V., Nijenhuis, W., Snel, B., and Kops, G.J. (2013). Arrayed BUB recruitment modules in the kinetochore scaffold KNL1 promote accurate chromosome segregation. *J. Cell Biol.* *203*, 943-955.
- Wang, K., Sturt-Gillespie, B., Hittle, J.C., Macdonald, D., Chan, G.K., Yen, T.J., and Liu, S.T. (2014a). Thyroid hormone receptor interacting protein 13 (TRIP13) AAA-ATPase is a novel mitotic checkpoint-silencing protein. *The Journal of biological chemistry* *289*, 23928-23937.
- Wang, K., Sturt-Gillespie, B., Hittle, J.C., Macdonald, D., Chan, G.K., Yen, T.J., and Liu, S.T. (2014b). Thyroid Hormone Receptor Interacting Protein 13 (TRIP13) AAA-ATPase is a Novel Mitotic Checkpoint Silencing Protein. *J. Biol. Chem.* *289*, 23928-23937.
- Weinert, T., and Hartwell, L. (1989). Control of G2 delay by the rad9 gene of *Saccharomyces cerevisiae*. *Journal of cell science. Supplement* *12*, 145-148.
- Weir, J.R., Faesen, A.C., Klare, K., Petrovic, A., Basilico, F., Fischbock, J., Pentakota, S., Keller, J., Pesenti, M.E., Pan, D., *et al.* (2016). Insights from biochemical reconstitution into the architecture of human kinetochores. *Nature* *537*, 249-253.
- Westhorpe, F.G., Tighe, A., Lara-Gonzalez, P., and Taylor, S.S. (2011). p31<sup>comet</sup>-mediated extraction of Mad2 from the MCC promotes efficient mitotic exit. *Journal of cell science* *124*, 3905-3916.

- Xia, G., Luo, X., Habu, T., Rizo, J., Matsumoto, T., and Yu, H. (2004). Conformation-specific binding of p31(comet) antagonizes the function of Mad2 in the spindle checkpoint. *The EMBO journal* *23*, 3133-3143.
- Yamagishi, Y., Yang, C.H., Tanno, Y., and Watanabe, Y. (2012). MPS1/Mph1 phosphorylates the kinetochore protein KNL1/Spc7 to recruit SAC components. *Nature cell biology* *14*, 746-752.
- Yamaguchi, M., VanderLinden, R., Weissmann, F., Qiao, R., Dube, P., Brown, N.G., Haselbach, D., Zhang, W., Sidhu, S.S., Peters, J.M., *et al.* (2016). Cryo-EM of Mitotic Checkpoint Complex-Bound APC/C Reveals Reciprocal and Conformational Regulation of Ubiquitin Ligation. *Molecular cell* *63*, 593-607.
- Yang, M., Li, B., Liu, C.J., Tomchick, D.R., Machius, M., Rizo, J., Yu, H., and Luo, X. (2008). Insights into mad2 regulation in the spindle checkpoint revealed by the crystal structure of the symmetric mad2 dimer. *PLoS biology* *6*, e50.
- Yang, M., Li, B., Tomchick, D.R., Machius, M., Rizo, J., Yu, H., and Luo, X. (2007). p31comet blocks Mad2 activation through structural mimicry. *Cell* *131*, 744-755.
- Ye, Q., Kim, D.H., Dereli, I., Rosenberg, S.C., Hagemann, G., Herzog, F., Toth, A., Cleveland, D.W., and Corbett, K.D. (2017). The AAA+ ATPase TRIP13 remodels HORMA domains through N-terminal engagement and unfolding. *The EMBO journal* *36*, 2419-2434.
- Ye, Q., Rosenberg, S.C., Moeller, A., Speir, J.A., Su, T.Y., and Corbett, K.D. (2015). TRIP13 is a protein-remodeling AAA+ ATPase that catalyzes MAD2 conformation switching. *eLife* *4*.
- Yu, H. (2007). Cdc20: a WD40 activator for a cell cycle degradation machine. *Molecular cell* *27*, 3-16.
- Zaytsev, A.V., Sundin, L.J., DeLuca, K.F., Grishchuk, E.L., and DeLuca, J.G. (2014). Accurate phosphoregulation of kinetochore-microtubule affinity requires unconstrained molecular interactions. *The Journal of cell biology* *206*, 45-59.
- Zhang, D., Yin, S., Jiang, M.X., Ma, W., Hou, Y., Liang, C.G., Yu, L.Z., Wang, W.H., and Sun, Q.Y. (2007). Cytoplasmic dynein participates in meiotic checkpoint inactivation in mouse oocytes by transporting cytoplasmic mitotic arrest-deficient (Mad) proteins from kinetochores to spindle poles. *Reproduction* *133*, 685-695.
- Zhang, G., Lischetti, T., and Nilsson, J. (2014). A minimal number of MELT repeats supports all functions of KNL1 in chromosome segregation. *J. Cell Sci.* *127*, 871-884.
- Zhang, Y., Xue, Q., Pan, G., Meng, Q.H., Tuo, X., Cai, X., Chen, Z., Li, Y., Huang, T., Duan, X., *et al.* (2017). Integrated Analysis of Genome-Wide Copy Number Alterations and Gene Expression Profiling of Lung Cancer in Xuanwei, China. *PloS one* *12*, e0169098.
- Zhou, H.J., Wang, J., Yao, B., Wong, S., Djakovic, S., Kumar, B., Rice, J., Valle, E., Soriano, F., Menon, M.K., *et al.* (2015). Discovery of a First-in-Class, Potent, Selective, and Orally Bioavailable Inhibitor of the p97 AAA ATPase (CB-5083). *Journal of medicinal chemistry* *58*, 9480-9497.

Zhou, K., Zhang, W., Zhang, Q., Gui, R., Zhao, H., Chai, X., Li, Y., Wei, X., and Song, Y. (2017). Loss of thyroid hormone receptor interactor 13 inhibits cell proliferation and survival in human chronic lymphocytic leukemia. *Oncotarget* 8, 25469-25481.